X-ray reflection from surfaces and interfaces

Goldar, Arach

Award date:
2001

Awarding institution:
University of Bath

X-Ray Reflection from surfaces and interfaces

submitted by **Arach Goldar**
for the degree of PhD
of the University of Bath
2001

ProQuest LLC
789 East Eisenhower Parkway
P.O. Box 1346
Ann Arbor, MI 48106-1346

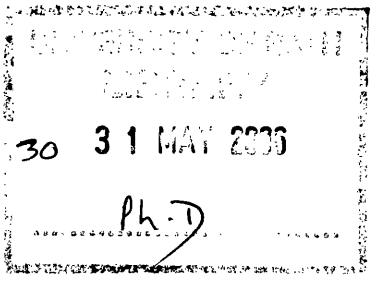
30 31 MAY 2006
Ph.D

University of Bath

Department of Chemistry

Doctor of Philosophy

X-Ray Reflection from surfaces and interfaces

by Arach Goldar

Abstract

The possibility of using n-type silicon [111] as an electrode, during *in-situ* neutron or X-ray reflection investigations of an electrochemical process has been considered. The low scattering length density of silicon compared to other metallic electrodes and its relative transparency to neutrons make it an excellent candidate for such studies. The simplicity in the structure of this electrode and the relative ease of cleaning the surface of the n-type silicon [111] electrode has been shown. The feasibility of the use of silicon electrode has been demonstrated by an *in-situ* X-ray reflection investigation of the electropolymerisation of poly (aniline). The structure of the polymer film has been determined. The film is composed of two parts: the first part, near the electrode surface, is made of a compact polymer film and the second part, lying on top of this smooth layer, forms a more open structure. The high degree of roughness of the surface of the polymer film makes the data interpretation difficult. Therefore, a new theory has been developed to analyse the reflected intensity from very rough surface. This method of analysis is based on the variation of the shape of the total reflection edge in the reflectivity profile when the correlation length and the height of the surface roughness are larger than the wavelength of the incoming beam. The possibility of using this technique to study the kinetics of surface roughness variation is considered and applied to the electrochemical study of silicon / fluoride solution. By use of this technique the roughening of the silicon surface during the cathodic polarization is linked to the incorporation of hydrogen into the silicon lattice, and the anodic dissolution to the diffusion of the fluoride ions toward the surface of the electrode.

To my Father and Mother

Wish you were here.
Pink Floyd

Acknowledgements

I express all my gratitude to my supervisor, Dr. Steve Roser, for all his help, guidance and encouragement through these three years of work. I am grateful for the opportunity I had to work with, to play with and finally to keep running a homebuilt instrument which helps me to understand better the reflectivity theory than by using the Fourier transform!!

I would like also to thank Dr. Michael Gerstenberg for his help and enthusiasm during the neutron reflectivity experiment at Riso National Laboratory and his critical point of view on the theoretical part of the work.

I wish to thank my partners in crime: Dr. Arwel Huges, Dr. Karen Edler, Dr. Tessa Brennan and Barry Stidder. They were always available to provide an extra pair of hands or four other brains to help me to solve a problem.

Special thanks to "Sam" who supports me and helps me in the moment of crisis. Her patience and kindness can never be fully acknowledged.

I wish to thanks my flat mates: Diego Oriato, Hadi Madani, Michael Gill Carry, Jean-Philippe Cros and Cristelle Claverie for standing my "hairy face" and "hairy head" during two years.

I do not forget to thanks all the students of the chemistry department and particularly: Marie, Maurizio, Fred, Coco, Tim and Shin for their good humour and happiness.

Thanks to Arimori for his help to my computer problems!!!

Finally, I would like to thank all my relatives who supported me over the years, especially my parents.

Contents

Chapter I

General introduction

"Physicists like to think that all you have to do is say: these are the conditions, now what happens next?"

Richard P. Feynman

The aim of this thesis is to propose a new type of electrode system that can be used for neutron and X-ray reflection. Some typical examples of the use of this electrode (electrodeposited polymer films) are investigated, and new, general theories to explain the observed scattering are put forward.

Several works have already investigated the growth of thin polymer films at electrodes using neutron reflection [1-4]. The distribution of ions and metallic deposition at electrolyte/electrode interfaces have also been widely studied by using X-ray reflection [5-7]. The success of all these experiments has always been limited by the availability, complexity and quality of the electrode material. To perform reflection measurements at the solid/liquid interface, using neutron reflectivity, the beam impinges on the sample through a solid, usually single crystal block, which forms the back of electrode [3] (Figure 1.1).

The traditional method uses a system of plating a gold or palladium electrode onto a

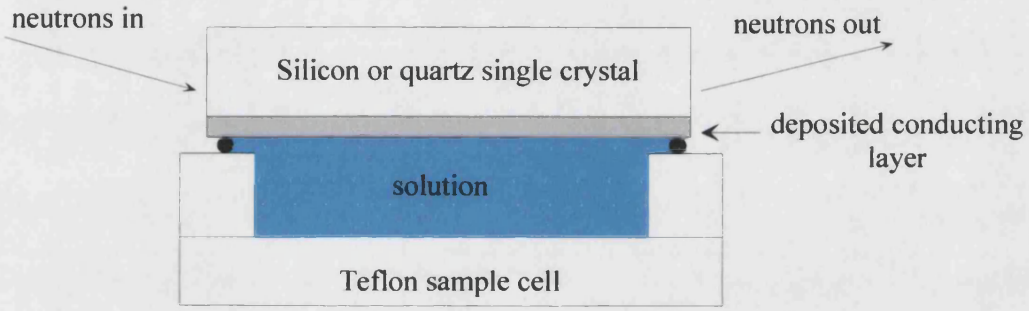

Figure 1.1. Configuration of the cell for neutron reflection from solid / liquid interface

quartz substrate or a multilayer of chromium and gold on top of a silicon substrate. The use of these thin metal films (about 4000Å) complicates the structure of the electrode by introducing a number of extra interfaces into the scattering problem, which have to be separately determined for each experiment. In addition, after plating of polymer onto the electrode, the ingot has to be recoated with metal, a non-trivial process that could not be easily carried out on-site. Thus the number of experiments performed in a single visit to a neutron scattering facility is highly limited. This is a serious drawback as the use of many different solvent contrasts greatly aids the indisputable determination of the polymer film structure.

In the case of X-rays, the solid/liquid interface is illuminated through the liquid phase. The absorption of X-rays by the liquid normally constrains one to use a complex cell [8, 9].

The high scattering length density of classical electrodes (gold, platinum) limits the use of X-rays to study the deposition of polymeric material at the surface of the electrode, simply because the contrast of the metal with the electron density of the polymer is insufficient to resolve any film structure. One of the ways to overcome these problems is to simplify the structure of the electrode. Highly doped silicon can be considered as a good choice for the solution of these problems. The low electron density of this material compared with other metallic electrodes (silicon = 2.012×10^{-5} $Å^{-2}$, gold = 13.14×10^{-5} $Å^{-2}$, platinum = 14.5×10^{-5} $Å^{-2}$) creates a bigger relative difference between the scattering from the electrode and the scattering from the polymer film top-layer in the case of X-rays. In addition to the interface's simplicity, the ability of neutrons to penetrate the silicon lattice without significant attenuation [10] make this material an ideal candidate for studying solid/liquid interface by neutron reflection. In principle, X-ray and neutrons could utilize this electrode as the basis of an ideal system to study the solid/ electrolyte interface. There are however major problems with the oxidation of the bare silicon surface and cleaning of the silicon electrode surface.

In this work we aim to demonstrate the possibility of using an n-type silicon electrode as an excellent working electrode for studying the *in-situ* formation of an electrochemical polymer film by neutron and X-ray reflection. In order to be able to carry out this study we have to focus first on the electrochemistry of silicon electrode and to define the conditions under which one can strip off the natural oxide layer from the silicon surface and have a relatively stable surface. Then we will demonstrate the possibility of growing a polymer film at the surface of this electrode, and we will characterize this polymer film by X-ray reflection.

It is well known that the cleaning of the silicon surface and the etching of the oxide layer changes the structure of the silicon surface [11]. The polymer film deposited on the surface of the electrode can be rough or smooth or it can undergo a transition between a smooth to rough surface during its formation In order to be able to determine the surface morphology and to study its *in-situ* variation during the chemical and electrochemical etching of the oxide layer by neutron and X-ray reflection we had to develop a new theory of scattering from rough surfaces.

Wave scattering from rough surfaces has been the subject of a huge number of books and research papers [12-22], both theoretical and experimental. Most of the theoretical work can be divided into two categories: approximate, as in perturbation theory [14-17,

[20, 21] and Kirchhoff theory [12, 19], or more rigorous but predominantly formal such as Integral equation technique [19], variation methods [19] and Green's function approach [13]. These theories are mathematically abstract and subject to approximations that are unrealistic in practical applications. In the domain of reflection of neutrons and X-rays from rough surfaces the most commonly used approach is a perturbative approach based on the Distorted Born Wave Approximation (DBWA) [23]. This technique supposes that the surface roughness can be considered as a perturbation to the flat surface [17]. However the validity of this technique breaks down when the in-plane dimension of the roughness and the normal to surface dimension of the roughness become important and therefore the roughness cannot be considered as a perturbation to the flat surface [17]. To the best of our knowledge, there was no theory covering scattering from this kind of surface morphology. Therefore, we have had to develop and extend the theory based on the principles of optical geometry, in order to be able to explain the kinetics of the changes in the reflected signal from the silicon electrode during the chemical or electrochemical etching process. We have studied the electrochemical and the chemical etching of the silicon oxide layer by a fluoride solution and by using the developed theory have linked the changes in the reflected intensity to the changes in the chemical composition of the surface.

In summary the aim of this work is to demonstrate the advantage of using n-type silicon as an electrode for *in-situ* study of an electrochemical process by X-ray and neutron reflectivity techniques. We will describe the full characterization of a polymer film electrodeposited on the surface of this electrode and show the consistency of the obtained results with the existing literature. Finally we will develop a new theory of scattering from rough surfaces and use this theory to study the chemical and electrochemical etching of the silicon electrode by neutron and X-rays reflection.

This thesis is organized into chapters as follows: Chapter II is a derivation of some of the scattering phenomena, starting with the classical scattering of an electromagnetic wave. Chapter III is an introduction to electrochemistry, specially orientated to the electrochemistry of semiconductors and electrodeposition processes.

The study of the electrodeposited film is performed in Chapter IV. In Chapter V we present a new theory of scattering from a "very rough" surface. The neutron reflection data from the hydrogen adsorption process and their analysis are presented in Chapter VI. The electro-etching and chemical etching of the silicon electrode in fluorinated

solution are analysed in terms of this new theory in Chapter VII. Finally, conclusions are presented in Chapter VIII.

REFERENCES:

1 R. M. Richardson, M. J. Swann, A. R. Hillman, et al., Faraday Discussion **94**, 295 (1992).

2 L. Bailey, M. J. Henderson, A. R. Hillman, et al., Physica B **276-278**, 373 (2000).

3 S. J. Roser, D. J. Caruana, and M. Gerstenberg, Journal of Electroanalytical Chemistry **411**, 153 (1996).

4 A. R. Hillman, A. Glidle, R. M. Richardson, et al., Journal of American Chemical Society **120**, 12882 (1998).

5 Y. P. Feng, S. K. Sinha, C. A. Melendres, et al., Physica B **221**, 251 (1996).

6 J. Wang, B. M. Ocko, A. J. Davenport, et al., Physical Review B **46**, 10321 (1992).

7 E. Herrero, L. J. Buller, J. Li, et al., Electrochimica Acta **44**, 983 (1998).

8 Z. Nagy, H. You, and R. M. Yonco, Rev. Sci. Instrum **65**, 2199 (1994).

9 Z. Nagy, H. You, R. M. Yonco, et al., Electrochimica Acta **36**, 209 (1991).

10 J. Daillant and A. Gibaud, *X-Ray and Neutron Reflectivity: Principles and Applications*, (1999).

11 P. Allongue, V. Kieling, and H. Gerischer, Electrochimica Acta **40**, 1353 (1995).

12 P. Beckmann and A. Spizzichino, *The Scattering of electromagnetic waves from Rough surfaces* (Pergamon, London, 1963).

13 C. Baylard, J.-J. Greffet, and A. A. Maradudin, J. Opt. Soc. Am. A **10**, 2637 (1993).

14 P. Croce, L. Nevot, and B. Pardo, C. R. Acad. Sc. Paris **Serie B**, 855 (1972).

15 P. Croce, L. Nevot, and B. Pardo, C. R. Acad. Sc. Paris **Serie B**, 803 (1972).

16 J. Daillant and O. Belorgey, J. Chem. Phys. **97**, 5824 (1992).

17 D. K. G. d. Boer, Physical Review B **49**, 5817 (1993).

18 P. Mikulik and T. Baumbach, Physical Review B **59**, 7632 (1999).

19 J. A. Ogilvy, *Theory of wave scattering from random rough surfaces* (Adam Hilger, Bristol U.K, 1991).

20 S. K. Sinha, M. Tolan, and A. Gibaud, Physical Review B **57**, 2740 (1998).

21 V. F. Sears, Physical Review B **48**, 17477 (1993).

22 K. Tang and R. o. Buckius, Int. J. Heat Mass Transfer **41**, 2037 (1998).

23 S. K. Sinha, E. B. Sirota, S. Garoff, et al., Physical Review B **38**, 2297 (1988).

Chapter II

Introduction to Reflectivity

"The question as to the reflection of the X-ray may be regarded as settled, by the experiments mentioned in the preceding paragraph, in favor of the view that no noticeable regular reflection of the rays takes place from any of the substances examined. Other experiments, which I here omit, lead to the same conclusion."

Röntgen

Würzburg Physico-Medical Society, December 28, 1895

2.1) Introduction

The aim of this chapter is to introduce the major concepts in the theory of reflectivity from surface and interfaces that we will use to study the systems presented in this thesis. This chapter might appear too detailed. However, all the notions developed in this chapter must be clearly determined and understood in order to be able in chapter V to follow the development of the reflection from "very rough surfaces". Most of this chapter is described in more detail in three different books: "Principle of Optics" [1], "X-ray and Neutron Reflectivity: Principles and Application" [2] and "Polymers and Neutron Scattering" [3].

Reflection techniques have been used for the last fifty years to describe the structure and properties of different type of materials at interfaces [4-14]. The basic principle of a reflectivity experiment set-up is simple (figure 2.1).

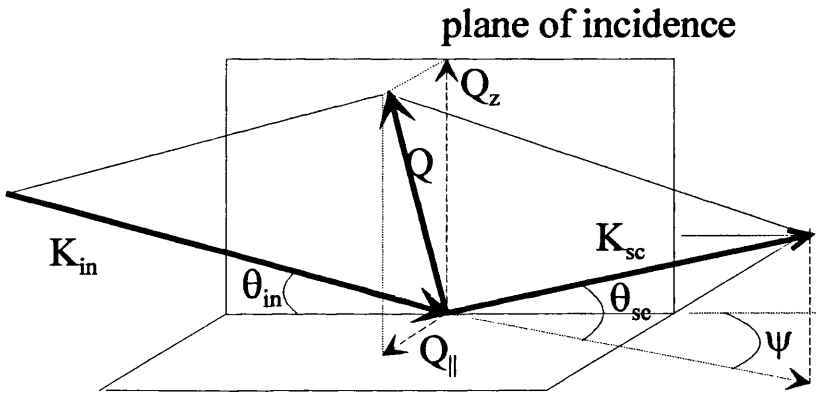

Figure 2.1. Scattering geometry for interpreting surface scattering

An incident beam directed along the wave vector $\mathbf{K_{in}}$, of wavelength λ, illuminates the interface. The angle of incidence, θ_{in}, is the angle between the $\mathbf{K_{in}}$ and the interface in the plane of incidence. The scattered intensity is detected in the far-field region in an arbitrary small solid angle in the direction $\mathbf{K_{sc}}$. The angle of detection, θ_{sc}, (in the plane of incidence) is the angle between the plane of interface and $\mathbf{K_{sc}}$. The in-plane angle of detection, ψ, is the angle between the plane of incidence and the projection of $\mathbf{K_{sc}}$ on the plane of interface. The interaction of the beam with the material results in a wave vector transfer $\mathbf{Q}$ [2,3].

$$\vec{Q} = \vec{K}_{sc} - \vec{K}_{in}$$

Equation 2.1

The wave vector transfer (or transfer moment) can be decomposed into two components: the in plane wave vector transfer, $\mathbf{Q}_{\|}$, and the normal to the interface wave vector transfer, $\mathbf{Q}_z$.

The work of Kiessing demonstrated that the scattered intensity contains structural information about the interface. He shows the possibility to link the variation of the reflected intensity as a function of angle of incidence (interference fringes) to the thickness of the material deposited at the interface. Others (Thomas [15], Nevot and Croce [16-18], Sinha [19], De Boher [20], Daillant [5, 21]) developed different analysis techniques and theories, based on the interaction between the radiation and matter, to extract information from the scattered intensity. However, the pioneer works on the analysis of the reflected intensity from an interface should be attributed to Fresnel and Lord Rayleigh. The only difference in the parameters used to analyse the reflected intensity between the pioneer's works and more recently developed theories is the wavelength of the incident radiation. The earliest works were dealing with the reflection of light from an interface, therefore these authors could only probe structures, which have a dimension roughly equal to the wavelength of the incident beam (500 nm). The more recent works have been interested into the definition of the molecular structure of an interface by using X-rays and neutron as the incident beam (1Å to 12Å).

Light and X-rays are electromagnetic radiation [1, 22]. Neutrons are nuclear radiation [2]. Maxwell in 1865 [1] defined and built a theory to describe the interaction of electromagnetic waves with matter. This can be summarised in an elegant set of four dependent equations (equation 2.2)

$$a: \vec{\nabla} \times \vec{H}(\vec{r},t) = \frac{\partial \vec{D}(\vec{r},t)}{\partial t} + \vec{J}(\vec{r},t)$$
$$b: \vec{\nabla} \cdot \vec{B}(\vec{r},t) = 0$$
$$c: \vec{\nabla} \times \vec{E}(\vec{r},t) = -\frac{\partial \vec{B}(\vec{r},t)}{\partial t}$$
$$d: \vec{\nabla} \cdot \vec{D}(\vec{r},t) = \varphi(\vec{r},t)$$

Equation 2.2

Where the operator ∇ is a three dimensional vector

$$\vec{\nabla} = \left(\frac{\partial}{\partial x}, \frac{\partial}{\partial y}, \frac{\partial}{\partial z} \right)$$

Equation 2.3

the time dependent (time-harmonic) electric field vector **E(r,t)** is in volts/meter, the time dependent (time-harmonic) magnetic field vector **H(r,t)** is in amperes/meter, **D(r,t)** is the electric displacement vector in coulombs/meter^2, **B(r,t)** is the magnetic flux density vector in webers/meter^2, **J(r,t)** is the current density vector in amperes/meter^2, and let φ**(r,t)** be the volume charge density in coulombs/meter^3. The link between these four equations depends on the characteristics of the medium which defines a set of relationship among **D, E, B, H** and **J**. For example in the case of an isotropic lossless medium (no charge or current) we have [1]:

$$\vec{D}(\vec{r},t) = \varepsilon(\vec{r})\vec{E}(\vec{r},t)$$
$$\vec{B}(\vec{r},t) = \mu(\vec{r})\vec{H}(\vec{r},t)$$
$$\vec{J}(\vec{r},t) = \vec{0}$$

Equation 2.4

Where ε**(r)** is the permittivity or dielectric constant (farad/meter), μ**(r)** is the permeability (henries/meter), and both ε**(r)** and μ**(r)** are real. For free space, the dielectric constant and the permeability are [1]

$$\varepsilon_0 = 8.854 \times 10^{-12}\ farad/meter$$
$$\mu_0 = 4\pi \times 10^{-7}\ henry/meter$$

Equation 2.5

Note that the light velocity in free space is given by [1]

$$c = \frac{1}{\sqrt{\varepsilon_0 \mu_0}} \cong 3 \times 10^8\ m.s^{-1}$$

Equation 2.6

We define the index of refraction as [1]:

$$n(\vec{r}) = \frac{\sqrt{\varepsilon(\vec{r})\mu(\vec{r})}}{c}$$

Equation 2.7

Therefore, in the case of an isotropic nonabsorbing medium we can reduce the four Maxwell's equations to two sets of independent equations [22] (Helmholtz equations).

One describes the propagation of the electric field in the medium (equation 2.8) and the other one the propagation of the magnetic field in the medium.

$$\nabla^2 \vec{E}(\vec{r}) + n^2(\vec{r})\frac{\omega^2}{c^2}\vec{E}(\vec{r}) = 0$$

Equation 2.8

Where ω is equal to:

$$\omega = \frac{2\pi}{\lambda}c$$

Equation 2.9

Let us define the wave number K as the magnitude of the wave vector **K** in the media as:

$$K(\vec{r}) = n(\vec{r})\frac{\omega}{c}$$

Equation 2.10

and the wave number in the vacuum K_0 as

$$K_0(\vec{r}) = \frac{\omega}{c}$$

Equation 2.11

therefore we can re-write equation 2.8 in the following form:

$$\nabla^2 E(\vec{r}) + \left(K_0^2 - U(\vec{r})\right)E(\vec{r}) = 0$$

Equation 2.12

where $U(\vec{r}) = K_0^2\left(1 - n^2(\vec{r})\right)$

This equation will be used in this chapter as the basis for the description of the electromagnetic radiation-matter interaction.

Neutrons can be described by a wave of wavelength λ, of wave vector [2]:

$$K_0 = \frac{2\pi}{\lambda}$$

Equation 2.13

and of energy

$$E_0 = \frac{\hbar^2 K_0^2}{2m}$$

Equation 2.14

Its wave function is the solution the Schrödinger equation [2]:

$$\nabla^2\Psi(\vec{r})+\left[K_0^2-V(\vec{r})\right]\Psi(\vec{r})=0$$

Equation 2.15

Where m is the neutron mass and V(**r**) is the interaction potential which characterises the material. The similarities in structure between equation 2.12, from electromagnetic theory, and 2.15, from the Schrödinger equation, are remarkable, and, the mathematical development of one of these interactions can straightforwardly be applied to the other one. In this chapter we have decided to deal with the electromagnetic radiation, from which the basic results for neutron scattering follow. We first establish a general propagation equation for electric field. In the third section we discuss the notion of coherent (specular) and incoherent scattered intensity. The other sections of this chapter are only about the specular component of the reflected intensity. A more detailed description of the diffuse part of the reflected intensity is given in the chapter V. In the fourth part of this chapter we derive an expression for the reflection coefficient as a function of polarisation. The fifth section of this chapter defines the notion of Brewster angle, and the total reflection. In the sixth section we discuss three commonly used techniques to model the reflection coefficient from a stratified medium. Then in the seventh section we describe the effect of the roughness on the reflection coefficient profile. Finally we will discuss the experimental and theoretical limitation of the specular reflectivity technique.

2.2) Propagation equation

As we have seen in the introduction (section 2.1), the behaviour of the electric field in a medium is described by the Helmholtz's equation. We have also obtained the propagation equation for the electric field in a homogeneous media containing no charge or current (equation 2.8). The refractive index, n(**r**), depends on the atomic or molecular scattering [22] and the nature of its dependence on the latter should be established. Figure 2.2 represents the scattering of a beam from the surface of a stratified medium. If the variation of the refractive index at the surface (in this case due to the roughness) is small compared to the refractive index of the stratified media, we can consider the variation of the index, $\delta n(\mathbf{r})$, as a perturbation to the refractive index of the stratified media (which can be considered as a reference refractive index, $n_{ref}(\mathbf{r})$) [17].

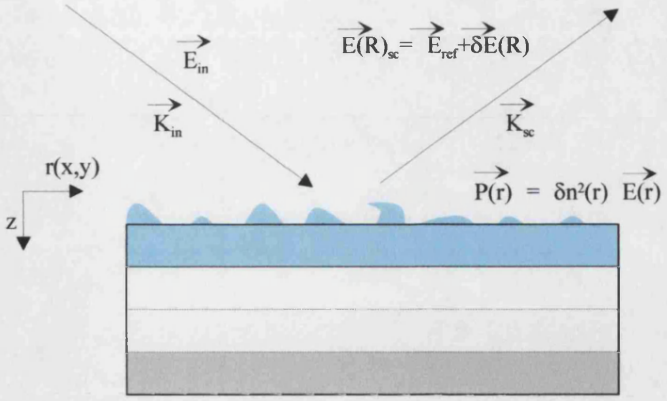

Figure 2.2. Illustration of the reflection from a multilayer. The surface roughness is consider a perturbation to the refractive index.

Hence we decompose the index as [5, 16, 17]:

$$n^2(\vec{r}) = n_{ref}^2(\vec{r}) + \delta n^2(\vec{r})$$

Equation 2.16

The reference medium, of refractive index $n_{ref}(\mathbf{r})$, creates an electrical field $\mathbf{E}_{ref}(R)$ at a distance R far from the surface. The index $\delta n(\mathbf{r})$ creates also an electrical field $\delta\mathbf{E}(R)$ at a distance R far from the surface. As Maxwell's equation are linear [1], the total electric field at a distance R far from the surface can be written as:

$$\vec{E}(R) = \vec{E}_{ref}(R) + \delta\vec{E}(R)$$

Equation 2.17

Where $E_{ref}(R)$ is the field in the reference case and $\delta\mathbf{E}(R)$ is the perturbation in the field radiated by the surface. By introducing equation 2.16 into the equation 2.8 we obtain:

$$\nabla^2 E(\vec{r}) + n_{ref}^2(\vec{r}) K_0^2 E(\vec{r}) = -\delta n^2(\vec{r}) K_0^2 E(\vec{r})$$

Equation 2.18

The right-hand side of equation 2.18 can be considered as a virtual dipole source of dipole density $\mathbf{P}(\mathbf{r})=\varepsilon_0\ \delta n^2(\mathbf{r})\ \mathbf{E}(\mathbf{r})$ [17]. This consideration led Croce [17] to calculate $\delta\mathbf{E}(\mathbf{r})$ using the reciprocity theorem [22], and then to calculate the reflected field.

2.3) Notions on Coherent (specular) and Incoherent (diffuse) Reflection

In the last section we showed that the scattered field at a point R far from the surface could be considered as the sum of the field scattered by the reference medium (mean part of the field) and a fluctuating part (equation 2.17). In the far-field region the scattered electric field, $\mathbf{E}_{sc}$, behaves like a plane wave [1, 2] with a wave vector $\mathbf{K}_{sc}$ and amplitude $E(\mathbf{K}_{sc})$. The important parameter in a reflectivity experiment is the value of intensity, I_r, radiated by the sample, as a function of incident angle θ_{in} or alternatively as a function of modulus of the wave vector transfer **Q** (defined by equation 2.1). The intensity is defined as the flux of the Pointing vector through the detector area [1]. It can be shown that the dependence of the pointing vector to the amplitude of the electric field is quadratic [1]. Therefore, the reflected intensity is proportional to the square of the amplitude of the electric field [1]

$$I_r\left(\left|\vec{Q}\right|\right) \propto \left|\vec{E}_{sc}\left(\vec{K}_{sc}\right)\right|^2$$

Equation 2.19

At this stage of our discussion it is important to notice that the intensity measured by a detector corresponds to the sum of all scattered intensity by all the configurations that the sample can have during the time of the experiment [2]. In the limit of the Ergodic principle [23] we can consider that the measured scattered intensity corresponds to the average scattered intensity (by one realisation of the sample) over the surface of the sample [2, 3, 24]. Therefore, the measured intensity by a detector during a reflectivity experiment is averaged on the plane of the interface over the illuminated area. Hence, the scattered intensity detected by the detector is proportional to:

$$I_r \propto \left|\left\langle \vec{E}_{sc} \right\rangle\right|^2 + \left\langle \left|\delta\vec{E}_{sc}\right|^2 \right\rangle + 2\left\langle \vec{E}_{sc} \right\rangle \cdot \left\langle \delta\vec{E}_{sc} \right\rangle$$

Equation 2.20

where the operator $\langle\rangle$ corresponds to the averaging over the illuminated area. As theinhomogeneities of the refractive index are random, the third term in the right hand side of equation 2.20 is equal to zero, so the expression of the radiated intensity is reduced to $I_r = I_{coh} + I_{incoh}$. The first term in the definition of the reflected intensity(I_{coh}) is called the coherent intensity [2, 3, 19] and is proportional to the field scattered by the reference media. The second term (I_{incoh}) is called the incoherent

intensity and is proportional to the field scattered by the inhomogeneities in the refractive index [2, 19].

Now we wish to clarify the dependence of the coherent and the incoherent intensity to the different components of the wave vector transfer.

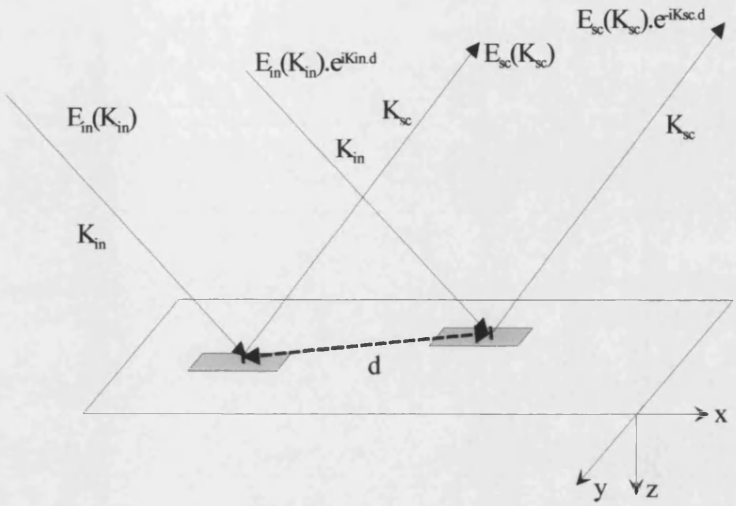

Figure 2.3.Illustration of the invariance of the reflection from a surface under a translation d.

Daillant et al [2] used an elegant argument to demonstrate the independence of the coherent intensity to the in-plane wave vector transfer $\mathbf{Q}_{\parallel}$. If we know the scattered far-field $\mathbf{E}_{sc}$ from an infinite rough surface, produced by a random spatially homogeneous process, the surface profile is given by the equation z = z(r(x,y)). It is clear that a horizontal shift by a vector **d** of the whole surface should not change any physical properties of the system (figure 2.3). However, this horizontal shift will modify the phase of the incident and scattered electric field by a factor, $\exp(i\mathbf{K}_{in}.\mathbf{d})$ and $\exp(-i\mathbf{K}_{sc}.\mathbf{d})$ respectively. Therefore we obtain:

$$\vec{E}_{sc}(z,\vec{r}(x,y)-\vec{d}) = e^{-i(\vec{K}_{sc}-\vec{K}_{in})\cdot\vec{d}}\,\vec{E}_{sc}(z,\vec{r}(x,y))$$

Equation 2.21

As the roughness of the surface is supposed to be spatially homogeneous, the averaging over the surface is invariant under any translation in (x,y) plane [2].

$$\left\langle \vec{E}_{sc}(z,\vec{r}(x,y)-\vec{d})\right\rangle = \left\langle \vec{E}_{sc}(z,\vec{r}(x,y))\right\rangle$$

Equation 2.22

This equality is only possible if during the averaging process the exponential term becomes equal to one, in other words if the in-plane component of the wave vector transfer $\mathbf{Q}_{\parallel}$ is equal to zero. This is possible if the mean value of the scattered field is a Dirac distribution in the reflection direction [2, 3, 19]

$$\left\langle \vec{E}_{sc} \right\rangle = A\delta\left(\vec{Q}_{\parallel}\right)$$

Equation 2.23

The expressions of different components of the wave vector transfer can be calculated from the figure 2.1.

$$\begin{cases} Q_x = K_0\left(\cos\theta_{sc}\cos\Psi - \cos\theta_{in}\right) \\ Q_y = K_0\left(\cos\theta_{sc}\sin\Psi\right) \\ Q_z = K_0\left(\sin\theta_{sc} + \sin\theta_{in}\right) \end{cases}$$

Equation 2.24

As the in-plane wave vector transfer is equal to $\mathbf{Q}_{\parallel} = Q_x\,\mathbf{x} + Q_y\,\mathbf{y}$ the only way to null the $\mathbf{Q}_{\parallel}$ is to have both Q_x and Q_y equal to zero, therefore we obtain the following conditions over the incident, reflection and in-plane angles:

$$\begin{cases} \theta_{sc} = \theta_{in} \\ \Psi = 0 \end{cases}$$

Equation 2.25

The fact that the incidence angle and the angle between the direction of detection and the surface of the sample must be equal (direction at which the detector is positioned) gives coherent intensity the name of specular intensity [1, 3].

Unlike the coherent intensity, the incoherent intensity is a function of $\mathbf{Q}_{\parallel}$ [19]. The specular intensity allows the determination of the structure of material in the direction normal to the surface of the substrate [25, 26]. The incoherent (off-specular) intensity allows determination of the in-plane structure of the material in terms of correlation length [19]. However the separation between these two components of the radiated intensity is not very sharp. One must bear in mind that the intensity measured by the detector is a combination of the specular and off-specular components even in the condition of specular reflectivity [20].

2.4) Reflection coefficient

In the last two sections we defined the behaviour of the electrical field. We showed that the scattered intensity can be decomposed into two parts: one known as the coherent or specular intensity and the other the incoherent or off-specular intensity.

In this section we are interested in the specular intensity, more exactly in the variation of this intensity as a function of the normal to the surface component of the wave vector transfer, Q_z, which is equal to (in case of specular reflection):

$$Q_z = \frac{4\pi}{\lambda}\sin\theta_{in}$$

Equation 2.26

In order to calculate the dependence of the reflected intensity we first must calculate the reflection coefficient, $R(Q_z)$, and we will discuss the difference between the reflection intensity as a function of the orientation of the electric field.

Consider the reflection and refraction of a plane wave incident on a single boundary separating two media of refractive index n_1 and n_2 (Figure 2.4).

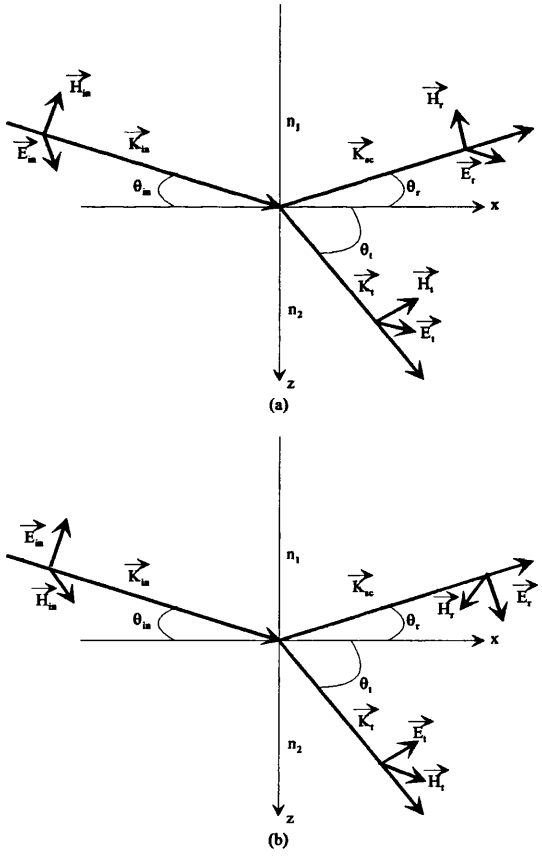

Figure 2.4. Reflection of a polarised beam from the interface between two media. a) Case of a s polarised wave. b) Case of a p polarised wave.

Both media can be absorbing, and therefore the refractive index is a complex quantity [1]. We define the plane of incidence as the plane containing the direction of wave propagation ($\mathbf{K_{in}}$) and the normal to the boundary, we choose (x,z) as the plane of incidence. The angle of incidence, θ_{in}, is defined as the angle between the direction of propagation and the boundary (Figure 2.4). In Figure 2.4 two cases are shown: (a) the electric field is perpendicular to the plane of incidence (perpendicular polarization). This case is also called "s polarization" (*senkrecht*, "perpendicular" in German) or "TE wave" (electric field is transverse to the direction of wave propagation). In the second case (b) the electric field is in the plane of incidence (parallel polarization). This case is also called " p polarization" (p for parallel) or "TM wave" (magnetic field is transverse to the direction of wave propagation). These two waves are independent. In fact, for a two-dimensional problem the electromagnetic wave can be separated into two independent waves: TE and TM (this decomposition is only correct if the refractive index is independent of y direction) [1].

In the two next sub-sections we will calculate the reflection coefficient for each of these waves.

2.4.1) Reflection coefficient for a s polarised field

Let us consider the perpendicular polarization. We suppose the incoming wave to be a plane wave, and by using Maxwell's equations (Equation 2.2) it is easy to show [27] the following relationships:

$$a: \vec{E} = \vec{E}_0 e^{-i\vec{K}\cdot\vec{r}}$$
$$b: \vec{H} = \sqrt{\frac{\varepsilon}{\mu}} \frac{\vec{K} \times \vec{E}}{|\vec{K}|}$$
$$c: \vec{r} = x\vec{x} + y\vec{y} + z\vec{z}$$

Equation 2.27

From the Figure 2.4.a we can write:

$$\vec{K}_i = K_i(\cos\theta_i \vec{x} + \sin\theta_i \vec{z})$$

Equation 2.28

We define β_i as $\beta_i = K_i \cos\theta_i$ and q_i as $q_i = K_i \sin\theta_I$, we then write the incident field E_{yi} with magnitude E_0 as:

$$E_{yi} = E_0 e^{-i(q_i z + \beta_i x)}$$

Equation 2.29

K_i is the wave number in medium 1 and K_0 is the wave number in free-space. The relationship between them is given by $K_i = n_1.K_0$ [1]. As the reflected and transmitted beam satisfy the wave equation we can therefore write:

$$E_{yr} = r_s E_0 e^{-i(-q_r z + \beta_r x)}$$
$$E_{yt} = t_s E_0 e^{-i(q_t z + \beta_t x)}$$

Equation 2.30

Where r_s and t_s are the complex reflection and transmission coefficient. The expression for q_r, β_r, q_t, β_t are given by:

$$q_r = K_0 n_1 \sin\theta_r$$
$$\beta_r = K_0 n_1 \cos\theta_r$$
$$q_t = K_0 n_2 \sin\theta_t$$
$$\beta_t = K_0 n_2 \cos\theta_t$$

Equation 2.31

Where θ_r and θ_t are the angle of reflection and the angle of transmission respectively. Now we apply the continuity condition to the tangential component of the electric and magnetic field at the boundary for z = 0 [22]. For a homogeneous media the tangential component of the electric field is conserved [22], we can then write:

$$E_{yi} + E_{yr} = E_{yt}$$

Equation 2.32

For this relation to hold at z=0, all phases must be equal [22]. Therefore we get the phase matching condition:

$$\beta_i = \beta_r = \beta_t$$

Equation 2.33

From this condition we obtain the law of reflection, which justifies the reason why this development can only be applied to the specular reflection:

$$\theta_i = \theta_r$$

Equation 2.34

And also we find Snell's law [1]:

$$n_1 \cos\theta_i = n_2 \cos\theta_t$$

Equation 2.35

From these two equations we find the energy conservation condition on the reflection and transmission coefficient [1]:

$$1 + r_s = t_s$$

Equation 2.36

Now we wish to apply the continuity condition on the tangential component of the magnetic field, at z = 0. To obtain an expression for the tangential component of the magnetic field we use the Maxwell's third equation (equation 2.2.c) and the relationship between the magnetic flux and the magnetic field (equation 2.4).

$$\begin{cases} H_{xi} = -\dfrac{E_0}{Z_1} e^{-i(q_i z + \beta_i x)} \\ H_{xr} = -\dfrac{r_s E_0}{Z_1} e^{-i(-q_i z + \beta_i x)} \\ H_{xt} = -\dfrac{t_s E_0}{Z_2} e^{-i(q_t z + \beta_t x)} \end{cases}$$

Equation 2.37

where Z_1 and Z_2 are the ratio between the tangential component of E_y and H_x (called also the wave impedance [27])

$$\begin{cases} Z_1 = \dfrac{\omega \mu_1}{q_i} \\ Z_2 = \dfrac{\omega \mu_2}{q_t} \end{cases}$$

Equation 2.38

where ω is the angular frequency of the wave and μ_1 and μ_2 are the permeability of the medium 1 and 2 respectively. Now we apply the continuity of the tangential component of the magnetic field at z = 0

$$H_{xi} + H_{xr} = H_{xt}$$

Equation 2.39

Then we obtain the following energy conservation relation between the reflection and transmission coefficient:

$$\frac{1-r_s}{Z_1}=\frac{t_s}{Z_2}$$

Equation 2.40

Finally from equation 2.40 and 2.36 we obtain the Fresnel formula [1]:

$$r_s=\frac{Z_2-Z_1}{Z_2+Z_1} \quad \text{(a)}$$

$$t_s=\frac{2Z_2}{Z_2+Z_1} \quad \text{(b)}$$

Equation 2.41

In a particular case where the magnetic permeability of the medium can be neglected ($\mu_1 = \mu_2 = \mu_0$), equations 2.41.a and 2.41.b can be reduced to a more familiar form (Fresnel form):

$$r_s=\frac{n_1\sin\theta_i-n_2\sin\theta_t}{n_1\sin\theta_i+n_2\sin\theta_t} \quad \text{(a)}$$

$$t_s=\frac{2n_1\sin\theta_i}{n_1\sin\theta_i+n_2\sin\theta} \quad \text{(b)}$$

Equation 2. 42

2.4.2) Reflection coefficient for a p polarised field

In this section we develop an expression for the complex reflection (r_p) and transmission coefficient (t_p) in the case of a parallel polarised wave. The x component of the electric field can be written as:

$$E_{xi}=E_0\sin\theta_i e^{-i(q_i z+\beta_i x)}$$
$$E_{xr}=r_p E_0\sin\theta_r e^{-i(-q_r z+\beta_r x)}$$
$$E_{xt}=t_p E_0\sin\theta_t e^{-i(q_t z+\beta_t x)}$$

Equation 2.43

As we explained in the last sub-section Snell's law and the condition $\theta_i = \theta_r$, hold also here. By using Maxwell's first equation (equation 2.2.a) and the relationship between the displacement vector, **D**, and the electric field (equation 2.4) we can write the relationship between the tangential component of the electric field and magnetic field.

$$E_x = -\frac{1}{j\omega\varepsilon}\frac{\partial}{\partial z}H_y$$

Equation 2.44

Now by applying the continuity conditions at the boundary z = 0, to the tangential component of the magnetic and electric field we obtain the following Fresnel formula [1]:

$$a: r_p = \frac{Z_2 - Z_1}{Z_2 + Z_1}$$
$$b: tp = \frac{2Z_2}{Z_2 + Z_1}\frac{\sin\theta_i}{\sin\theta_t}$$

Equation 2.45

Where Z_1 and Z_2 are given by the formula:

$$Z_1 = \frac{q_i}{\omega\varepsilon_1}$$
$$Z_2 = \frac{q_t}{\omega\varepsilon_2}$$

Equation 2.46

Where ε_1 and ε_2 are the permittivity of the medium 1 and 2 respectively. If the magnetic permeability of each medium can be neglected ($\mu_1 = \mu_2 = \mu_0$) then equation 2.46 would reduce to a more familiar form:

$$r_p = \frac{\left(\frac{1}{n_2}\right)\sin\theta_t - \left(\frac{1}{n_1}\right)\sin\theta_i}{\left(\frac{1}{n_2}\right)\sin\theta_t + \left(\frac{1}{n_1}\right)\sin\theta_i}$$
$$t_p = \frac{\left(\frac{2}{n_1}\right)\sin\theta_i}{\left(\frac{1}{n_2}\right)\sin\theta_t + \left(\frac{1}{n_1}\right)\sin\theta_i}\frac{\sin\theta_i}{\sin\theta_t}$$

Equation 2.47

2.5) Brewster angle and total reflection

In the last section we calculated the complex reflection and transmission coefficient for the electric field. We showed that the reflection coefficient depends on the polarization of the electric field, on the refractive index of the two medium and

finally on the incidence angle θ_i. In this section we will show that under particular circumstances the reflection coefficient or the transmission coefficient become equal to zero. We will discuss first the case where the reflection coefficient for a p polarized wave becomes equal to zero, then we will be interested to the total reflection case. Finally we will show the analogy between the scattering density and the refractive index.

In the following chapters we will describe experimental results obtained by use of Brewster Angle Microscopy (BAM) whose principle is based on the existence of the Brewster angle and we will show that the shape of the reflectivity profile near the total reflection region depends strongly on the nature and morphology of the surface.

2.5.1) Brewster angle

Let us examine the Fresnel formula given by equations 2.41 and 2.45, where n_1 and n_2 are real and positive (lossless medium and no amplifying [22]). Figure 2.5 shows the variation of the reflection and transmission coefficient as a function of the incident angle θ_i.

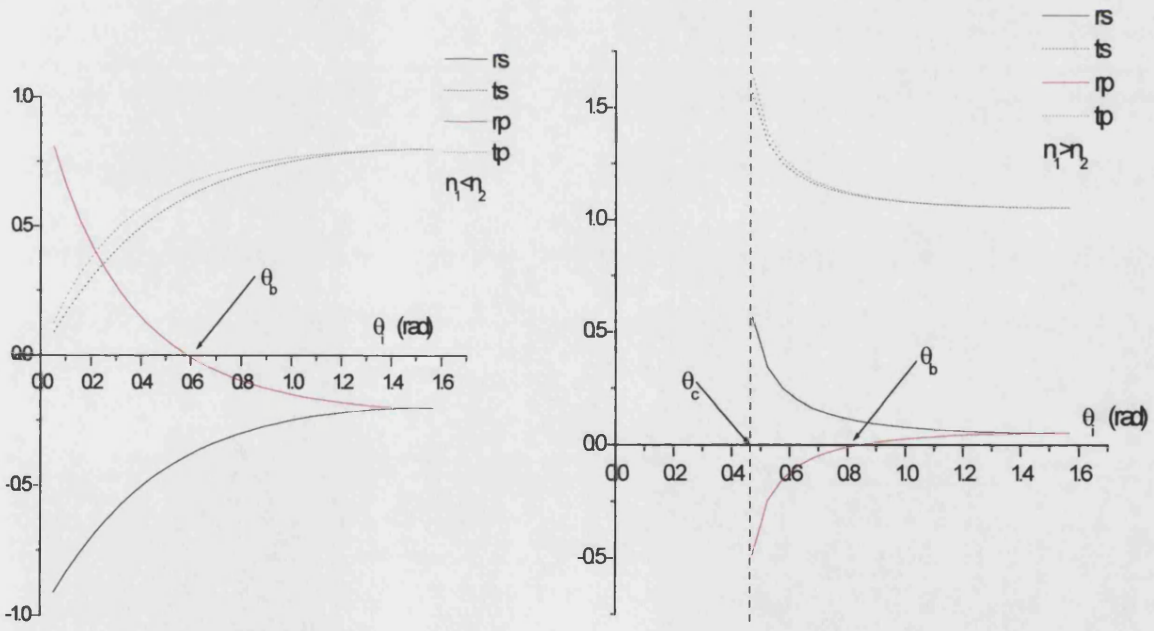

Figure 2.5. Variation of the reflection and transmission complex coefficient as a function of the incident angle. The figure in left hand side represent the case where $n_1<n_2$ ($n_1 = 1$ and $n_2 = 1.5$)and the figure in right hand side illustrates the case where $n_1>n_2$.($n_1 = 1.5$ and $n_2 = 1$)

We can notice that the p polarized reflection coefficient becomes equal to zero at a particular angle, for both cases $n_1 > n_2$ and $n_1 < n_2$. The reflection coefficient r_p for parallel polarization becomes equal to zero when:

$$\sin\theta_i = \frac{n_1}{n_2}\sin\theta_t$$

Equation 2.48

By using Snell's law and the addition formula of cosine we can re-write equation 2.48 as:

$$\sin\theta_i = \frac{n_1}{n_2}\left[1-\left(\frac{n_1}{n_2}\right)^2\cos^2\theta_i\right]^{\frac{1}{2}}$$

Equation 2.49

By using some algebra, we solve the equation 2.49 for θ_i and we get:

$$\theta_i = \frac{\pi}{2} - \theta_b = \tan^{-1}\left(\frac{n_1}{n_2}\right)$$

Equation 2.50

This incident angle θ_b is called Brewster angle [1]. At this angle all the incident power passes into the second medium. Note that this occurs only when the incident field is polarised in the plane of incidence. If a wave consisting of both parallel and perpendicular polarizations is incident on the boundary at Brewster angle, the component with parallel polarization is all transmitted into the second medium and the reflected wave consists only of perpendicular polarization. It is easy to prove that at Brewster angle, $\theta_b+\theta_t=\pi/2$.

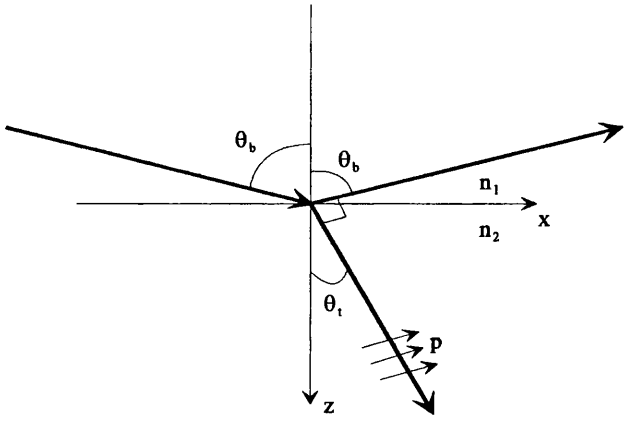

Figure 2.6. Illustration of the reflection at an interface at Brewster angle. At this incident angle all the p polarised component of the incident wave is transmitted and only the s polarised component is reflected.

This means that the electric field in the second medium is polarized such that all the polarized vectors **P** are pointed in the direction of the reflected wave (Figure 2.6).

2.5.2) Total reflection

Let us next examine the case when medium 2 is less optically dense than medium 1, that is $n_1 > n_2$. Figure 2.5 shows the reflection and transmission complex coefficients. Note that for the parallel polarization there is still a Brewster angle. Since $n_1 > n_2$, the transmitted angle is smaller than the incident angle [27]. Therefore, there exists a critical angle, θ_c, below which the transmission angle becomes equal to zero. In other words there exists a critical angle below which the transmission coefficient is not any more defined (transmission coefficient becomes purely imaginary [1]). The value of the critical angle is given by Snell's law:

$$\theta_c = \cos^{-1}\left(\frac{n_2}{n_1}\right)$$

Equation 2.51

When the incident angle is smaller than the critical angle the wave is totally reflected, there is no real power transmitted through the boundary [1]. Therefore, below the critical angle the value of the modulus of the reflection coefficient is equal to one.

2.5.3) Relation between the Critical Angle and the Scattering length density in the case of X-ray and Neutron

In the last two sub-sections we discussed the behaviour of transmission and reflection coefficients as a function of the incidence angle for an electromagnetic wave, and we demonstrated that their behaviours are strongly dependent on the value of the refractive index. In this sub-section we will discuss the case of X-ray and neutron radiations. We will show how the interaction between these two radiations and matter can be express through the refractive index.

X-rays interact principally with the electrons, and weakly with atomic nuclei. In contrary neutrons interact principally with nuclei. However, in both cases a photon (or a neutron in case of neutrons) which meets an atom can undergo one of the three following events: elastic scattering, inelastic scattering, absorption. The scattering power of the sample (the nature of the interaction and the amplitude of the scattered

signal) is characterised by a coefficient called the scattering length, b [2, 3]. This coefficient is a complex number and can be positive or negative [3]. The notation b is used for neutron but we use it for X-rays as well. b is positive for X-ray (Thomson–scattering [2]) and also for the interaction between neutron and most of nuclei. The complex part of the scattering length corresponds to the capture of the photon (or neutron) in a non-radiative process (e.g. absorption) [3]. In order to link the refractive index, n, to the scattering length, b, we use equations 2.12 and 2.15. These equations correspond to the propagation of a wave in a medium represented by the interaction potential per unit of volume U(r), in equation 2.12, and V(r), in equation 2.15. Let us first assume that the amplitude of the scattering is independent of the direction, therefore the scattering length density is the same for all direction. Let us also assume that φ(r), is the density of objects of scattering length b.

Therefore, the expression of the interaction potential is given by:

$$U(r) = V(r) = 4\pi\varphi(r)b$$

Equation 2.52

If in this equation φ(r)b can be replaced by its space average Nb, by using the equation 2.12 we obtain the refractive index n as:

$$n^2 = 1 - \left(\frac{4\pi}{K_0^2}\right)Nb$$

Equation 2.53

Equation 2.53 links the refractive index, n, to the scattering length. It turns out that in the case of neutrons and X-rays [2], because they give small values of Nb, the average can be made safely. With these small values the equation 2.53 can be written in the first approximation as:

$$n \cong 1 - \left(\frac{2\pi}{K_0^2}\right)Nb = 1 - \left(\frac{\lambda^2}{2\pi}\right)Nb$$

Equation 2.54

Now by decomposing the scattering length in to a real and an imaginary part we obtain:

$$n \cong 1 - \left(\frac{2\pi}{K_0^2}\right)\left(Nb' + iNb''\right) = 1 - \delta - i\beta$$

Equation 2.55

Where Nb' is linked to the scattering power of the scattering centre, and Nb" to its absorption power [3]. However for most materials made of polymer the absorption power is negligible in front of the scattering power of the centre therefore, the imaginary part of equation 2.55 can be neglected [3], so:

$$n \cong 1 - \delta$$

Equation 2.56

In the following part of this work we will consider that the refractive index is real and we will neglect the absorption process. In the case of neutrons, the value of the scattering length is pseudo-randomly defined through the elementary element table [3]. In the case of X-rays the value of the scattering length increases as a function of the atomic number [22]. A long derivation of refraction index can be found in Jackson [22]. He showed that for a large enough photon energies ($\hbar\omega$), the dielectric constant approaches the "plasma limit"(the characteristic frequency of each material [22]) and:

$$\varepsilon(\omega) \cong 1 - \frac{\omega_p^2}{\omega^2}$$

Equation 2.57

where the "plasma frequency" is

$$\omega_p^2 = \frac{4\pi\varphi Ze^2}{m}$$

Equation 2.58

Where Z is the atomic number, e is the elementary charge of an electron ($e = 1.6\times10^{-19}$ C) and m is the mass (Kg) of the material. The refractive index is defined as the square root of the product of the magnetic permeability and the dielectric constant (equation 2.7). As we assume the material does not have any magnetic properties ($\mu = 1$) since the refractive index is close to unity we can write in first approximation the refractive index as:

$$n \cong 1 - \left(\frac{2\pi}{K_0^2}\right)\varphi Z r_0$$

Equation 2.59

Where $r_0 = e^2 / mc^2$ is the classical electron radius ($r_0 = 2.818 \times 10^{-5}$ Å). By comparing equation 2.59 and 2.54 we notice that in the cases of X-rays the scattering length density is equal to:

$$Nb' = r_0 \varphi Z$$

Equation 2.60

and the density of the scattering centre, φ, is equal to:

$$\varphi = \frac{\varphi_m N_A}{W}$$

Equation 2.61

Where φ_m is the density of material ($g.cm^{-3}$), N_A is the Avogadro number ($N_A = 6.022 \times 10^{23}$ mol^{-1}) and W is the relative molecular mass ($g.mol^{-1}$).

We showed that the refractive index and the scattering length of the material can be linked together. We use the argument that the value of the scattering length density (Nb $Å^{-2}$) is small compared to 1. With these values, the vector character of the electromagnetic radiation does not make any difference [2], therefore to calculate the reflection coefficient we will consider only the perpendicular polarization [2]. We showed that in the case when the medium 2 is optically less dense than medium 1, there exists a critical angle below which the entire incident wave is reflected. Now consider that the scattering length density of the medium 1 is Nb_1 and the scattering length density of medium 2 is Nb_2. By introducing the equation 2.56 into the equation 2.51 we obtain:

$$\cos\theta_c = \frac{1-\delta_2}{1-\delta_1}$$

Equation 2.62

As in the case of X-rays and neutrons δ is of the order of 10^{-6}, so θ_c is very small (<1°) [2]. Therefore total reflection occurs at glancing angles of incidence. Since θ_c is small, a series expansion can be used for the cosine term, also as δ_1 and δ_2 are small we can approximate the right hand side of the equation 2.63 to the first order approximation. So the value of the critical angle is given by:

$$\theta_c \cong \sqrt{\frac{4\pi}{K_0^2}}\sqrt{Nb_2 - Nb_1} = \sqrt{\frac{1}{\pi}}\lambda\sqrt{Nb_2 - Nb_1}$$

Equation 2.63

Or alternatively we can define the value of the critical normal transfer moment, Q_{zc}, as:

$$Q_{zc} \cong \sqrt{16\pi}\sqrt{Nb_2 - Nb_1}$$

Equation 2.64

In a reflectivity experiment what is detected by the spectrometer is the intensity reflected by sample and not the electrical reflected field. As we notice (equation 2.19) the scattered intensity is proportional to the modulus of the averaged electrical scattered field. Therefore, by using the relationship between the electrical scattered field and the incident electrical field (equation 2.43) in the case of a s-polarized field we obtain:

$$I(Q_z) \propto I_0 |r_s|^2 = I_0 R(Q_z)$$

Equation 2.65

Therefore the important parameter that we measure during a reflectivity experiment is the variation of the reflection coefficient $R(Q_z)$ as a function of Q_z. Figure 2.7 and table 2.1 represent the shape of the reflection coefficient R and the values of the scattering length density for several materials respectively.

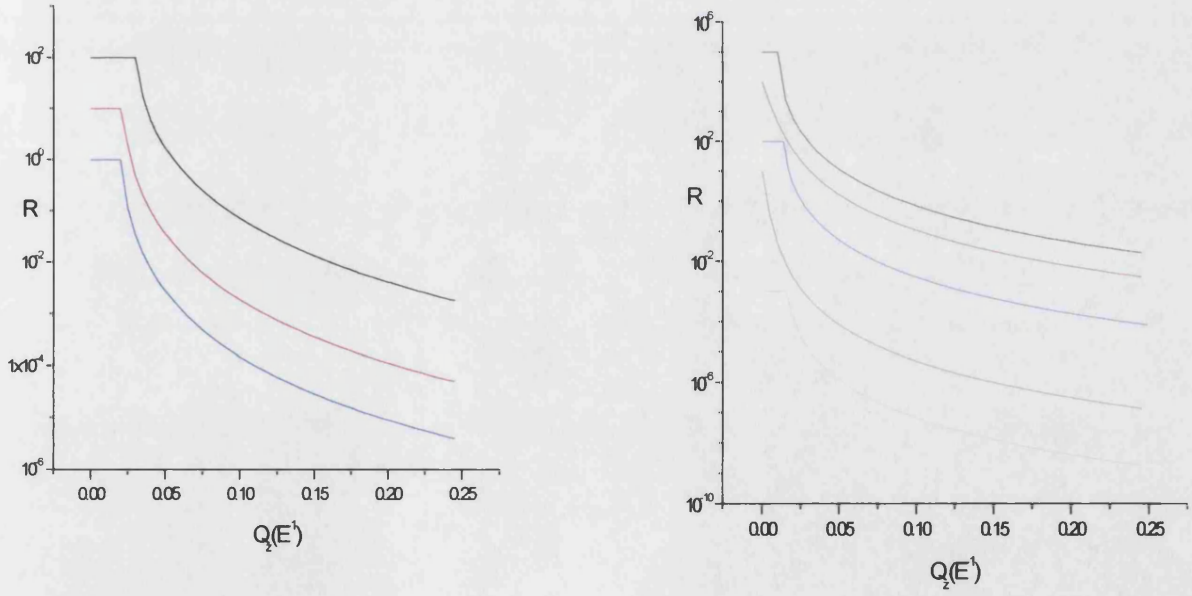

Figure 2.7. Reflectivity profiles from different interfaces. The profiles have been rescaled. The figure on the left hand side represents the reflectivity profiles in the case of X-ray scattering (black : air/silicon, red: water/silicon, blue: air/water). The figure on the right hand side represents the reflectivity profile in the case of neutron scattering (black: air/silicon, red: silicon/water, Blue: silicon/D_2O, green: air/water, yellow: air/D_2O).

	Nb neutron ($Å^{-2}$)	Nb X-rays($Å^{-2}$)	Q_{zc} ($Å^{-1}$), air (x-rays)	Q_{zc} ($Å^{-1}$), water (x-rays)	Q_{zc} ($Å^{-1}$), air (neutron)	Q_{zc} ($Å^{-1}$), silicon (neutron)
air	0	0	×	×	×	×
silicon	2.073×10^{-6}	2.012×10^{-5}	0.03179	0.02313	0.01021	0
Water	-5.61×10^{-7}	9.475×10^{-6}	0.02182	0	×	×
D_2O	6.366×10^{-6}	9.475×10^{-6}	0.02182	0	0.01788	0.01469

Table 2.1. Values for the scattering length density of different materials and the critical transfer moment at different interfaces.

2.6) Commonly used techniques

In the last section we showed the relationship between the scattering density of the material and the critical angle. In this section we will discuss the reflection coefficient from a multilayer on the top of a substrate. Kiessing's work showed that the periodicity of the interference fringes appearing in the reflectivity profile depends on the structure (thickness, density, roughness) of the film deposited on the top of a substrate. Several techniques have been developed to extract from the reflectivity profile information about the structure of the deposited material [2]. These methods can be divided into two categories: the discrete (but exact) methods and the continuous (but approximate) methods. In this section we will first discuss the discrete methods and we will show how one can consider the continuous method as an approximate to the discrete method.

2.6.1) Discrete methods

These methods are generally exact and based on the optical calculation and principles [24]. They are very useful to calculate the reflectivity profile from a series of sharp interfaces (or discrete layers). In order to use these techniques to model the interface one must divide the interface into a sequence of steps (Figure 2.8) of constant scattering density and of thickness d.

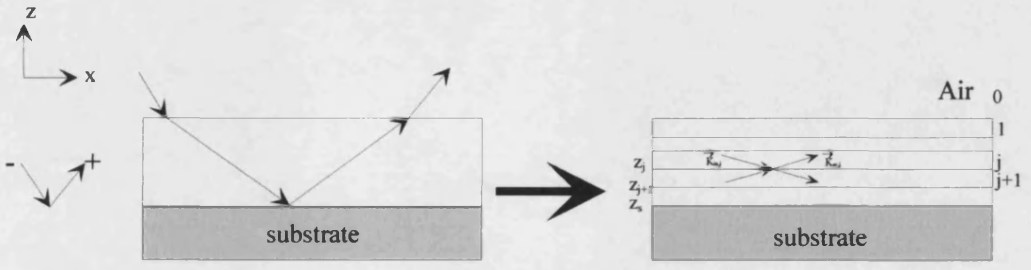

Figure 2.8 . Illustration of plane of incidence for a stratified medium. The signs – (incident wave) and + (reflection wave) label the direction of propagation of the wave; Air is labelled medium 0 and the strata are identified by $1\leq j\leq N$ layers in which upwards and downwards waves travel.

The reflectivity coefficient is calculated by matching the electrical field and its space differential (in z direction) at each interface [2]. There are two widely used techniques: the optical matrix method [1, 24] (or the dynamical theory) and the equivalent recursive technique developed initially by Parrat [28] known as the Parrat formalism.

Let us consider the case of a plane wave illuminating the surface of a stratified media (figure 2.8). Consider z_{j+1} as a depth which marks the interface between the j and j+1 layers. The wave travelling through the material would be transmitted and reflected at each interface. The amplitude of the upward and downward travelling wave in the j^{th} stratum, for example, are defined by A^{+}_{j} and A^{-}_{j}. Therefore, the tangential component of the electric field in the j^{th} medium (using Snell's law) is given by:

$$E_j(x,z) = \left(A_j^{+} e^{ik_{in,j}z} + A_j^{-} e^{-ik_{in,j}z}\right) e^{i(\omega t - k_{in,x,j}x)}$$

Equation 2.66

The condition of continuity of the tangential component of the electric field [22] and the conservation of the $k_{in,x,j}$ at the depth z_{j+1} of interface j / j+1 lead to the relation:

$$A_j^{+} e^{ik_{in,j}z_{j+1}} + A_j^{-} e^{-ik_{in,j}z_{j+1}} = A_{j+1}^{+} e^{ik_{in,j+1}z_{j+1}} + A_{j+1}^{-} e^{ik_{in,j+1}z_{j+1}}$$

Equation 2.67

In section 2.4 we used the continuity condition on the tangential component of the magnetic field in order to calculate the Fresnel formula for the reflection coefficient from a simple interface. This condition in the case of a plane wave is equivalent to the continuity of the differential of the electric field at the interface between two media j and j+1 [27]. Therefore we can write:

$$A_j^{+} k_{in,j} e^{ik_{in,j}z_{j+1}} - A_j^{-} k_{in,j} e^{-ik_{in,j}z_{j+1}} = A_{j+1}^{+} k_{in,j+1} e^{ik_{in,j+1}z_{j+1}} - A_{j+1}^{-} k_{in,j+1} e^{-ik_{in,j+1}z_{j+1}}$$

Equation 2.68

The combination of these two equations (equation 2.68 and 2.69) allows us to express the value of the amplitude of the reflected field (A^{+}_{j}) in the media j as a function of the value of the amplitude of the reflected field and incident field of the media j-1. The reflection coefficient is defined as the modulus of the ratio of the reflected electric field and the incident electric field [2] at the surface of the material. Therefore,

the knowledge of the total reflected field at the surface of the sample is necessary. There are two ways of calculating the reflectivity coefficient, by using the matrix method or using a recursive method.

2.6.1.1) Matrix method

This method is based on the standard optical matrix technique described in Born and Wolf [1] andis referred to as matrix method or dynamical theory [3, 24].

The combination of equation 2.68 and 2.69 is written in the form of a matrix, which links the electric field and its first derivative at the depth z_j to the same quantities at a depth z_{j+1} for each layer [1]. Therefore, each layer is defined by a characteristic matrix M_j

$$M_j = \begin{bmatrix} \cos\beta_j & -\left(\frac{i}{k_{in,j}}\right)\sin\beta_j \\ -ik_{in,j}\sin\beta_j & \cos\beta_j \end{bmatrix}$$

Equation 2.69

where $k_{in,j} = n_j \sin\theta_j$ and $\beta_j = k_{in,j} \times (z_{j+1}-z_j)$.

Each layer adds another reflected wave, all of which have to be added together, taking into account of their relative phases. Therefore, the electric field at the surface of the sample is linked to the electric field at the surface of the substrate by:

$$\begin{bmatrix} E(k_{in,0}, z_1) \\ \frac{\partial E(k_{in,0}, z_1)}{\partial z} \end{bmatrix} = \prod_{j=1}^{N} M_j \begin{bmatrix} E(k_{in,s}, z_s) \\ \frac{\partial E(k_{in,s}, z_s)}{\partial z} \end{bmatrix}$$

Equation 2.70

All the matrices involved in the above product are 2×2 matrices. So that their product which is called the transfer matrix, M is also a 2×2 matrix.

$$M = \prod_{j=1}^{N} M_j = \begin{bmatrix} M_{11} & M_{12} \\ M_{21} & M_{22} \end{bmatrix}$$

Equation 2.71

and the reflectivity is given by[1, 24]

$$R = \left| \frac{(M_{11} + M_{12}k_{in,s})k_{in,0} - (M_{21} + M_{22}k_{in,s})}{(M_{11} + M_{12}k_{in,s})k_{in,0} + (M_{21} + M_{22}k_{in,s})} \right|^2$$

Equation 2.72

2.6.1.2) The recursive method

This method has been developed by L.G. Parrat [28] for reflection of X-ray at glancing angles and is known as Parrat formalism.

The complex reflection coefficient can be obtained by dividing the difference between equation 2.68 and 2.69 by their sum and writing the result as a recursion formula.

$$r_{j-1,j} = e^{-i4k_{j-1}\frac{z_j - z_{j-1}}{2}} \frac{r_{j,j+1} + F_{j-1,j}}{r_{j,j+1}F_{j-1,j} + 1}$$

Equation 2.73

where

$$r_{j,j+1} = \frac{A_j^+}{A_j^-} e^{-i2k_j\frac{z_{j+1} - z_j}{2}}$$

Equation 2.74

and the factor $F_{j-1,j}$ in equation 2.73 is given by:

$$F_{j-1,j} = \frac{\sqrt{(Q_z^2 - Q_{z,c_{j-1}}^2)} - \sqrt{(Q_z^2 - Q_{z,c_j}^2)}}{\sqrt{(Q_z^2 - Q_{z,c_{j-1}}^2)} + \sqrt{(Q_z^2 - Q_{z,c_j}^2)}}$$

Equation 2.75

One has to solve these three equations by starting at bottom medium (substrate). The reflection coefficient is then given by

$$R = \left| \frac{E_1^R}{E_1} \right|^2$$

Equation 2.76

where E^R_1 is the total reflected electric field at the surface of the stratified medium and E_1 is the incident electric field at the same surface.

The full dynamical theory is exact. In this technique one has to divide the structure of the sample in to N layers. The algebra used for a system divided into 2 layers is

straightforward but very tedious for N > 3. Therefore, to calculate or to model a reflectivity profile numerical calculations are necessary. At the earliest time of the reflectivity experimentation the calculation time and power of the used computers to simulate a reflectivity profile by using dynamical theory was limited. Therefore, it was more useful to use an approximate technique in order to have an insight into the physical meaning of the observed phenomena. However, at the present time computation power has increased and allows one easily calculate structure up to 200 layers very quickly.

2.6.2) Continuous method

In this technique one assumes the scattering density as a continuous function of the space parameter z. Gibaud [2] degraded the analytical form of the reflectivity coefficient calculated by dynamical theory in order to obtain an approximate formula known as first order Born approximation or kinematical theory [2, 3]. Here we will only present the important points and hypothesis.

The complex reflection coefficient from a thin film of thickness h is given by

$$r = \frac{r_{0,1} + r_{1,2} e^{-iQ_{z1}h}}{1 + r_{0,1} r_{1,2} e^{-iQ_{z1}h}}$$

Equation 2.77

where $r_{1,2}$ and $r_{0,1}$ are the Fresnel's formula for the reflectance from the interface between the medium 1 / 2 and 0 / 1 respectively (figure 2.9).

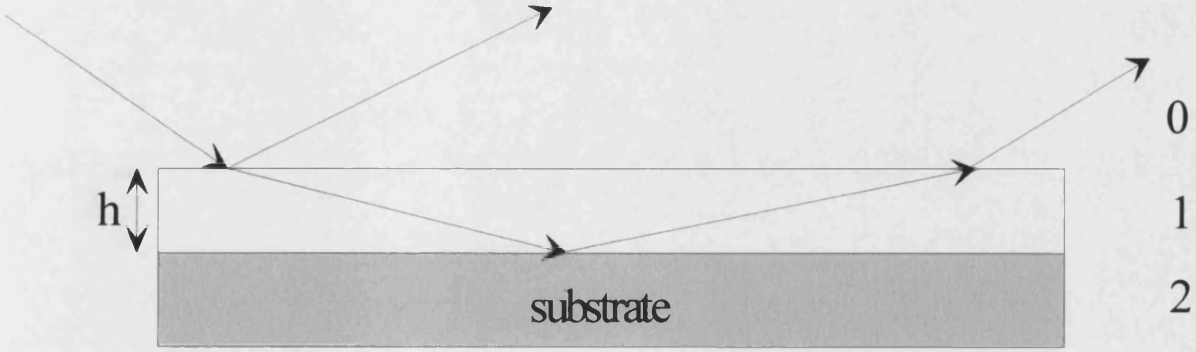

Figure 2.9. Illustration of reflection from a thin film of thickness h deposited on a substrate.

In the case where reflectance are real

$$R(Q_{z,0}) = |r|^2 = \frac{r_{0,1}^{\ 2} + r_{1,2}^{\ 2} + 2r_{0,1}r_{1,2}\cos(Q_{z,1}h)}{1 + r_{0,1}^{\ 2}r_{1,2}^{\ 2} + 2r_{0,1}r_{1,2}\cos(Q_{z,1}h)}$$

Equation 2.78

Figure 2.10 illustrates a calculated reflectivity profile for a film, 100Å in thickness, on a silicon substrate where the interfaces between the film and the air and film and substrate are infinitely sharp.

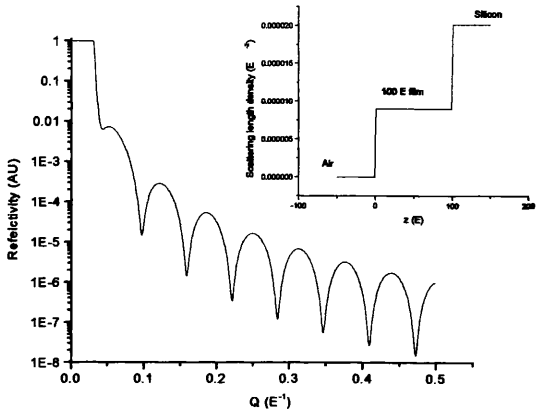

Figure 2.10. Represents the calculated reflectivity profile from a film of 100 Å thick (scattering length density is assumed to be equal to (9×10^{-6} $Å^{-2}$) deposited on a silicon substrate. The insert in top right corner represents the scattering length density profile.

The reflectivity profile contains series of maxima and minima which characterise the thickness of the film [26]. The differential (as a function of the space parameter h) of the equation 2.78 is equal to zero only if the argument of the sine function ($Q_{z1}\times h$) are even multiples of π [26]. Consequently the position of the two successive minima yield a thickness directly from

$$\Delta Q_{z,1}h = \pi \Rightarrow h = \frac{\pi}{\Delta Q_{z,1}}$$

Equation 2.79

And by neglecting the variation of the refractive index from one media to the other we find

$$h \approx \frac{\pi}{\Delta Q_{z,0}}$$

Equation 2.80

Under general considerations the reflectance are complex quantities and can be expressed as:

$$r_{j,j+1} = \frac{Q_{z,j} - Q_{z,j+1}}{Q_{z,j} + Q_{z,j+1}}$$

Equation 2.81

where $Q_{z,j} = (4\pi/\lambda) \times \sin\theta_j = (Q_{z,j}^2 - Q_{c,j}^2)^{0.5}$. $Q_{c,j}$ is the critical transfer moment of the media j.

The first approximation is to neglect the multiple reflections (because the interaction between the matter and the radiation is supposed to be very weak [2, 3]). Therefore, the cross term in the denominator of equation 2.77 ($r_{0,1}\, r_{1,2}\, e^{-iQ_{z1}h}$) can be neglected [2]. Under this approximation equation 2.77 is approximately equal to

$$r \approx r_{0,1} + r_{1,2} e^{-iQ_{z1}h}$$

Equation 2.82

This expression can be generalized to a system of stratified media. The second approximation consists of neglecting the absorption and the refraction in the material in the phase factor [2]. This approximation is consistent if the incident angle of reflection is far from the critical angle ($\theta > 3 \times \theta_c$) [2]. Therefore, the transfer moment, Q_{zj}, is independent of the index j and we can write the reflection coefficient for a stratified media formed of N layers as:

$$R(Q_z) = \left| \sum_{j=0}^{N} r_{j,j+1} e^{-iQ_z z_j} \right|^2$$

Equation 2.83

At this stage we assume that the variations of the transfer moment, Q_z, are small from one media to another one [2]. Therefore the sum in the denominator of the equation 2.81 can be approximate in first order to $2 \times Q_z$. By considering this assumption and the

fact that the stratified media is supposed to be continuous we can replace the sum term by an integral term.

$$R(Q_z) = R_F(Q_z)\left|\frac{1}{Nb_s}\int_{-\infty}^{+\infty}\frac{\partial\rho(z)}{\partial z}e^{-iQ_z z}dz\right|^2$$

Equation 2.84

where $R_F(Q_z)$ is the reflection from a sharp interface [2, 3].

$$R_F(Q_z) = \frac{16\pi(Nb_s)^2}{Q_z^4}$$

Equation 2.85

Nb_s is the scattering length density of the substrate and $\rho(z)$ is the scattering length density of the stratified media.

The equation 2.84 has a very simple form. However, it can yield a simple and powerful result. If the scattering density of the substrate is known, then dividing the observed reflectivity profile by the ideal, Fresnel reflectivity yields the square of the Fourier transform of the normalized scattering length density gradient in the specimen.

If $Qz_{,0} > 3 \times Q_z$, by using equation 2.84 and 2.85 we can notice that the film factor ($Q_{z,0}^4 \times R(Q_{z,0})$) is proportional to the Fourier transform of the gradient of the scattering density. If the interfaces are supposed to be sharp, equation 2.84 suggests that

$$R(Q_{z,0})Q_{z,0}^4 \propto Nb_1^2 + (Nb_2 - Nb_1)^2$$

Equation 2.86

in its asymptotic level (figure 2.11). From this result it is clear that the interface with largest contrast will dominate the asymptotic level of the film factor.

While it is clear that the oscillations in reflectivity profile result from the thickness of the film, the amplitude of the oscillation will depend on the contrast between the two interfaces. Consequently, the higher the contrast the more pronounced will be the oscillation [3, 26].

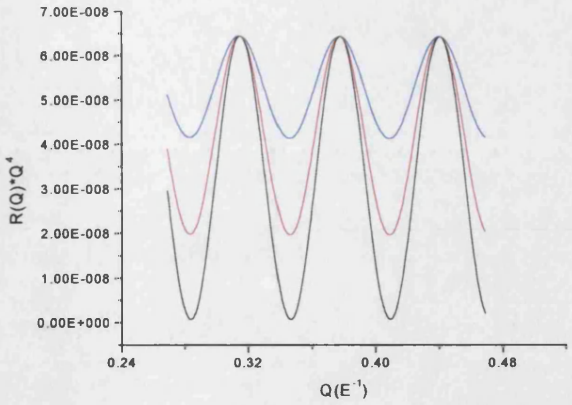

Figure 2.11. Illustration of the variation of the film factor as a function of the scattering length density of the film. A film of 100 Å on top of a silicon substrate is considered. Different scattering length density are presented: 2×10^{-6} Å^{-2} (blue), 4.5×10^{-6} Å^{-2} (red) and 9×10^{-6} Å^{-2} (black).
As we can see amplitude of the fringes increases as the scattering length density of the film increases.

2.7) Influence of the roughness of the deposited material on the shape of the reflectivity profile

The work of Kiessing, Parrat [28], Yoneda [29], Nevot and Croce [16-18, 30] and others [15, 19, 24, 25, 31] demonstrated that the shape of the reflectivity profile is sensitive to three variables: In the last section we demonstrated the influence of the thickness and the scattering length density of the deposited material on the shape of the reflectivity profile. In this section we will discuss the effect of the roughness parameter

Up to now we have considered surfaces and interfaces to be infinitely sharp. In reality any interface is jagged, and the degree of roughness of an interface depends on the resolution of the instrument used [32, 33]. In the earliest work on the reflection of X-ray and neutron from interfaces, it was realised that it is possible to account for interface roughness with the methods known from the scattering of other kinds of radiation [26]. However, only after the work of Nevot and Croce [16, 17, 30] in the 1970s could the effect of surface roughness be described quantitatively.

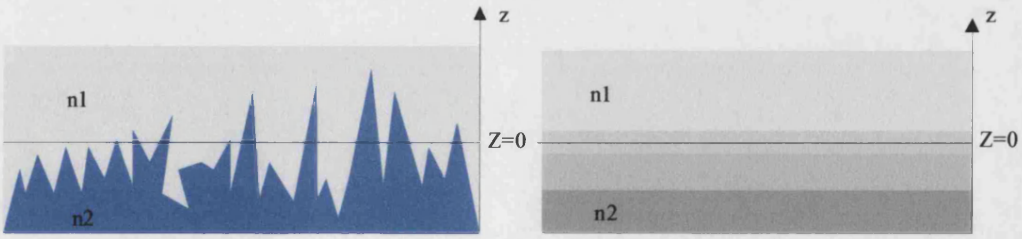

Figure 2.12. This figure illustrates the possibility of existence of two kinds of roughness. The first on (figure in left hand side) corresponds to the roughness due to the geometrical inhomogeneities of the interface. The second one (figure in the right hand side) corresponds to the existence of a gradient in the refractive index normal to the surface.

Interface roughness can be divided into two categories: Roughness and inter-diffusion (figure 2.12). Specular reflectivity cannot distinguish between roughness and inter-diffusion if the size of the imperfection of the surface is smaller than the coherence length of the X-ray [2, 26]. Interface roughness reduces the specular reflectivity and give rise to diffuses scattering [2, 19, 20].

A characteristic measure of a rough interface is its root-mean-square (r.m.s) roughness, σ [34]. However, for a full characterisation, the lateral behaviour of the interface must also be known [20, 34]. There are two factors which take into account the effect of the roughness [20]. The first one is called the static Debye Waller factor [34] (D.W) which is applied at large value of Q_z, and is equal to

$$e^{-Q_z^2\sigma^2}$$

Equation 2.87

The second one is due to Nevot and Croce [16, 17] (N.C) which is applied in the vicinity of the total reflection region [20] and is equal to

$$e^{-Q_{z1}Q_{z2}\sigma^2}$$

Equation 2.88

To take into account the roughness of the interface in to the reflectivity profile, the reflectivity profile from a perfectly sharp interface is multiplied by one of these factors depending on the lateral dimension of the roughness [20].

In the case of a multilayer, where each interface has its own roughness, Abeles defined a characteristic matrix per layer in term of Fresnel reflectance and phase factor [24].

$$C_j = \begin{bmatrix} e^{i\beta_{j-1}} & r_j e^{i\beta_{j-1}} \\ r_j e^{-i\beta_{j-1}} & e^{-i\beta_{j-1}} \end{bmatrix}$$

Equation 2.89

Where r_j is the reflectance from the j^{th} interface.

$$r_j = \frac{Q_{z,j} - Q_{z,j+1}}{Q_{z,j} + Q_{z,j+1}} e^{-\frac{Q_{z,j}Q_{z,j+1}}{2}\sigma_j^2}$$

Equation 2.90

He introduced for each layer the roughness parameter σ_j [24]. For a system of N layer the characteristic matrix is equal to the product of the C_j matrix of each layer.

$$\begin{bmatrix} M_{11} & M_{12} \\ M_{21} & M_{22} \end{bmatrix} = \prod_{j=1}^{N+1} C_j$$

Equation 2.91

Then the reflection coefficient is equal to [24]

$$R = \frac{M_{21} M_{21}^*}{M_{11} M_{11}^*}$$

Equation 2.92

Where M^*_{ij} is the complex conjugate of the element M_{ij} of the characteristic matrix. The advantage of this technique is the possibility to simulate the reflectivity profile from a multilayer interface. Figure 2.13 represents the reflection profile from a silicon surface with a Gaussian mean square deviation of 15 Å. As we can see, the simulated reflectivity profile drops more steeply at higher transfer moment than the Fresnel profile.

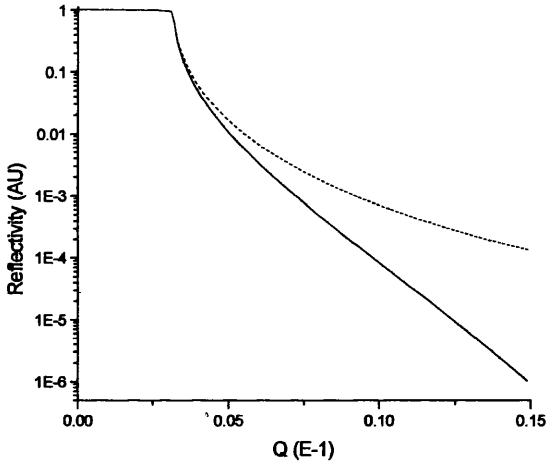

Figure 2.13. Comparison between the calculated reflectivity profile from a silicon substrate with 15 Å roughness (the black curve) and the reflectivity profile from a ideally smooth silicon substrate (dashed line). As we can notice at high Q the reflectivity profile from the rough surface drops more quickly than the flat surface.

In figure 2.14 a thin layer of 30 Å of scattering length density of 9×10^{-6} Å^{-2} has been superimposed on the flat, smooth silicon substrate. The interference pattern (fringes) arising from the reflection at the interface is clearly seen. Two cases are considered: the first case is dealing with the roughness of the interface (figure 2.14.b) the second case is dealing with the roughness of the surface (figure 2.14.a). It is interesting to

note that the roughness of interfaces damps the amplitude of the interface fringes while roughness of the surface lowers the intensity at high transfer moment.

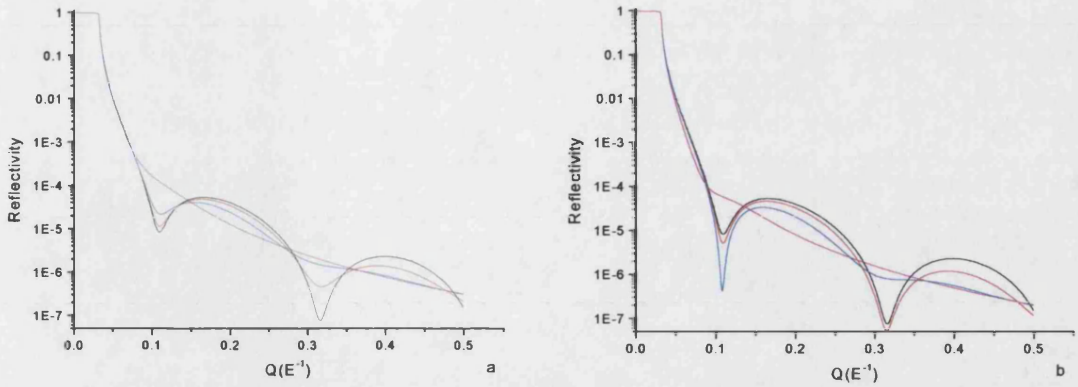

Figure 2.14. Illustrates the effect of the roughness on the reflectivity profile. **a)** As the roughness at the surface increases: σ=0 Å (black), σ= 3 Å (red), σ= 6 Å (blue) and σ= 18 Å (magenta).the intensity of the fringes decreases. **b)** As the roughness at the interface increases: σ=0 Å (black), σ= 3 Å (red), σ= 6 Å (blue) and σ= 18 Å (magenta) it becomes more difficult to distinguish the fringes.

2.8) Theoretical and Experimental limitations

In the last section we discussed the possibility of using X-ray and neutron specular reflection from interfaces to extract some structural information about the deposited material on top of a substrate. The discussed possibilities present some theoretical and experimental limitations. This section gives a summery of these limitations and at which extend one must be aware of their existence.

2.8.1) Theoretical limitation: The "Phase problem"

As, we discussed in section 2.6) different analysis techniques can be used to determine the scattering density profile *via.* specular reflection of X-rays or neutrons. Two techniques have been presented. One of them, Dynamical theory is exact and is very well suited to model the reflection from samples with complex layer structure and interfaces. The other one, kinematics approximation, is an approximate technique and is well suited to extract some physical idea about the structure of the studied system.

In both cases for the determination of the scattering density profile one commonly makes use of simulations to achieve a fit of the measured reflectivity as a function of incident transfer moment. In this type of analysis the reflection phase is not used a

separate input (even if few attempts have been made to overcome this problem [35], the experimental set-up is complicated and time consuming). Therefore, the procedure will generally lead to ambiguous results, since only knowledge of reflectivity in conjunction with phase guarantee a unique determination of the density profile [1, 26]. The non-uniqueness of the used model to fit reflectivity data is referred to as "phase problem" [36]. This means that it is very important to have as much supporting information about the structure as possible by using other experimental techniques, in order to fix few parameters in the model.

The model-dependent character of the reflectivity analysis is the most important feature that one must have in mind before beginning any analysis of the reflectivity profile. Then the question how unique is the model that one is using to describe the data must be raised. This is the most important question which relies on several factors [26]. Among these are the design of a specific experiment, the quality of the sample being studied, the spectrometer resolution, the quality of the measured reflectivity profile and the goodness of the fit. All of these must be considered in determining the credibility of a given model for the description of observed data.

2.8.2) Experimental limitations

The parameters that enter into the observed reflectivity profile are the magnitudes of the scattering densities with respect of each others [26] and with respect to the substrates. In the case of neutron radiation on can adjust the contrast between the film and the substrate (or between the film and the sub phase) by changing the degree of the deuteration of the solution or the material from which the film is made [3]. In addition the total thickness and the roughness at the air / sample and sample / substrate interfaces must be considered. Obviously, if the specimen is made very thick, then as far as the reflectivity experiment is concerned the specimen is infinitely thick. Yet by doing this two parameters have been eliminated: the thickness and sample / substrate and interfacial roughness. Therefore, to detect the structure of a material by reflectivity techniques the thickness of the film must be typically between 10 Å to 2000 Å.

The effect of the roughness is more complex [2, 25]. Two factors must be considered: the amplitude of the roughness and the lateral dimension of the roughness. If the amplitude of the latter is very high (> 150 Å [26]) the reflectivity profile is dominated

by the effect of the roughness and the existing techniques cannot model the sample [26]. The amplitude of the effect of the lateral dimension of the roughness depends on the resolution of the spectrometer and the in-plane coherence length (area) of the incident beam [26] (figure 2.15).

The notion of the coherence length will be discussed in more detail in chapter V.

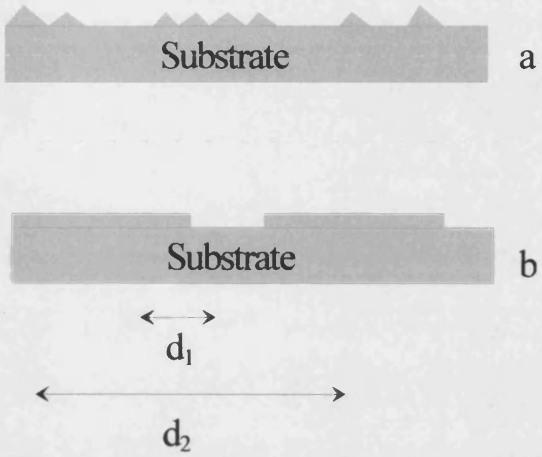

Figure 2.15. Schematic diagrams of a rough surface of a sample.d_1 and d_2 are arbitrary distance over which the scattering length density is averaged. If the scattering length density is averaged over d_2 the scattering from a and b are similar,. However, if the scattering length density averaged over d_1 the scattering from a and b will be different.

2.9) Conclusion

In this chapter we discuss the important points in the reflection theory for our study. We have shown the possibility of using X-ray and neutron reflection to determine the structure of a thin film normal to the surface on top of a substrate. The parameters that we extract from these techniques are thickness, roughness and scattering density. However, we discussed that the scattering profile determined by the fitting procedure is not unique and is part of a family of profile which can model the data [36]. Finally, we showed that the design of the experimental procedure (choice of substrate, the instrumental resolution...) can be a crucial factor in the goodness of a chosen model [26].

REFERENCES:

1 M. Born and E. Wolf, *Principles of Optics, Sixth edition* (Pergamon, 1980).

2 J. Daillant and A. Gibaud, *X-Ray and Neutron Reflectivity: Principles and Applications*, (1999).

3 J. S. Higgins and H. C. Benoit, *Polymers and Neutron Scattering*, New York, (1996).

4 V. Chamard, G. Dolino, G. Lerondel, et al., Physica B **248**, 101 (1998).

5 J. Daillant and O. Belorgy, Journal of Chemical Physics **97**, 5837 (1992).

6 J. D. Shindler, E. A. L. Mol, A. Shalaginov, et al., Physical Review Letters **74**, 722 (1995).

7 A. Zarbakhsh, J. Bowers, and J. R. P. Webster, Meas. Sci. Technol **10**, 738 (1999).

8 C. Fradin, D. Luzet, A. Braslau, et al., Langmuir (Letters) **14**, 7328 (1998).

9 S. J. Roser, R.Felici, and A.Eaglesham, Langmuir **10**, 3853 (1994).

10 M. Tolan, O. H. Seeck, J. Wang, et al., Physica B **283**, 22 (2000).

11 D. K. G. d. Boer, A. J. G. Leenaers, M. W. J. v. d. Wielen, et al., Physica B **248**, 274 (1998).

12 C.-J. Yu, A. G. Richter, A. Datta, et al., Physica B **283**, 27 (2000).

13 S. J. Roser, H. M. Patel, M. R. Lovell, et al., Chem. Commun, 829 (1998).

14 W. R. Birch, M. A. Knewtson, S. Garoff, et al., Langmuir **11**, 48 (1995).

15 R. K. Thomas and J. Penfold, Current Opinion in colloid & interface science **1**, 23 (1996).

16 P. Croce, L. Nevot, and B. Pardo, C. R. Acad. Sc. Paris **Serie B**, 855 (1972).

17 P. Croce, L. Nevot, and B. Pardo, C. R. Acad. Sc. Paris **Serie B**, 803 (1972).

18 L. Nevot and P.Croce, Revue. Phys. Appl **15**, 761 (1980).

19 S. K. Sinha, E. B. Sirota, S. Garoff, et al., Physical Review B **38**, 2297 (1988).

20 D. K. G. d. Boer, Physical Review B **49**, 5817 (1993).

21 J. Daillant, K. Quinn, C. Gourier, et al., J. Chem. Soc., Faraday Trans. **92**, 505 (1996).

22 J. D. Jackson, *Classical Electrodynamics*, New York, (1975).

23 L. Landau and E. Lifchitz, *Physique statistique* (Edition Mir, 1994).

24 J. Penfold and R. K. Thomas, J.Phys: Condens.Matter **2**, 1369 (1990).

25 D. K. G. d. Boer, A. J. G. Leenaers, and W. W. v. d. Hoogenhof, X-Ray Spectrometry **24**, 91 (1995).

26 T. P. Russell, Materials Science Reports **5**, 171 (1990).

27 A. Ishimaru, *Electromagnetic Wave propagation, radiation and scattering* (Prentice-Hall inc, 1991).

28 L. G. Parratt, Physical Review **95**, 359 (1954).

29 Y. Yoneda, Physical Review **131**, 2010 (1963).

30 P. Croce and L. Nevot, Revue de Physique Appliquee **11**, 113 (1976).

31 J. Daillant and O. Belorgey, J. Chem. Phys. **97**, 5824 (1992).

32 M. Tolan and S. K. Sinha, Physica B **248**, 399 (1998).

33 S. K. Sinha, M. Tolan, and A. Gibaud, Physical Review B **57**, 2740 (1998).

34 P. Beckmann and A. Spizzichino, *The Scattering of electromagnetic waves from Rough surfaces* (Pergamon, London, 1963).

35 C. F. Majkrzak, N. F. Berk, S. Krueger, et al., Biophysical Journal **79**, 3330 (2000).

36 G. Reiss and R. Lipperheide, Physical Review B **53**, 8157 (1996).

Chapter III

Introduction to electrochemistry

"La question ne se pose pas, il y a trop de vent."
Boris Vian

3.1) Introduction

The first electrochemical experiments were performed by the Italian physicist Luigi Galvani (1737 – 1798), who investigated the nature and effect of what he conceived to be electricity in animal tissues. His most famous studies involved electrified frog legs. Since, then developments in electrochemical science have created new domains of application of electrochemistry. As defined by Schmickler [1]: electrochemistry studies processes and phenomena at the interface between an electrical conductor (the electrode) and an ionic conductor (the electrolyte) or at the interface between two electrolytes.

As we discussed in the first chapter, electrochemical techniques can be used to deposit or synthesise organic [2-5] or inorganic [6-8] material on the surface of an electrode. These materials can be characterised by reflectivity techniques. However, the complexity in the structure of commonly used electrodes and the difficulties of cleaning their surfaces can make these experiments difficult and time consuming.

We have proposed that one way to overcome this problem is to use highly doped silicon as an electrode. However, doped silicon belongs to the family of semiconductor materials therefore its electrochemical behaviour is different, to some extent, from that of the classical metallic electrode [9].

In this chapter we introduce some rudimentary aspect of electrochemistry from a physical perspective. Then we discuss the basic concepts of semiconductor electrochemistry. In the last part we focus our attention on the properties of the silicon electrode.

3.2) Basic electrochemistry

In this section we show how the interface between the electrode and the electrolyte can be described by electric double layer model, then we will describe the cyclic voltammetry and the electrocrystalisation

3.2.1) Electrode / Electrolyte interface

At any interface, particularly at a solid / liquid interface, a charged plane or space charged layer is formed. This leads to the formation of an electrical double layer due to the motion of the charge carriers. The earliest work on the double layer is due to Helmholtz. He considered that a layer of positive charged ions were tightly

bound to the negatively charged electrode surface. The centres of these ions were postulated to lie on a single "Helmholtz" plane at a distance z_H from the electrode surface. This is the Helmholtz double layer, positioned between the surface and outer Helmholtz plane (OHP) (Figure 3.1). The resulting potential is identical to that within a capacitor, and is a linear interpolation between the bulk and surface potentials. The Helmhlotz layer is assumed to be extremely thin with a width of about 3 Å [10].
However, the model presented by Helmholtz is independent of applied potential and is in conflict with experimental observations.

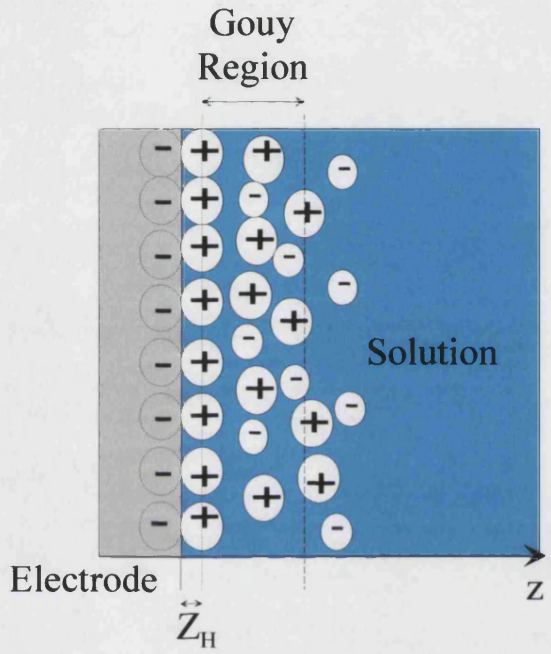

Figure 3.1 Schematic representation of the double layer at the solid / liquid interface.

Gouy in 1910 and Chapman in 1913 proposed that none of the ions were tightly bound to the surface. Each ion is sensitive to the electrical potential formed by other ions but not constrained to a tight double layer. In this case the position of the ions are not predetermined, but are the results of a statistical equilibrium with respect to the mean potential across the interface. This consideration is an improvement over the Helmholtz model but does not take into account the finite size of ions. Stern realised this in 1924. He considered that the plane of closest approach corresponds to the Helmholtz layer and called this: distance of closest approach Z_{OHP} (OHP stands for "Outer Helmholtz plane") and applied the Gouy-Chapman description for distances larger than Z_{OHP}. The Gouy layer is important only for dilute solution, in the case of

concentrated solutions the Gouy layer is extremely thin so that it can be considered as a part of the OHP.

3.2.2) Commonly used techniques

The most common tool to study electrode processes is potential sweep methods. The potential sweep method consists of the application of a continuous time-varying potential to the working electrode. This results in the oxidation or reduction of the electro-active species according to the current and capcitative current due to double layer charging [10]. Its principal use has been to diagnose the mechanism of electrochemical reactions for identification of species present in the solution and for semi-quantitative analysis of reaction rate. In cyclic voltametry (CV) the potential difference between the working electrode and the reference electrode is scanned between preset limits, as depicted in figure 3.4.a.

An electron transfer reaction at an electrolyte / electrode interface often involves several processes. The overall reaction rate will be determined by the slowest transport process of the reactant species from the bulk to the electrode surface. Therefore mass transport effects are important for a successful analysis of an electrochemical experiment.

In this section we first discuss the general mass transport phenomena and we solve explicitly the diffusion equation. Then we will introduce some ideas about cyclic voltametry and electrocrystalisation.

3.2.2.1) Transport of ions

The current of the species i in the solution is proportional to the electrochemical potential gradient [11] (Smolochovsky equation, Langevin equation [11]).

$$\vec{j}_i(r) = -\frac{C_i D_i}{kT}\vec{\nabla}\mu_i^{elec} + c_i\vec{v}(r)$$

Equation 3.1

Where $\vec{v}(r)$ is the velocity of the solution and D_i is the diffusion coefficient of the species i, in the solution. By using the expression of the electrochemical potential in the case of a dilute solution we find the Nernst-Planck equation [10]:

$$\vec{j}_i(r) = -D_i\vec{\nabla}c_i(r) - \frac{D_i c_i(r)}{kT}\nabla\phi(r) + c_i(r)\vec{v}(r)$$

Equation 3.2

By using the continuity equation [11]

$$\frac{\partial c_i(r,t)}{\partial t} + \vec{\nabla} j_i(r,t) = 0$$

Equation 3.3

We can express the variation of the concentration as

$$\frac{\partial c_i(r,t)}{\partial t} = D_i \nabla^2 c_i(r,t) + \frac{D_i c_i(r,t) q_i}{kt} \nabla^2 \phi(r,t) - \nabla(c_i(r,t) v_i(r,t))$$

Equation 3.4

The first term on the right hand side corresponds to the diffusion of species i in the solution [11]. The second term represents the electromigration effect [10] and the third term represents the hydrodynamic effects and is called conventionally the convection effect [10].

In any electrochemical experiment it is important to determine which part of the measured current is derived from diffusion as opposed to electromigration. When both effects are present the analysis become difficult. However, electrochemical experiments are generally carried out with large amount of supporting electrolyte relative to the amount of active species. The supporting electrolyte does not take part in the reaction at the electrode, but carries the majority of the current through the solution [10]. The electrolyte serves to screen the ions, making the interaction between them weak; therefore the approximation of an ideal solution becomes more realistic. Hence, the reactant ions arrive mostly via diffusion, and electromigration effects can be neglected [10]. Hydrodynamic transport should be considered when the solution is stirred or the electrode rotated [10]. In this work we will neglect the effect of electromigration because all solutions used have a high concentration of supporting electrolyte and also the electrodes used are planar and fixed therefore we neglect the effects due to convection and the geometry of the electrode [10].

All these considerations simplify equation 3.4 to the diffusion equation. The electrode surface is considered as a perfect sink for the species i (*i.e.* $c_i(z = 0^+, t > 0) = 0$). Furthermore; the solution container is assumed to be semi-infinite therefore, far from the electrode surface the bulk solution concentration will be maintained $c_i(z \to \infty, t) = c_\infty$ (Figure 3.2). We must therefore solve the linear diffusion equation.

$$\frac{\partial c_i(z,t)}{\partial t} = -D_i \frac{\partial^2 c_i(z,t)}{\partial z^2}$$

Equation 3.5

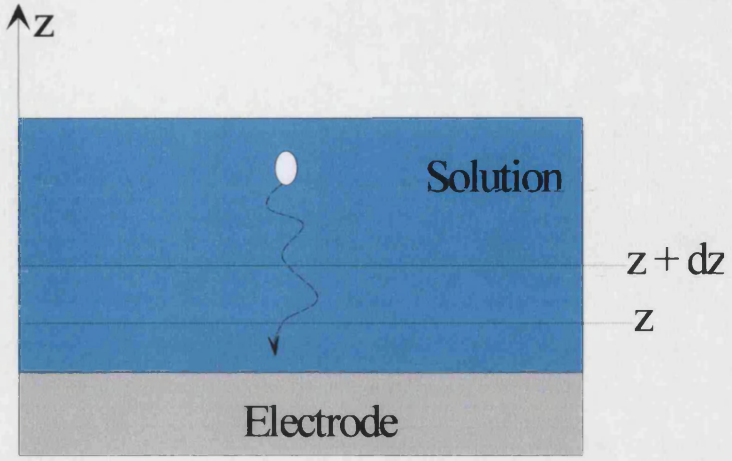

Figure 3.2. Diffusion to a large planar surface

The standard method to solve equation 3.14 is to use the Laplace transform of this equation [10] and take into account the initial conditions (I.C) defined:

$$sC_i(z,s) - c_\infty = D_i \frac{\partial^2 C_i(z,s)}{\partial z^2}$$

Equation 3.6

Where $C_i(z,s)$ is the Laplace transform of the function $c_i(z,t)$, and s is the reciprocal variable in the Laplace transform of the variable t. Equation 3.6 is an ordinary second order differential equation and has as its solution:

$$C_i(z,s) = A(s)e^{\left(\frac{s}{D_i}\right)^{\frac{1}{2}}z} + B(s)e^{-\left(\frac{s}{D_i}\right)^{\frac{1}{2}}z} + \frac{c_\infty}{s}$$

Equation 3.7

Applying the initial conditions to equation 3.7 we find that A(s) = 0 and $B(s) = -\frac{c_\infty}{s}$.

Therefore the solution of the transformed equation is:

$$C_i(z,s) = \frac{c_\infty}{s}\left(1 - e^{-\left(\frac{s}{D_i}\right)^{\frac{1}{2}}z}\right)$$

Equation 3.8

Taking the inverse Laplace transform yields the concentration profile.

$$c_i(z,t) = c_\infty erf\left(\left(\frac{1}{tD_i}\right)^{\frac{1}{2}}\frac{z}{2}\right)$$

Equation 3.9

Where erf (x) is the error function. Figure 3.3 represents the variation of the concentration as a function of time and distance from the electrode surface for $D_i = 10^{-5}$ cm.s^{-1}. The concentration profile begins as a steep distribution, but broadens at later time as the diffusion makes more ions available.

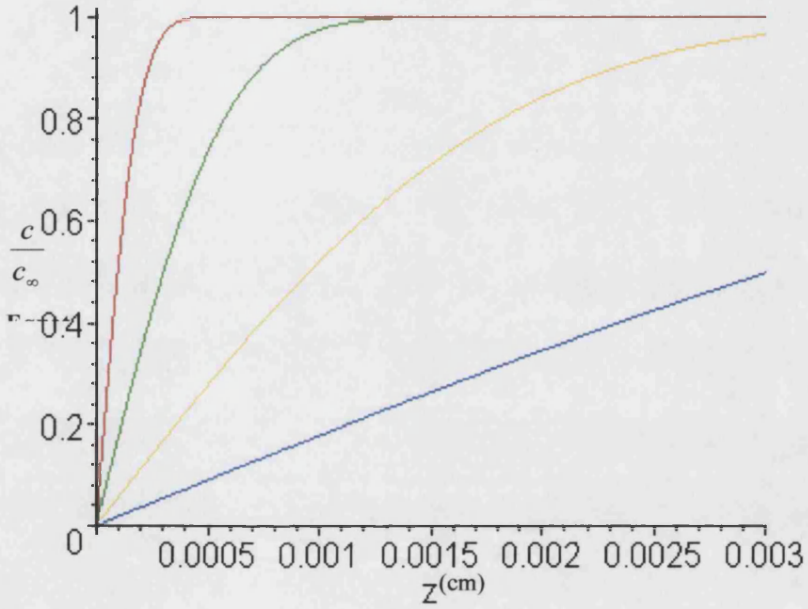

Figure 3.3 Normalised concentration profiles for t = 0.001 s (red curve), t = 0.01 s (green curve), t = 0.1 s (yellow curve), t = 1 s (blue curve).

3.2.2.2) Cyclic voltammetry

As the name suggests, cyclic voltammetry is a measurement of the current while the voltage is being swept (linearly with time). The adjective cyclic refers to the fact that the voltage is swept in both directions.

Consider the oxidation of a species R at the electrode to its oxidative form O, and the adsorption of both species on the electrode.

$$R \rightleftharpoons O + ne^-$$

Equation 3.10

We suppose that the rate of reaction of adsorbed species is much greater than of species in solution, therefore only the adsorbed oxidized and reduced species contribute to the total current. We wish to obtain an expression for the variation of current density, j ($A.cm^{-2}$), as a function of the voltage E, and the sweep rate v. The current density for oxidized species initially adsorbed can be written as:

$$j(t) = nF\frac{dc^O_{surface}}{dt} = -nFv\frac{dc^O_{surface}}{dE}$$

Equation 3.11

Where $c^O_{surface}$ is the surface concentration of adsorbed oxidized species. Assuming the oxido reduction reaction is completely reversible the Nernst equation can be applied. Therefore the ratio between the concentrations of different species present at the surface of the electrode can be linked to the potential E and the standard potential E_0:

$$\frac{c_0(t)}{c_R(t)} = e^{\frac{nF(E-E_0)}{RT}}$$

Equation 3.12

Where c_O and c_R are the concentration of the oxidized and reduced species at the surface of the electrode. Therefore the ratio between the concentrations of adsorbed species is equal to:

$$x = \frac{c^O_{surface}}{c^R_{surface}} = \frac{b_0}{b_R}\frac{c_0(t)}{c_R(t)}$$

Equation 3.13

Where b_O and b_R express the adsorption energy of the oxidized and reduced species. Since we assumed that $c^R_{surface}(t=0)=0$, then $c^R_{surface}(t)+c^O_{surface}(t)=c^O_{surface}(t=0)$ for all t. Then

$$c^O_{surface} = c^O_{surface}(t=0)\frac{x}{1+x}$$

Equation 3.14

And now we taking the derivative:

$$\frac{dc^{O}_{surface}}{dE} = c^{O}_{surface}(t=0)\frac{dx}{dE}\frac{x}{(1+x)^2}$$

Equation 3.15

And by substituting equation 3.15 into equation 3.11 and replacing x we obtain:

$$j = -\frac{n^2F}{RT}vc^{O}_{surface}(t=0)\frac{\frac{b_O}{b_R}e^{\frac{nF(E-E_0)}{RT}}}{\left(1+\frac{b_O}{b_R}e^{\frac{nF(E-E_0)}{RT}}\right)^2}$$

Equation 3.16

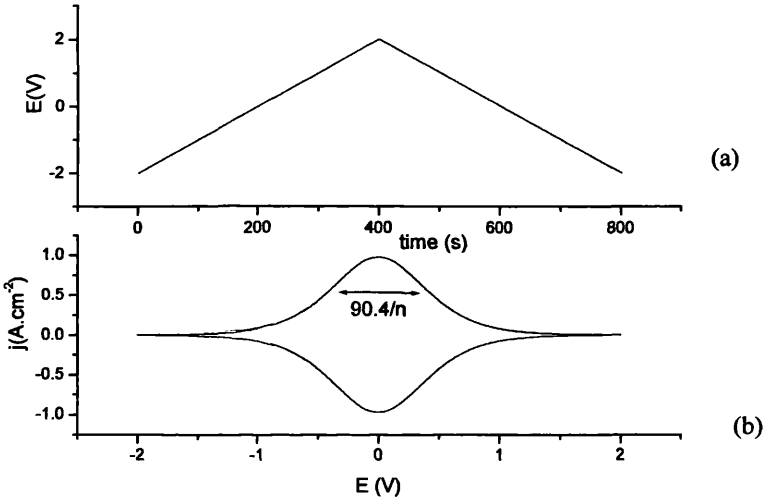

Figure 3.4 (a) This figure represents the applied voltage waveform **(b)** This figure represents the current response for an ideal system where the oxidised species and the reduced species are adsorbed on the electrode surface.

From this formula we calculate the full width of the half-maximum, which is approximately $\frac{3.52RT}{nF}$, or about $\frac{90.4}{n}$ mV at 25°C.

3.2.2.3) Electrocristalisation

Electocrystalisation on foreign substrates has been widely discussed in the literature. A full review can be found in "Instrumental methods in electrochemistry" [12]. The main feature associated in electrocrystalisation, under the potentiostatic

control, is that the current transients exhibit characteristic shapes that depends on the growing centres. The simplest limiting cases are shown in table below.

Type of growth	$i \propto t^0$	$i \propto t^{0.5}$	$i \propto t$	$i \propto t^{3/2}$
2-D instantaneous	$i = \frac{ZF\rho}{M}\pi\theta^2 D$		$i = \frac{2Z\pi FM}{\rho}N_0 hk^2 t$	
2-D progressive			$i = \frac{ZFh\rho}{M}\pi\theta^2 DAt$	
3-D instantaneous		$i = \frac{2F\rho}{M}N_0\pi\theta^3 D^{\frac{3}{2}}t^{\frac{1}{2}}$		
3-D progressive				$i = \frac{ZF\rho}{M}\left(\pi\theta^3 DA^{\frac{3}{2}}\right)\frac{2}{3}t^{\frac{3}{2}}$

Type of growth	$i \propto t^2$	$i \propto t^3$
2-D instantaneous		
2-D progressive	$i = \frac{ZFM\pi h}{\rho}Ak^2 t^2$	
3-D instantaneous	$i = \frac{2ZF\pi M^2}{\rho^2}N_0 k^3 t^2$	
3-D progressive		$i = \frac{2ZF\pi M^2}{3\rho^2}N_0 k^3 t^3$

Table 3.1. Current in the limit t small ($t \to 0$) into isolated nuclei (without overlap). F is the Faraday constant, M is the molecular weight, ρ is the density, N_0 is the number of formed nuclei, h is the height, A and θ are two constants (θ depends on the applied potential), z is the number of exchanged electrons, and D is the diffusion constant.

At large time the current is determined by the overlap of the growing centres [12]. In the case of two dimensional growth the shapes shown in figure 3.5 are observed.

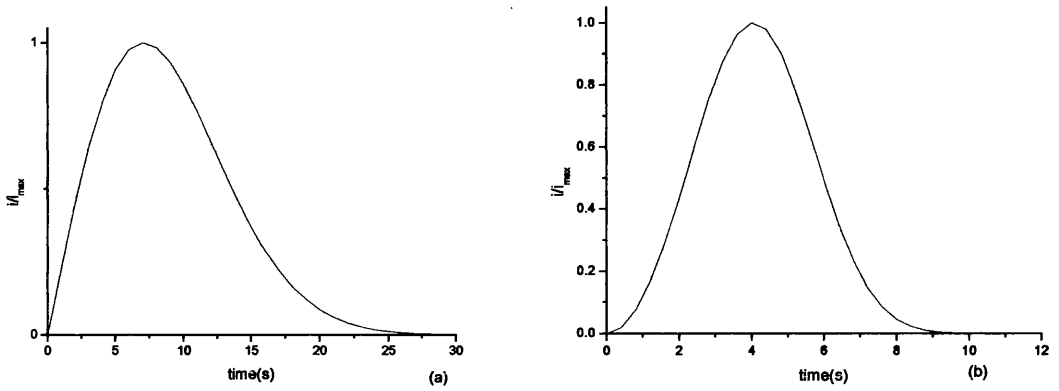

Figure 3.5. Theoretical current line curve for two dimensional growth process with overlapping. (a) instantaneous nucleation (b) progressive nucleation

In the case of three dimensional growth of conducting deposits, under diffusion control process, the current transient exhibits the form shown in figure 3.6.

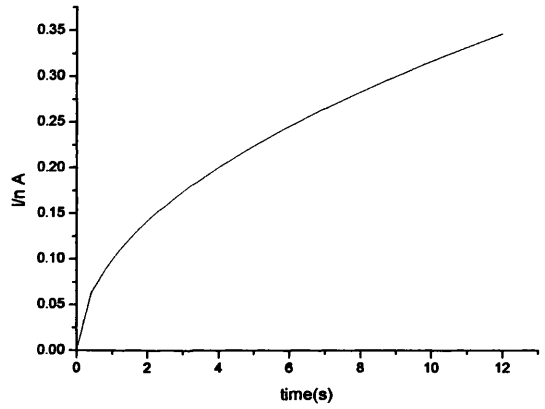

Figure 3.6. current transient for the three dimensional growth of a conductor deposit.

In this work the growth of poly (aniline) was discussed, using the descried method. However, as the growth of poly (aniline) film does not have the same geometry in the direction normal to the electrode surface and in the direction parallel to the electrode surface the structure of the formed film could be described by a self-affin growth process [13]. It is clear that the processes involved in the electrodeposition of the metals are different from the one involve in the electroformation of poly (aniline) film. However, the growth of poly (aniline) film can be described by using the same geometrical arguments that are used to describe the metal deposition process.

3.3) Introduction to the semiconductor-electrolyte interface

3.3.1) Semiconductors

The electronic properties of solids are determined by their band structure. The completely filled or completely empty bands do not contribute to the conductivity [14]. The filling of the available energy levels determines whether a material is a metal or an insulator. In the case of an insulator the current-carrier bands do not overlap (as they do in metals) they are separated by a forbidden region. The width of this forbidden region is called the "band gap", E_g [14]. The lowest energy level bands are called valence bands, and they have the highest occupied state of energy and the band with lowest occupied states is called the conduction band (Figure 3.7).

However, when the temperature is raised there is a nonvanishing probability that

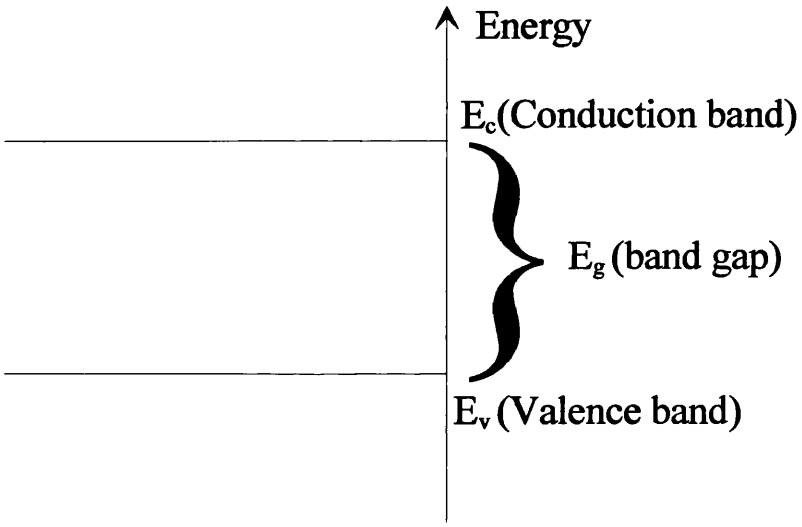

Figure 3.7. The schematic representation of the band structure

some thermally excited electrons transit from the valence band across the energy gap into the conduction bands. Whether such thermal excitation leads to appreciable effects on the conductivity of the material depends on the size of the band gap. Solids that are insulators at absolute zero temperature, but whose energy gap is of such a size that thermal excitation can lead to a observable conductivity at temperatures below the melting point are known as semiconductors [14]. At room temperature the resistivity of these materials (10^{-2} to 10^{9} Ω.cm) is intermediate between the resistivity of insulators (10^{14} to 10^{22} Ω.cm) and metals (10^{-6} Ω.cm).

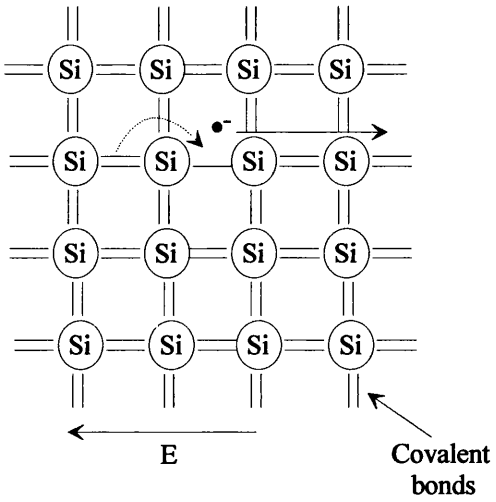

Figure 3.8. Schematic representation of the movement of the electrons and the holes in the silicon created by thermal excitation

The conduction process in a semiconductor can be described by the schematic representation in the figure 3.8. At 0 K all of the covalent bonds are maintained and each atom of silicon has eight electrons on its outer electronic layer. The transfer of an electron from the valence band to the conduction band corresponds to the elimination of a covalent bond under thermal excitation. Therefore the excited electron behaves as a free electron in the crystal and takes an active part in the conduction process. This electron leaves a localised electronic defect in the covalent bond which corresponds to a hole in the valence bond. The hole diffuses in the crystal because an electron in an adjacent bond could be trapped by this hole and creating a new hole in the adjacent covalent bond. Therefore, the hole diffuses in the opposite direction of that of the electron. Under the effect of an electric field the holes diffuse in the same direction as the electric field whereas the electrons diffuse in the opposite direction. Therefore the diffusion of holes in the semiconductor is analogous to the movement of positively charged particles [14]. However, in order to create a measurable conductivity in the semiconductor one must be able to overcome the band gap energy E_g. In the case of silicon E_g is equal to 1.1 eV [15]. In order to induce a significant change in the number of charge carriers in a semiconductor the doping process is used.

3.3.2) n-type and p-type semiconductor

The impurities that contribute to the carrier density of a semiconductor are the elements of the third or fifth column of the periodic table [14]. These impurities replace the atoms of the semiconductor (Figure 3.9).

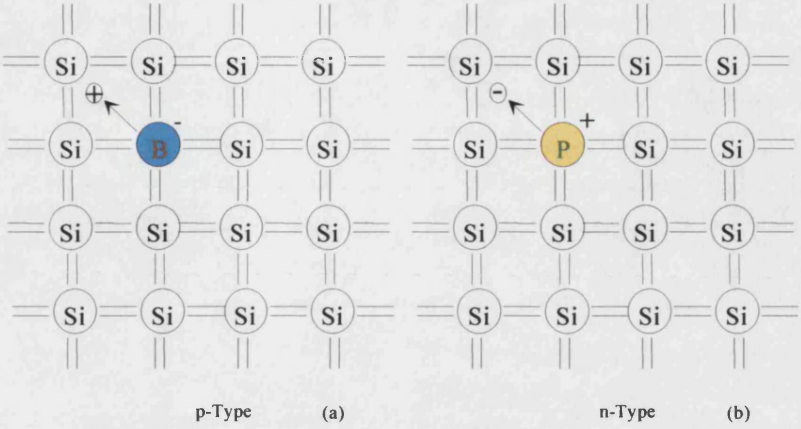

Figure 3.9. (a) Schematic representation of a p-type semiconductor. The boron atom traps one of the electrons of one of the adjacent atoms and creates a hole. **(b)** Schematic representation of a n-type semiconductor. The Phosphorous atom supplies additional electrons to the conduction band

If the impurities are pentavalent (P, As, Sb, Bi), four electrons of the impurity participate in forming covalent bonds with the adjacent silicon atoms. Therefore, one electron is free to participate in the conduction process. As in this case the number of electrons has increased, the semiconductor is called n-type. However, if the impurities are trivalent (B, Al, Ga, In, Tl), one electron from an adjacent silicon atom would be attracted by the impurity to form a covalent bond. Therefore, a hole would be created. Since, in this case the number of holes have increased the semiconductor is said to be of p-type.

In metals, the extent to which the bands are filled is determined by the Fermi Energy, E_f [14]. The Fermi level can be defined as the energy below which all the states are occupied and above which all the states are empty at absolute zero temperature [14]. In the case of a nondoped semiconductor (intrinsic semiconductor), for an electron to travel from the top of valence band to the bottom of conduction band an energy equal to the width of the band gap, E_g, is necessary. This inspires that an energy equal to $E_g/2$ is necessary to create an electron in the conduction band and an energy equal to $E_g/2$ is necessary to create a hole in the valence bond. Therefore, the reference energy for both valence band and conduction band will be the middle of the band gap. Hence, in the case of an intrinsic semiconductor the Fermi level lays half way between bands

[14]. Doping has the effect of moving the Fermi level away from its ideal mid-gap position (Figure 3.10).

In a n-type semiconductor the Fermi level is closer to the edge of the conduction band and in the case of a p-type silicon it is closer to the edge of the valence band [14].

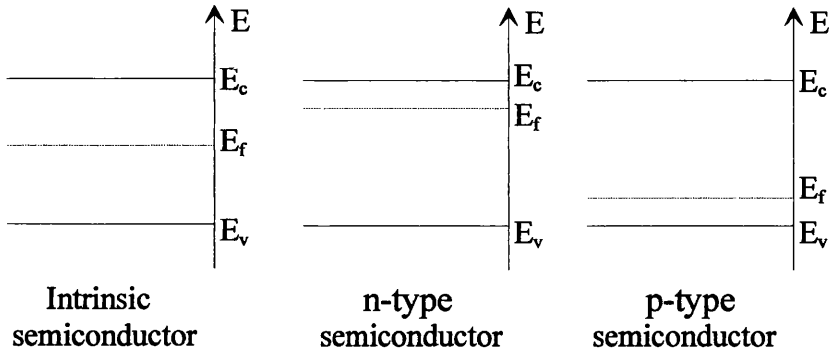

Figure 3.10. Schematic band diagram for the different type of semiconductor

3.3.4) Semiconductor / electrolyte junction

When a junction between a semiconductor and an electrolyte solution is made, thermodynamic equilibrium is established when the electrochemical potential of the species that can be exchanged between the two phases (semiconductor and the electrolyte) are equal. In most cases electrons are the only species that can be exchanged. Therefore, charge flows across the interface until the Fermi energy in the semiconductor (considered as the chemical potential of the electrons in the semiconductor [1]) is equal to the chemical potential of the electrons in the solution [9]. The charge build up on the both sides of the interface leads to a potential drop across the interface, leaving a Space Charge Region (SCR) [1] (figure 3.11). The variation of the potential in the interface region causes a bending of the bands. The space charge density may change due to several processes: (i) interaction of the immobile charged impurities (or immobile trapped carriers near the surface) with the solution and hence alteration of the charge in the surface states [1] (ii) injection and extraction of electrons from the ions in the solution with an appropriate energy level, (iii) imposing an external potential across the interface.

In the latter case the position of the Fermi energy relative to the band edge is not the same as the one in bulk. However, as the position of the Fermi level is imposed by the bulk (equilibrium) therefore it must be the bands themselves which are different at the

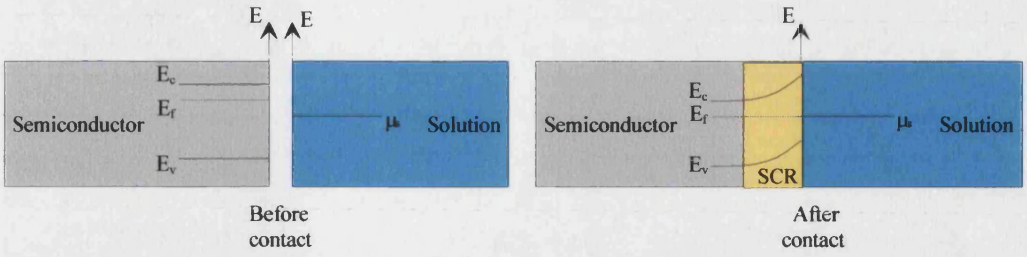

Figure 3.11. Schematic representation of the changes in the position of the energy bands and the formation of the space charge region.

surface. Figure 3.12 shows three different cases of band bending for an n-type semiconductor.

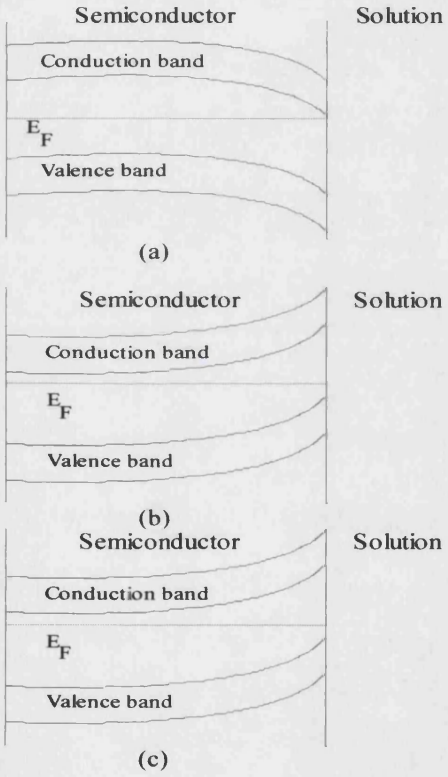

Figure 3.12. Band bending at the interface between an n-type semiconductor and an electrolyte solution.**(a)** Enrichment layer, **(b)** depletion layer, **(c)** inversion layer.

If the value of the potential (ϕ_s) at the surface is positive, the majorities carriers are injected into the surface from the semiconductor, therefore the bands bend downward and the concentration of electrons in the conduction band is enhanced, this is called an

enrichment layer. If $\phi_s<0$ the, the majorities carriers are extracted from the valence band (hole injection). Therefore, at the surface of the electrode there is an important concentration of minority carriers (holes in the case of n-type). In this case the energy bands bend upward and the concentration of electrons at the surface is reduced, this is called depletion layer. If the concentration of the holes exceeds that of the electron this is referred to as an inversion layer.

There is a fundamental difference between electron transfer reactions on metals and on semiconductors. As we have seen, the potential drop in the case of the semiconductor-solution junction occurs in the semiconductor, so the changes in electrode potential do not influence the activation energy for electron transfer. However, the relative position of the Fermi level in the semiconductor is changed [1]. Figure 3.13 shows the Gerischer's diagram [1].

As we can notice the Fermi energy level is located in the band gap. Electron

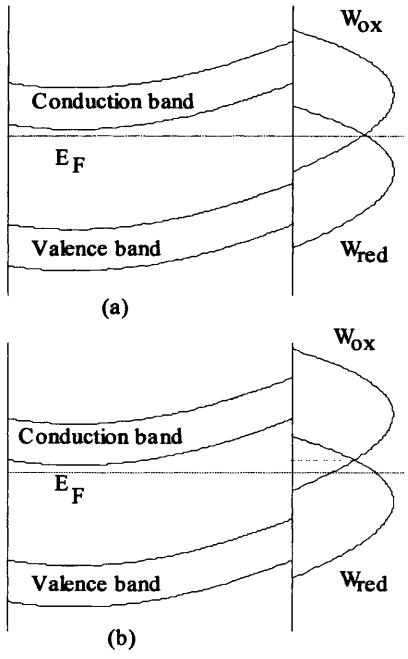

Figure 3.13 Gerischer diagram for redox reaction at an n-type semiconductor.

exchanges with redox species can involve either the conduction or valence band or both. The overlap between the energy bands and the redox states determines the contribution of the two bands to the current [1]. Generally the major part of the current comes from the band that is closer to the Fermi level of the redox system.

3.3.5) Photoexcitation of the electrode

If light of frequency ν, with hν> E_g, (h is the Planck's constant, h = 6.626 × 10^{34} J.s) is incident on a semiconducting electrode, it can excite an electron from the valence into the conduction band, so that an electron-hole pair is created. The electron-hole are separated by a electric field and one of the carriers will migrate toward the bulk of the semiconductor, while the other will drift to the surface, where it can react with a suitable redox partner (Figure 3.14).

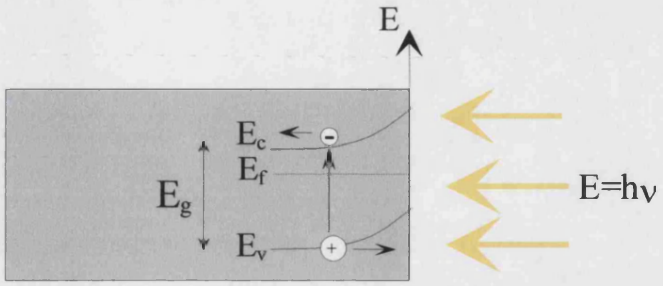

Figure 3.14 Photogeneration for a n-type semiconductor

In the case of the n-type silicon the width of the band gap is 1.1 eV. Therefore the frequency of the incident light must be bigger than 0.26×10^{15} Hz in order to induce the transition of an electron from the valance band to the conduction band. This frequency is in the range of visible light [16] (U.V (4 × 10^{14} Hz) < visible light < I.R (7.5 × 10^{14})) therefore illumination of the sample by white light is enough to induce the electron transition and to create a hole in valence band and an electron in the conduction band. Under depletion conditions the hole diffuses toward the surface of the electrode and the electrons toward the semiconductor bulk. At the surface of the electrode the generated hole can trap either an electron transferred from the solution to the semiconductor (an oxidative reaction) or be recombined with one of the electrons of the conduction band [17].

If the light flux is not too high, the collecting of photogenerated holes at the semiconductor / electrolyte interface gives rise to a current that is directly proportional to the absorbed photon flux. In this case a photocurrent plateau is observed as shown in figure 3.15

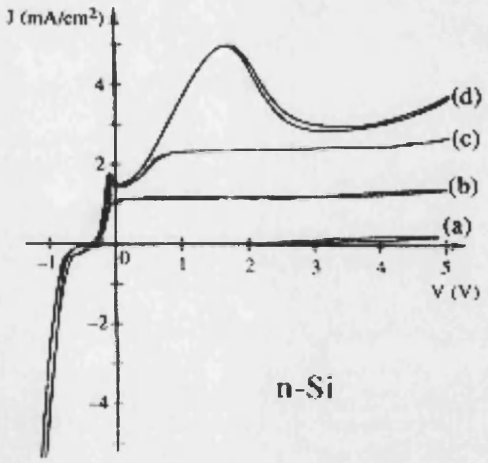

Figure 3.15. Typical current / potential curves at a Si/ fluoride interface.(a) In dark, (b-d) under increasing illumination. Reference is Ag / AgCl in saturated KCl.[18]

However, at high illumination levels the surface concentration of holes may become to large that the n-type semiconductor behaves like a p-type semiconductor. This is the case in the experiments on the photoetching of silicon described in chapter VI and VII. In the next section we will turn our interest to the properties of silicon electrodes.

3.4) Silicon electrode

Silicon is a highly oxidisable material [18]. The stability of silicon electrodes depends dramatically on the type of doping used [19], the direction of the silicon surface electrode [19], the presence of dissolve oxygen in the solution [20, 21], the pH of the solution [19, 21], and finally the concentration of holes at the silicon surface [19, 22, 23]. In this section we discuss first our choice of using the [111] crystallographic direction orientated surface, then we justify the use of n-type rather than p-type silicon electrode. Finally we describe the Brewster angle technique, used to probe the cleanliness of the electrode surface after oxide stripping.

3.4.1) Silicon surface

When the crystal is cleaved, the two electrons forming the covalent bond between two adjacent silicon atoms are shared between the two half-crystals [15]. Therefore, the ideal surface of the crystal exposes hybrid orbital that "dangles" into the vacuum. The [111] surface contains one dangling bond per surface unit cell. The

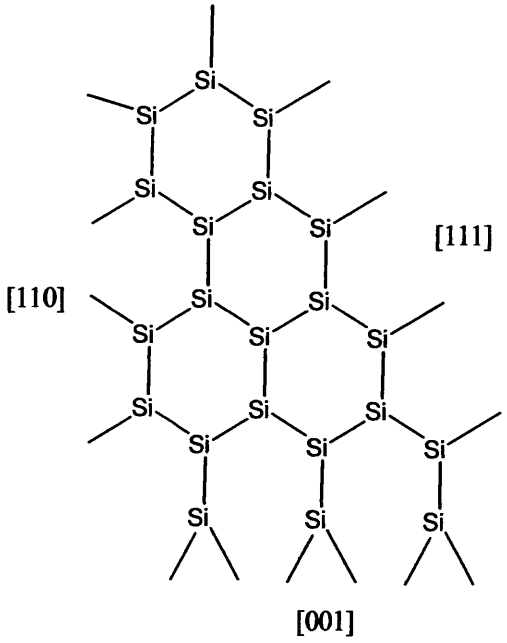

Figure 3.16. The schematic planar representation of the different orientations of the silicon surface

two atoms per cell of [110] each dangle a single bond into the vacuum, whereas the [100] surface cell possesses two dangling bonds attached to a single atom (Figure 3.16).

Table 3.2 shows the densities of the dangling bonds per crystal surface. The density of dangling bond for the [111] surface is the lowest and highest for [100] surface. This observation can be explained by the fact the [111] surface is the natural cleavage plane of silicon [15].

Plane	Atom density (cm^{-2})	Dangling bonds per atom	Dangling bond density (cm^{-2})
[100]	6.78×10^{14}	2	1.36×10^{15}
[110]	9.59×10^{14}	1	0.959×10^{15}
[111]	7.83×10^{14}	1	0.783×10^{15}

Table 3.2. Surface density and number of dangling bonds for ideally terminated, unreconstructed silicon surfaces as a function of crystal orientation in vaccum. (The lattice parameter of silicon is 5.43 Å)[19]

As the structure and the electronic structure of each face is different the properties of each face is different [15, 19].

Yablonovich et al [24] showed that the [111] silicon surface direction has the lowest surface recombination velocity (0.25 $cm.s^{-1}$) after the oxide layer has been removed from the surface of the electrode by a HF etch, leaving no surface dangling bond to act as a recombination centres. Therefore the efficiency of the photoelectrochemical process is increased. Because of the stability of the [111] surface orientation and the possibility of producing hydrogen terminated silicon [111] surface [25]we decided to use and study silicon [111] as an electrode.

3.4.2) Silicon oxide etching and Silicon dissolution in Fluoride solution

Under certain conditions the etch rate of silicon oxide is one or two orders of magnitude faster than for crystalline silicon. In addition etching of the oxide is isotropic whereas etching of hydrogen terminated surface is anisotropic [19]. Typical etch rates for silicon oxide are in the range 1 – 100 $Å.s^{-1}$, depending on HF concentration, pH and temperature [19], and an etch rate of 0.005 $Å.s^{-1}$ has been reported for n-type silicon [111] in 48% HF [19]. The dissolution of SiO_2 by HF can be written as [19]:

$$SiO_2 + 6\,HF \longrightarrow 2\,H^+ + SiF_6^{2-} + 2\,H_2O$$

Equation 3.17

It is important to note that the reaction involves HF molecules and not F^- ions in the solution. HF molecules attack Si-O bonds by inserting themselves between the Si and O atoms. The coulombic attraction leads to the positively charged hydrogen association with the negatively charged oxygen, while the negatively charged fluorine

associates with the positively charged silicon. This reaction releases H_2O and leaves SiF in place on the surface. The substitution of the fluorine terminated surface by the hydrogen terminated surface is thought to be related to the attack of the Si-Si backbonds by HF molecules [19, 26]. Higashi et al [25] demonstrated the production of nearly perfect atomically flat surface by etching the silicon [111] in 40% NH_4F. The hydrogen terminated [111] silicon surface is conductor and atomically flat [25]. This surface is stable to oxidation for several hours in air under ambient condition [25]. Itaya et al [27] demonstrated that even under oxidative conditions (under anodic potential in sulphuric acid and under illumination) the surface of n-type silicon [111] electrode is stable and shows a slow rate of oxidation.

However the fluorine ions have an important place during the direct dissolution of the silicon electrode in HF or NH_4F solution [26]. For the dissolution of silicon in fluoride electrolytes, the first step in the reaction is a hole capture [19, 26]. Therefore, for p-type silicon in the dark the dissolution were occurs when a positive potential is applied to the electrode [19]. Whereas, for the case of p-type silicon, where the holes are the majority carriers, silicon dissolution occurs at much lower applied potentials than for n-type silicon [19]. Therefore when any potential is applied to the silicon electrode the rate of the direct dissolution of p type electrode is higher than the rate of direct dissolution of n-type electrode. As the silicon etching is an anisotropic process [19] the surface of a p-type electrode etched for the same amount of time than a n-type electrode would be rougher.

All these considerations, suggest that in order to use silicon as an electrode it is more convenient to use the n-type silicon [111] as working electrode. In the next section we describe the Brewster angle microscope and we show that by the use of this microscope we can probe the cleanness and the flatness of an etched n-type silicon [111] electrode in the micron scale.

3.4.3) Brewster Angle Microscope images of an etched n-type silicon [111] surface.

In order to study the surface phase diagram of long-chain fatty acid monolayers, Henon and Meunier [28] developed a microscope sensitive to the surface density and the anisotropy of phase domains in monolayers. The microscope is based on the properties of a polarised light reflected from an interface (described in chapter

II). They show that by choosing the angle of incidence to be the Brewster Angle of the bare interface, one can minimise the background intensity and observe the surface structure.

In this section we explain briefly the principles of Brewster Angle Microscopy (BAM) and expand the use of this technique to scan the surface structure of a etched n-type silicon [111] sample.

3.4.3.1) Brewster Angle Microscope (BAM)

The characteristics of scattering at the Brewster angle can be used to build a microscope [28]. The interface is illuminated at the Brewster incidence with a parallel laser beam of P-polarization with a large intensity. The reflected beam is received by a microscope, the axis of which is in the direction of propagation of reflected light (Figure.3.17)

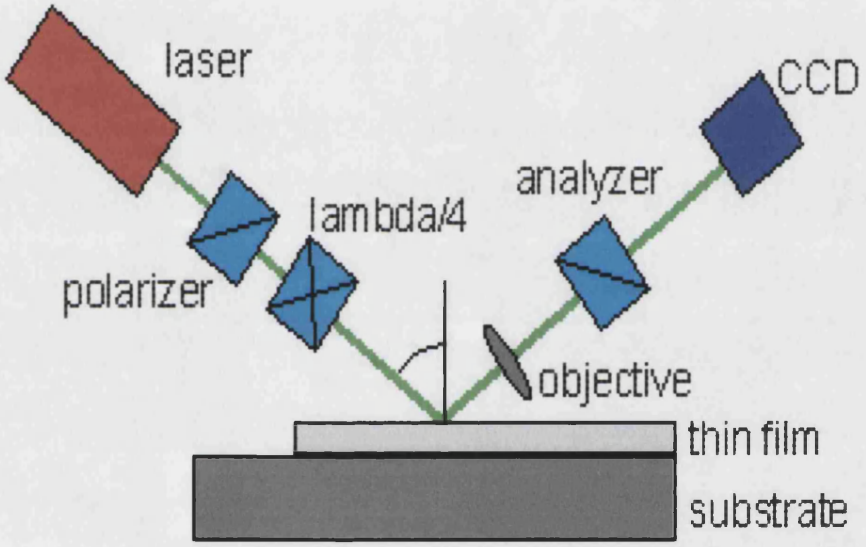

Figure.3.17 schematic representation of the Brewster angle microscope

As the surface is inclined on the axis of the objective the image in the lens is in focus only in a narrow strip. The focal point is scanned across a portion of the surface by a microcomputer and each image of the surface is transferred to the microcomputer using a very sensitive video camera. The lateral resolution of the machine is limited by the objective lens, and in the case of the Bath BAM, is close to1μm, with a total field width in one image of 1000 x 800μm.

An extra sophistication in the Bath BAM is the addition of a quarter wave plate in the path of the incident beam (The machine can then be used at a "pseudo Brewster

Angle" That means we find a particular configuration between the analyser and the polariser in order to find the null point) and an analyser on the path of the reflected beam. By adjusting the position of the quarter wave plate and the analyser we can obtain a high-contrast visualisation of the surface.

The reflected intensity at the Brewster angle depends strongly on three interfacial property [28]: (i) The thickness of the interface, (ii) the roughness of the interface and (iii) the anisotropy of the interface [28].

3.4.3.2) Cleaning of the silicon surface

The must widely used chemical way to clean and passivate silicon surfaces is to grow a thin layer of oxide in the act of cleaning. This is best accomplished using acidic or basic solution mixed with hydrogen peroxide, and is based on the RCA Standard Clean developed By Kern in 1965 [29]. These methods leave a thin layer of silicon oxide on the surface which prevents recontamination of the silicon, such surfaces are hydrophilic in nature, and easily wetted by aqueous solutions. This process involves sequential immersion steps designed to remove organic and inorganic contaminants, respectively:

RCA (1) H_2O / H_2O_2 / NH_4OH (5:1:1) at 75 – 85 °C for 10 - 20 min

RCA (2) H_2O / H_2O_2 / HCl (5:1:1) at 75 – 85 °C for 10 - 20min

The structural characteristics of the cleaned n-type silicon [111] surface were studied by a modified commercial Brewster Angle microscope (NFT technology). As described in the previous section a *P*-polarized light from a 532 nm (>50mW) laser is reflected from the air-silicon interface at the pseudo-Brewster's angle.

To minimise the background reflection from the silicon surface, the angles of the laser beam and the camera are fixed to approximately 50°. The compensator (quarter wave plate) was first adjusted in order to maximise the reflected intensity from the silicon to align the sample. The height of the sample was then adjusted to maximise the intensity on the focal line. Finally, the polariser angle and the analyser angle are iteratively adjusted in order to find the minimum of reflected intensity from the virgin silicon surface at the incident angle chosen.

The silicon sample was cleaned following the sequential immersion RCA (1), RCA (2). and then etched for 10 minutes by a solution of 50 NH_4F (40%): 1% HF [27]. This solution removes the oxide layer and produces a flat hydrogen terminated surface [27]. The sample was removed from the solution, and transferred in to the BAM. The

analyser position was then adjusted at fixed polariser to obtain the maximum of image contrast and the camera focused on the sample. The images are then digitalised, filtered and background subtracted and then processed to obtain the best quality images. Figure 3.17 shows the Brewster angle microscopy images of the surface of a silicon sample before and after the cleaning and the etching procedure.

As can be seen in the images of figure 3.18 after the oxide has been removed the surface of the silicon substrate looks flat and clean.

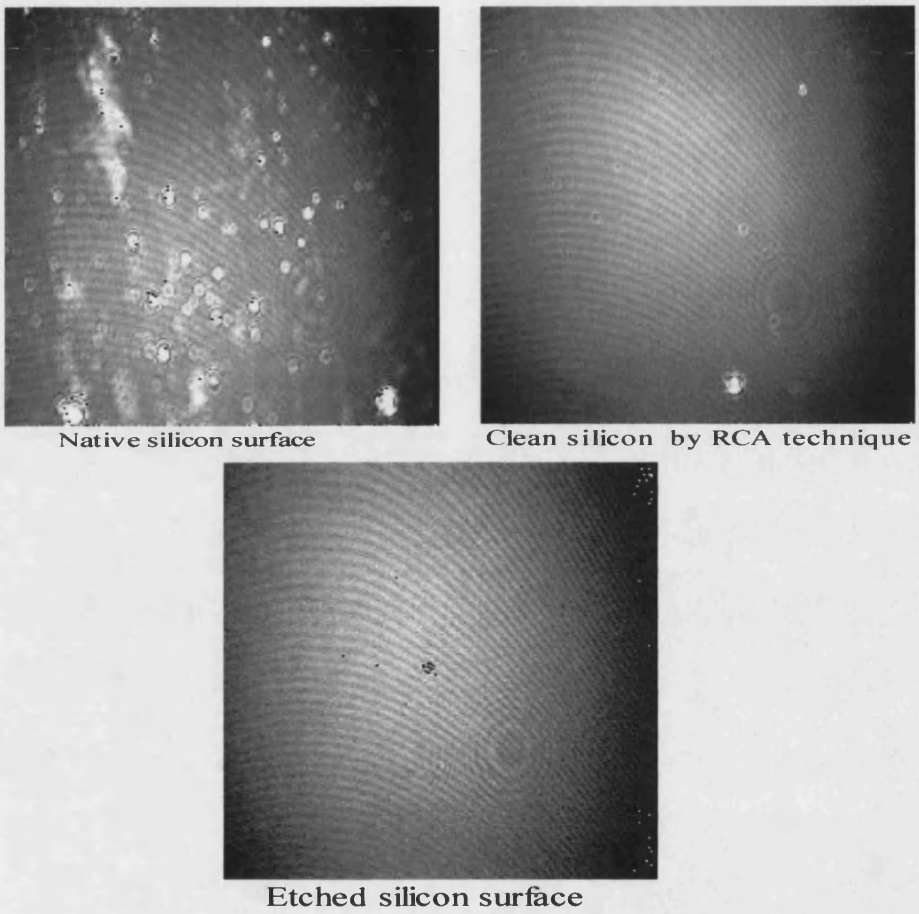

Figure 3.18 BAM images of the silicon surface (with surface orientation [111]) at different stage of cleaning (the scale of each image is 700μm × 700μm)

3.5) Conclusion

In this chapter we introduced the basic concepts and techniques in electrochemistry used in this thesis. We discussed the case of the junction between a semiconductor electrode and the electrolyte. We demonstrate that in the case of a n-type semiconductor electron acceptor (holes) can be generated at the surface of the

electrode by illuminating the surface of the electrode. Then we focused our study on the silicon electrode. As we discussed in the first and second chapter silicon substrate can be a good choice as an electrode in simultaneous reflectivity and electrochemical studies. However, the major problem with the silicon electrode is the presence of the insulating oxide at the surface of the electrode. We demonstrate that this oxide can be removed from the n-type silicon [111] surface and replaced by a smooth monolayer of hydrogen. We describe a simple method to clean and remove the silicon surface by the chemical etching. Finally the discussion in the last part of this chapter suggests the fact that n-type silicon [111] electrode is a stable electrode.

In the next chapter we will use this electrode in order to study the oxidative electrodeposition of a conducting polymer by *in-situ* X-ray reflection and we will show that the simple structure of the electrode and its low scattering length density and its relative transparency to neutrons make this electrode as an ideal electrode for simultaneous electrochemical and reflectivity studies.

References:

1 W. Schmickler, *Interfacial Electrochemistry*, New York, Oxford, 1996).

2 L. Bailey, M. J. Henderson, A. R. Hillman, et al., Physica B **276-278**, 373 (2000).

3 J.-L. Camalet, J.-C. Lacroix, T. D. Nguyen, et al., J. Electroanal. Chem. **485**, 13 (2000).

4 A. R. Hillman, A. Glidle, R. M. Richardson, et al., Journal of American Chemical Society **120**, 12882 (1998).

5 G. Mengoli and M. M. Musiani, Progress in Organic Coatings **24**, 234 (1994).

6 Y. P. Feng, S. K. Sinha, C. A. Melendres, et al., Physica B **221**, 251 (1996).

7 K.-I. Hara and I. Ohdomari, Applied surface Science **144-145**, 476 (1999).

8 K.-i. Hara and I. Ohdomari, Jpn. J. Appl. Phys **37**, L 1333 (1998).

9 L. M. Peter, in *Porous silicon Science and technology*, edited by J.-C. Vial and J. Derrien (Springer-verlag Les Editions de Physique, 1994), Vol. 1.

10 A. J. Bard and L. R. Faulkner, *Electrochemical methods fundamentals and applications* (Wiley, 1980).

11 M. Doi and S. F. Edwards, *The theory of polymer dynamics*, (1986).

12 Southampton Electrochemistry Group, *Instrumental methods in electrochemistry / Southampton Electrochemistry Group* (Horwood, Chichester, 2001).

13 L. Barbabsi and H.E.Stanley, *Fractal Concepts in Surface Growth* (Cambridge university press, Cambridge, 1995).

14 W. N. Ashcroft and N. D. Mermin, *Solid state physics*, 1976).

15 A. Zangwill, *Physics at surfaces*, New York, 1988).

16 M. Born and E. Wolf, *Principles of Optics, Sixth edition* (Pergamon, 1980).

17 L. M. Peter, Chem. Rev **90**, 753 (1990).

18 J.-N. Chazalviel, in *Porous Silicon Science And Technology*, edited by J.-C. Vial and J. Derrien (Les Editions de Physique, Les Ulis, 1995), p. 17.

19 P. C. Searson, in *Advances in electrochemical science and engineering*, edited by H. Gerischer and C. W. Tobias (VCH, Weinheim, 1995), Vol. 4.

20 H. Fukidom and M. Matsumura, Applied surface Science **130 - 132**, 146 (1998).

21 H. Fukidome, in *Department of Chemistry* (Osaka University, Osaka, 2000).

22 M. Matsumura and R. Morrison, J. Electroanal. Chem. **144**, 113 (1983).

23 M. Matsumura and R. Morrison, J. Electroanal. Chem. **147**, 157 (1983).

24 E. Yablonovitch, D.L.Allara, C. C. Chang, et al., Physical review letters **57**, 249 (1986).

25 G. S. Higashi, R.S.Becker, Y. J. Chabal, et al., Applied physics letter **58**, 1656 (1991).

26 P. Allongue, V. Kieling, and H. Gerischer, Electrochimica Acta **40**, 1353 (1995).

27 K. Itaya, R. Sugawara, Y. Morita, et al., Applied Physics letter **60**, 2534 (1992).

28 S. Henon and J. Meunier, Rev. Sci. Instrum **62**, 936 (1991).

29 W. Kern, Journal of the Electrochemical society **137**, 1887 (1990).

Chapter IV

In-situ and *ex-situ* X-ray reflection studies of electrodeposition of poly (aniline) on n-type silicon electrode under illumination

"A fool sees not the same tree that a wise man sees"
William Blake, Proverbs of Hell

In this chapter we aim to study the kinetic and structural changes during the formation of a polymer film. The film has been grown by electrochemical techniques, and changes observed using X-ray reflection. In this kind of investigation the design of the experimental set-up is very important, particularly the choice of the substrate. The substrate must have two important properties, (i) it must be conducting and (ii) its scattering length density must be low enough to allow one to study the scattering from polymer /electrode interface. This study will help us to demonstrate the possibility and advantage of using n-type silicon as an electrode in these kinds of experiments.

Coating electrode surfaces with polymer has been used to stabilize the substrate against corrosion [1-3]. The detail of the structure of the electrodeposited polymer in the direction normal to the surface of the electrode can be studied by electrochemical and reflection techniques [4-10]. The electrochemical approach to characterising the structure of the polymer film is unreliable [4, 9, 11, 12] because of the background current associated with other processes, uncertainties in polymerisation and deposition efficiency of polymer produced in solution. The *ex-situ* reflectivity techniques allows us to extract information about the structure of the polymer film once it has formed but does not give any insight into the kinetic mechanism of the film formation or solvent penetration in the polymer film.

In this chapter we show studies of the electropolymerisation of aniline by the combination of electrochemical techniques and *in-situ* and *ex-situ* X-ray reflectivity.

4.1) Introduction

Poly (aniline) (PANI) is a redox polymer which is an insulator in the electro reduced state and a conductor in its partially oxidized state. It can be prepared either by chemical or electrochemical oxidation of aniline under different conditions [3, 13-15]. The material is amorphous, and is insoluble in most solvents including water [13], but will dissolve in concentrated sulphuric acid [13]. The electrochemistry of poly (aniline) is complex and because the material can have a large number of possible structures, many reaction schemes have been suggested. Many of the proposed mechanisms are based on the formation of radical cation intermediates of aniline [13], and only differ in detail [7, 16-18] (Figure 4.1).

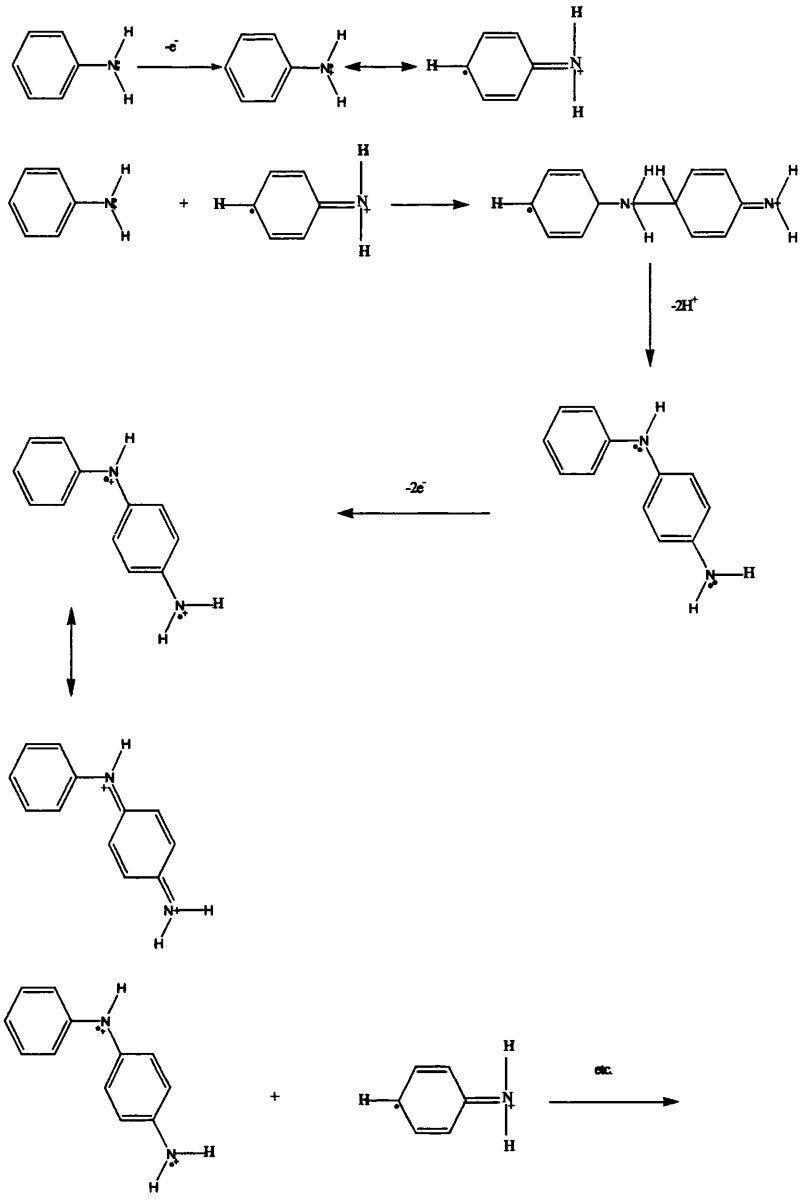

Figure 4.1. General reaction scheme for the polymerisation of aniline [13]

Many of properties of this polymer are pH dependent [17], including the fact that above pH 3 poly (aniline) films do not show any electro activity [13, 17]. One of the properties of this film is its electrochromic behaviour, being yellow below 0V and passing through green blue and black if the potential is taken to +1V [13].

The morphology and structure of poly (aniline) film resulting from the anodic oxidation in acidic media is not very well understood. It is generally accepted that the electrical conductivity of poly (aniline) is limited by structural discontinuities and that its electrochemical performance is dominated by the morphology of the deposited

film [19]. It was concluded at an early stage that the basic structure unit of poly (aniline) was that of the aniline octamer [13]. During the potentiodynamic preparation of poly (aniline) in aqueous sulphuric acid on a platinum substrate, three different growth modes were observed [20]. For an average thickness, <h>, smaller than 100 nm, it is commonly believed that the polymerisation involves a nucleation process similar to that of metals[13, 20], and electrochemically prepared poly (aniline) will form dense and non-fibrillar thin films which do not change significantly the roughness of the substrate [21]. However, for a thicker films (100 < <h> <1000nm) the growing surface becomes less densely packed and more fibrous, the dynamic scaling analysis applied to Surface Force Microscopy (SFM) images indicates the granular film can be described as a self-affine fractal surface [20]. Finally for very thick films (<h> > 1000 nm) it has been found that the surface exhibits patterns, which resemble those formed under diffusion-limited aggregation [20].

The majority of previous experiments have been realised on a platinum electrode, and the thickness of the film is measured by calculating the electrical charge transferred during the electrochemical process. However using this method to determine the thickness one has to assume that the all the charges transferred during the electrodeposition correspond to the formation of a polymer film (current efficiency is assumed to be equal to unity [22]). Therefore, the value of the thickness indicated by the electrochemical technique is not necessarily the real one. In our knowledge, the only technique used in order to characterise the structure of the poly (aniline) film independently of the electrochemical measurements is ellipsometry [5, 23] where a correspondence between the measured charge and the film thickness can be established [23](1 $mC.cm^{-2}$ corresponds to 318 Å). In order to measure directly the thickness of a poly (aniline) film we use a combination of three techniques: specular X-ray reflectivity, Brewster Angle Microscopy (BAM) and the time-variation of the electrical current collected during the electropolymerisation on a silicon electrode.

In this chapter, we will firstly describe the experimental procedure and set-up that we used in carry out this study. Then we will describe the cyclic voltammogram of polymerisation of poly (aniline) on a silicon electrode and we will show how one can follow *in-situ* the thickening of the film by specular x-ray reflectivity. The description of the formation of the potentiostatic formed film is given in the third part. Here we will describe all the processes that participate in the film formation, and again

correlate them to the results obtained by specular x-ray reflection. The fourth section is devoted to discussion of the obtained results.

4.2) Experimental

PANI films were grown on a n-type silicon electrode (phosphorous doped, of resistivity: 1-3 Ω.cm), of [111] crystallographic orientation. First, a 4cm x 5cm silicon substrate was cut from a 10 cm diameter one side etched wafer provided by A.C.M. The back of the substrate was coated with a sputtered thin film of gold in order to form a homogeneous ohmic back contact. The substrate was mounted in a PTFE x-ray cell Figure 4.2.

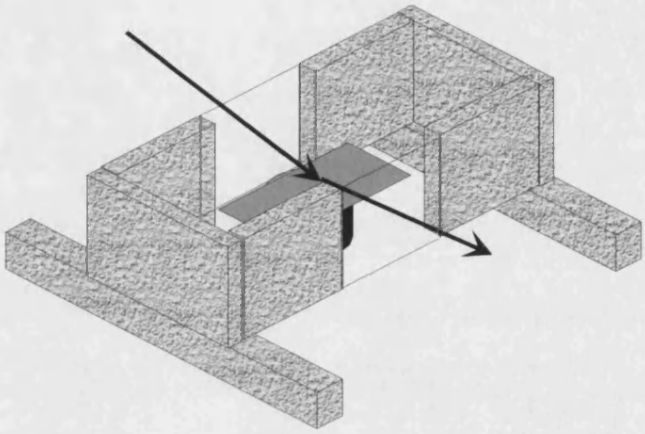

Figure 4.2. The schematic representation of the cell used for the X-ray reflection experiment. The body of the cell is made of PTFE. The incoming X-ray wave reaches the surface of the silicon electrode through a 3mm thick PTFE window. A white light through the electrolyte side illuminates the silicon electrode.

This substrate is then cleaned by several rinses of Millipore water (18 MΩ.cm) and acetone. Following the literature[24], in order to remove the native oxide layer from the substrate surface we used a solution of 1% HF: 50% NH_4F (in volume) and etched the surface for 10 minutes. Finally 150ml of a solution of 0.1M aniline in 0.5M sulphuric acid is added in to the cell.

The electrochemical set-up for PANI film preparation consists of a n-type silicon working electrode, a platinum counter electrode (4cm x 2cm), an Ag/AgCl reference electrode (all the potentials in this work are relative to this reference electrode), and a 110 W lamp (white beam).

PANI films were grown by repetitive triangular potential scanning at a potential sweep rate $V=1mV.s^{-1}$ between the lower switching potential E=-0.2V and the upper

switching potential E=0.9V under illumination. Potentiostatic current transients during the electroformation of PANI were recorded at E=0.9 V under illumination.

The X-ray reflection experiment was carried out with a home made X-ray reflectometer with energy sensitive detection at the University of Bath. The machine is mechanically very simple, with two arms pivoting about a central drive shaft, and the X-ray optical path defined by Huber 50 μm variable slits mounted on the arms. The source is a 2 kW tungsten tube, driven by a Phillips X-ray generator. X-ray detection is accomplished by an EG&G high-purity germanium solid-state detector connected to a PC via ADCAM hardware and MAESTRO software, which perform the necessary analogue to digital conversions and amplification. The energy resolution of the detector is ca. 1.5%, with a maximum count rate of approximately 10000 cps.

The advantages of using an energy dispersive technique are related to the fixed angle geometry and to the high energy of the X-ray beam. Having everything fixed means that the illumination of the sample does not change as a function of transfer moment. For majority of problems the Q range covered in one measurement is not sufficient to define the structures of the reflectivity curve, hence, several runs at different angles are necessary. Therefore, the widths of slits are changed as a function of the incident angle in order to keep the illuminated area constant. The normalization between two successive runs is obtained by integrating the overlap region. The other advantage of this technique is related to the strong penetration of hard X-rays (Figure 4.3). Traditionally, the reflection of X-rays from solid / liquid interface requires the design of a special cell where the cell thickness is optimised to minimise the attenuation of the incident X-ray beam due to the absorption of the X-rays by the liquid. In the range of commonly used energies (1 keV to 12.4 keV) the absorption length of X-rays is about a few millimetres [25]. As we can see in figure 4.3 the attenuation of the transmitted intensity is important up until 25 keV (that is below ~0.5Å). After this energy the incident spectra in air and in liquid have virtually the same shape. Therefore the strong penetration of hard X-rays used by this spectrometer allows to study the electronic density profiles at solid / liquid interface even through 10cm of liquid without much attenuation in the reflected signal.

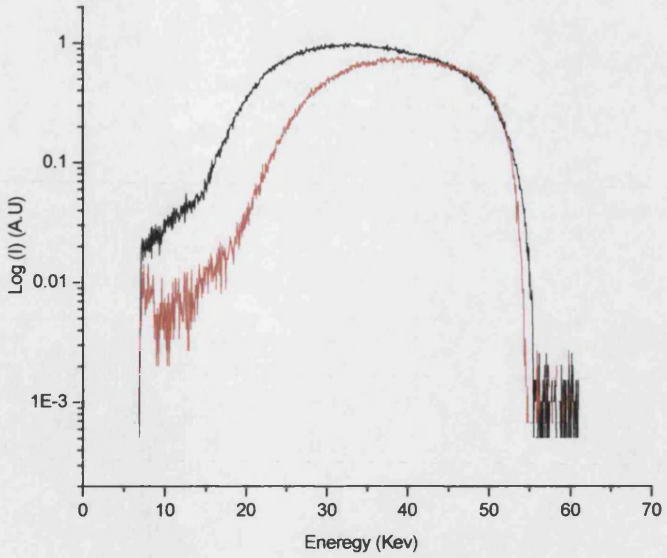

Figure 4.3.The variation of the intensity of the incident spectra as a function of energy. The black curve corresponds to the incident spectra in air and the red curve corresponds to the incident spectra in water

The reflected intensity is measured as a function of channel number. The detector has been calibrated in order to transform between channel number and energy by using the fluorescence of four different materials (tin, silver, barium, cadmium) in the energy range used in the experiment (13Kev to 55Kev). Once this relationship is established the equivalence between the channel number and the transfer moment, at a given incident angle θ_i, is expressed by $Q = (4\pi/12.4) \times \text{energy(channel)} \times \sin(\theta_i)$. Normalization of a raw reflection profile involves dividing the data by the measured incident spectra ("the white beam"). The measurement of the incident spectra is performed by putting the two arms in the straight position and collimating the beam by using the slits.

4.3) Poly (aniline) film formation by cyclic voltammogram (CV)

4.3.1) Introduction

Cyclic voltammograms for the formation of PANI films on the n-type silicon electrode in 0.5M H_2SO_4 +0.1M aniline aqueous solution, run in the range –0.2-0.9 V, at $1mV.s^{-1}$ under illumination, starting from –0.2V in the positive direction (Figure 4.4.a) exhibit the same features as the film grown on the platinum electrode (Figure 4.4.b) [7, 20].

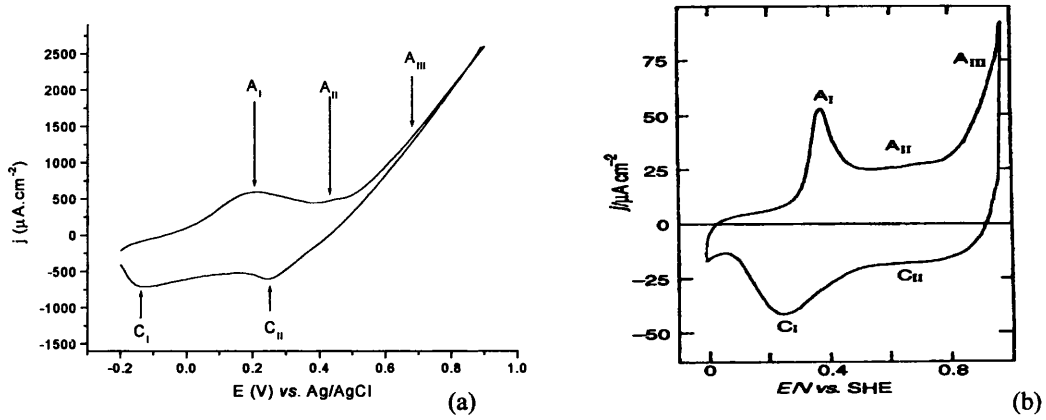

Figure 4.4. (a) Voltammogram (5th scan) run at 1mV.s^{-1} for PANI film formation on n-Si electrode in 0.5 M H_2SO_4 + 0.1 M aniline. The peaks A_I/C_I correspond to the electroformation of leucoemeraldine and the peak A_{II},A_{III} and C_{II} correspond to the formation of polyemeraldine. **(b)** Voltammogram (15th scan) run at 0.05 V.s^{-1} for PANI film formation on Pt in 0.5M H_2SO_4 + 0.1M aniline aqueous solution under N_2 saturation at 25 °C [20].

Initial reports of cyclic voltammetry on a platinum electrode stated that the voltammogram contained three different peaks [13]. However, further work using cyclic voltametry showed a more complex picture than initially proposed. It was found that the CV initially shows two processes with oxidation peaks located at approximately +0.15 V and +0.8 V, which correspond to the change of colour of the material from yellow to black, but that on cycling these peaks diminish in intensity and a third process become evident with an oxidation peak at approximately +0.5V, which increases in intensity as the initial two processes decrease [7, 13]. On the basis of theoretical calculation [13]the first anodic peak has been identified as the oxidation of the leucoemeraldine [20] (Figure 4.5.b) form of the polymer to produce an increasing

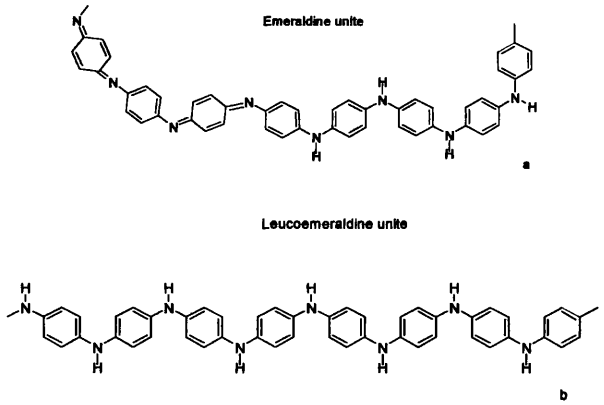

Figure 4.5. Two forms of units present during the electropolymerisation of aniline. **a)** Emeraldine unite. **b)** Leucoemeraldine unite

number of polyemeraldine forms by the end of the first cyclic voltammetric peak. The second peak is attributed, to degradation of material, which is accompanied by the rupture of electrode PANI [12], therefore the internal resistance of the material increases and shifts the redox peak toward positive potential [11] (Figure 4.6). Finally the third peak is attributed to formation of polyemeraldine (Figure 4.5.a) [13, 20].

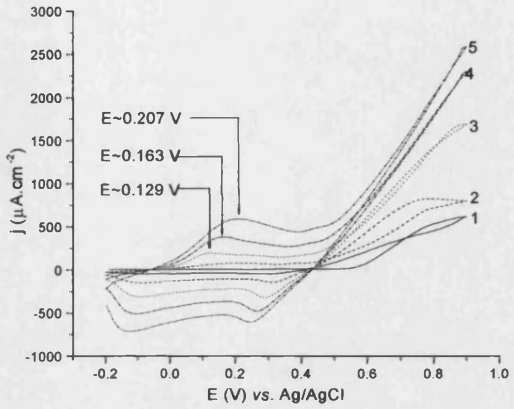

Figure 4.6. The anodic peak corresponding to the oxidation of the polymer is shifted toward the positive potential as the number of applied cycle increases.

From the cyclic voltammogram of PANI it is clear that the growth process follows different formation mechanism. The first three peaks correspond to the oxido-reduction reaction of the polymer film and the other component present in the solution. The increase in the current density observed at 0.9 V corresponds to the formation of the PANI film. However, it is difficult to decorrelate the charge transferred during the polymerisation and the charged transferred during the oxidatio or reduction of the other component present in the solution. As already discussed in the literature [7], the cathodic charge density of the cyclic voltammograms can be considered as a rough measure of the amount of the polymer formed during the multi-cycling, and very often is used to estimate the thickness of the films. This assumption can be justified if one suppose that only the polymer film present at the surface of the electrode is reduced during the reduction reaction. Therefore the amount of transferred charge is proportional to the amount of polymer present at the surface of the electrode. The relationship between the thickness and the charge is [22]:

$$d = \frac{\Phi M}{2SF\varphi}$$

Equation 4.1

where Φ is the charge (C) passed under the cathodic portion of the current for potential between –0.2V and 0.4V, M is the molecular weight ($g.mol^{-1}$), S is the surface area of the electrode (cm^2), F is the Faraday constant F=96500 $C.mol^{-1}$, φ is the density of the monomer ($g.cm^{-3}$).

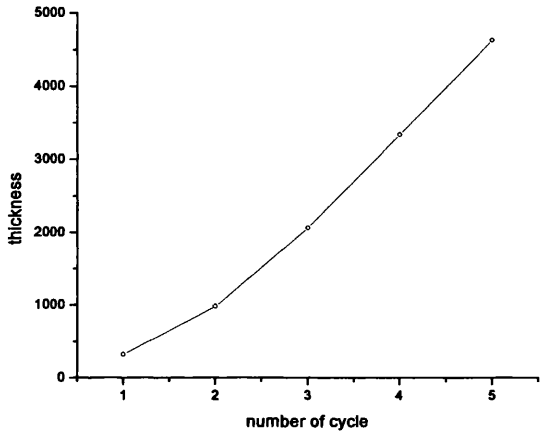

Figure 4.7. The variation of the thickness of the film calculated from the electrochemical data, by using the equation 4.1, as a function of the applied cycles.

The factor 2 in the denominator originates from the fact that 2 electrons are exchanged at each polymerisation process [13]. Figure 4.7 shows the variation of the calculated thickness as a function of number of cycles.

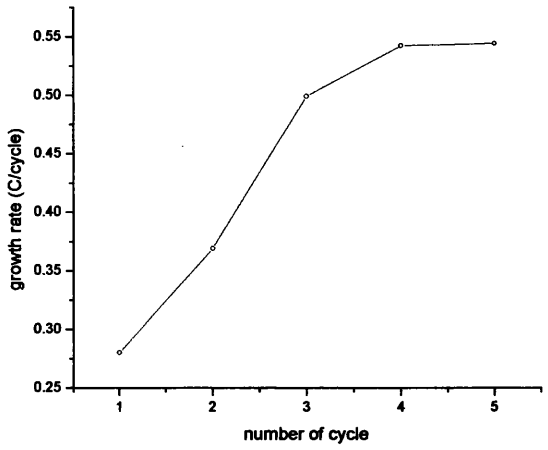

Figure 4.8. Growth rate *vs.* number of cycle

The calculated thickness from the electrochemical data seems to show that after the two first cycles the thickness of the film reaches 1000 Å. Figure 4.8 represents the growth rate of the PANI film as a function of number of cycle. It is defined as the difference between the total charges passed under the cathodic portion of the current during two successive cycles [7].

From figure 4.8 we can see there is a region which is characterised by a growth rate which increases linearly with cycle number. After some cycling time, the growth rate slows down and finally reaches a maximum value. For cycles beyond the maximum, the rate decreases [7]. The changes in the growth behaviour on the platinum electrode have been related to the build up of cross-linked polymers and other degradation by products in the film [7]. This build-up of undesirable reaction products would results in film with relatively poor charge transfer kinetics, and therefore very loose and rough [7]

In order to describe and to identify these processes we studied the structure of the PANI film by specular X-ray reflection.

4.3.2) PANI film growth: "dynamic" study

By the adjective "dynamic" we describe a situation where the reflected X-ray intensity from the electrode surface, in a finite range of transfer moment (Q), is collected as a function of time.

In order to study the formation of a PANI film on a n-type silicon electrode by cycling voltammerty (under illumination from a solution of 0.1 M aniline + 0.5 M sulphuric acid) we use the home made energy sensitive X-ray reflectometer. The high

energy X-rays photons produced by the tungsten tube source of this spectrometer allow us to study the electrode / electrolyte interface easily (through the electrolyte side), and the energy sensitive detector of the reflectometer set-up can collect the specular reflected intensity in a wide range of transfer moment in relatively short period of time (10 minutes) (Figure 4.9).

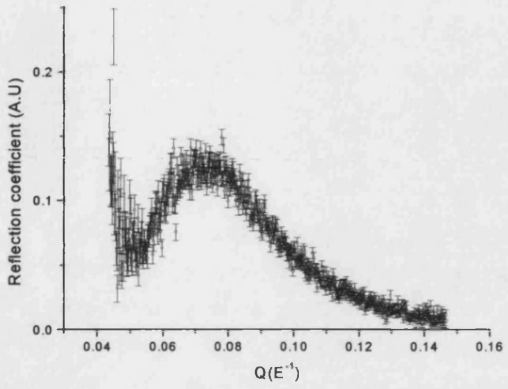

Figure 4.9. The reflection coefficient for the third applied ramp

Figure 4.10 represents the contour plot of the reflected intensity from the silicon electrode / electrolyte interface versus the number of potential ramp (x axis) and the transfer moment Q (y axis).

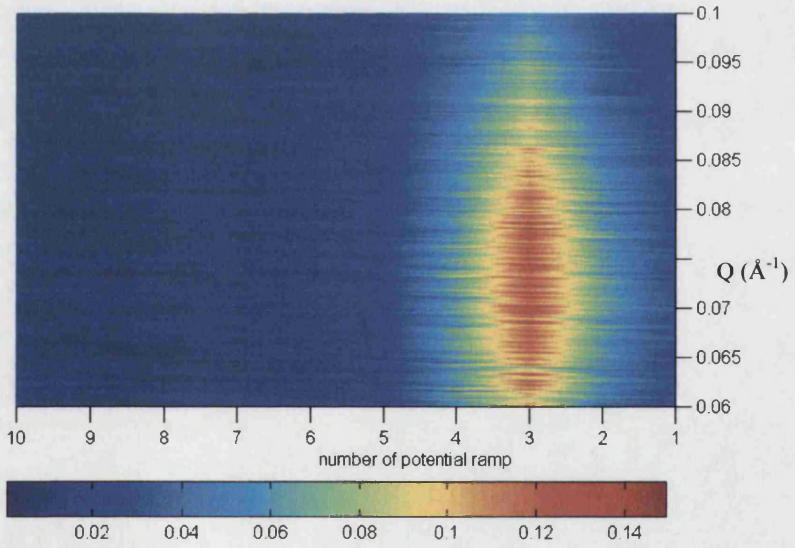

Figure 4.10. The *in-situ* variation of the reflected intensity as a function of the transfer moment during the electroformation of poly (aniline) by cyclic voltammetry.

The colour gradient is proportional to the amplitude of the reflected intensity. The dark blue colour corresponds to the lowest reflected intensity and the dark red colour corresponds to the highest reflected intensity. The measurement has been performed over a range of transfer momentum corresponding to [0.04,0.16] $Å^{-1}$. Figure 4.10 represents the contour plot of the reflected intensity in the range of transfer moment where the variation of the reflected intensity is most significant ([0.06,0.1] $Å^{-1}$). As we can see the intensity of the reflected beam increases as the number of applied cycle increases, and reaches a maximum at the end of the forward ramp of the second cycle and then the intensity of the reflected beam decreases gradually to reach the background value. Figure 4.11 shows the variation of the film factor (reflected intensity multiplied by the transfer moment to the power of four: $R \times Q^4$) as a function of the transfer moment for the first four applied potential ramps.

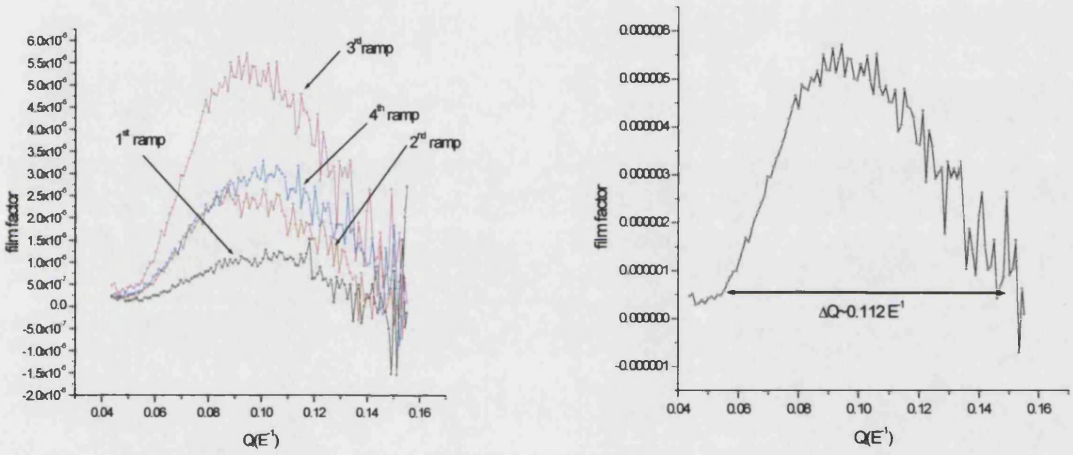

Figure 4.11. The figure in left hand side represents the variation of the film factor, for the first 4 potential ramps, as a function of the transfer moment. The figure in the right hand side represents the film factor for the 3rd ramp.

As we can see the amplitude of the fringe in the film factor increases for the first three ramps and reaches a maximal value for the third potential ramp. After the third ramp its amplitude decreases. However, the width of the fringe does not change as a function of applied potential ramp.

The width of the fringe in the film factor is proportional to the thickness of the film formed on the top of the electrode surface (see Chapter II). The analytical relationship between the thickness of the film and the width of the fringe is given by:

$$d = \frac{\pi}{\Delta Q}$$

Equation 4.2

As the width of the fringe after the third ramp, in the film factor, is equal to 0.112Å^{-1} (Figure 4.11) the calculated thickness of the film is equal to 36.120 Å. Figure 4.12 shows the variation of the calculated thickness, by using equation 4.2, and the applied

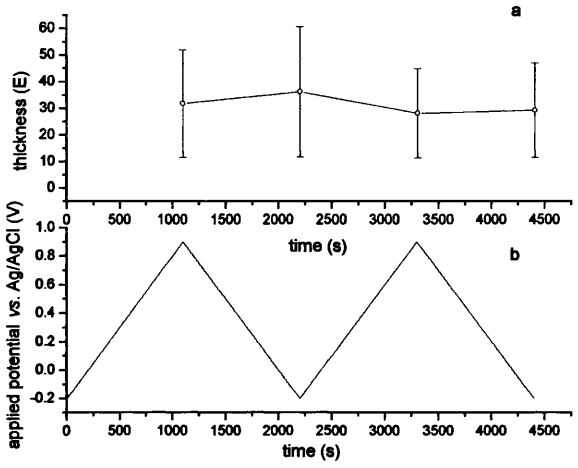

Figure 4.12. a) Variation of the thickness of the film calculated from the width of the fringes in the film factor by using equation 4.2 as a function of time for the first two cycles. **b)** Varaiation of the applied potential as a function of time for the first two cycles.

potential as a function of time for the first two cycles.

As we can see after the first ramp the thickness of the film reaches a constant value in the limit of the error bars. In fact after the end of the second cycle, it becomes very difficult to measure the width of the fringes since the value of the background scattering has changed dramatically.

However the thickness found after the second cycle by X-ray reflectivity is far from the value calculated by using the total charge passed under the cathodic part of the current

As we noticed before, the amplitude of the fringe changes as a function of number of applied ramps. Its value is a combination between the thickness, the scattering length density and the roughness parameter which define the polymer film (See Chapter II). Figure 4.13 shows the variation of the reflection coefficient as a function of time at a fixed Q corresponding to the position of the maximum intensity. (Q=0.0995 Å^{-1}).

The amplitude of the reflection coefficient increases for the first three potential ramps. Then as the number of applied potential ramps increases further, finally the amplitude

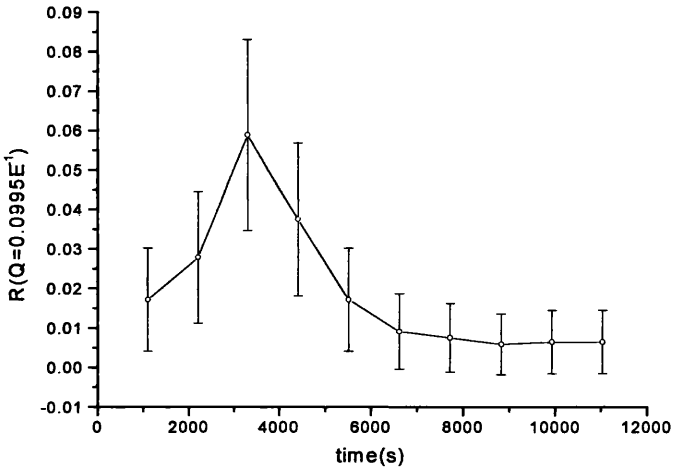

Figure 4.13. Variation of the reflection coefficient as a function of time at Q=0.0995 $Å^{-1}$

reaches a constant background value.

As we demonstrated the thickness of the film reaches a constant value of 36.12 Å after the application of the first potential ramp. Therefore the increase in the value of the reflection coefficient can be attributed to the increase of the density of the film and the decrease in the amplitude of the reflection coefficient to the catastrophic roughening of the formed film. Hence, these results suggest that the growth process of the PANI film has two phases: initially a two dimensional dense layer of 36.12 Å thickness, is formed at the surface of the electrode. After the second cycle the film creates a more open structure at the top of this dense layer which is so rough that it gives no fringes in the reflectivity profile. However, the value of the thickness measured by the reflectivity technique does not correspond to the value calculated using the electrochemical data (a thickness of 1000 Å is calculated by using the electrochemical data).

4.3.3) PANI film growth: "static" study

By the adjective "static" we describe a situation where the film is already formed. Figure 4.14 represents the reflection profile of a PANI film (formed on a n-type silicon electrode after 5 cycles under illumination from a solution of 0.1 M aniline+0.5 M sulphuric acid) at the solid/air interface.

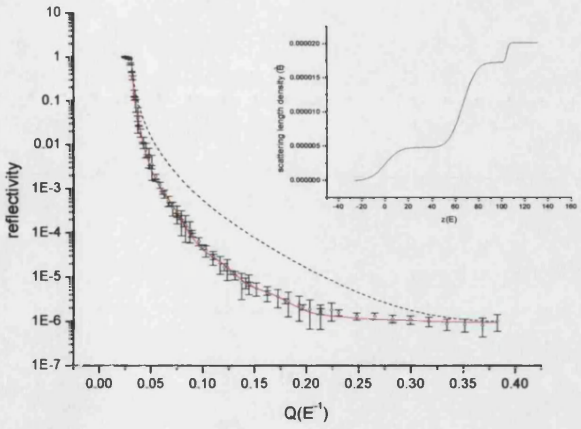

Figure 4.14. The reflectivity profile from polymer film formed by cyclic voltammetry after 5 cycles at air interface. The dashed line corresponds to the reflectivity curve from silicon/air interface. The red line corresponds to the fit and the black squares correspond to the experimental data. The scattering length density profile is presented in the top right insert.

In figure 4.14 the dashed line is the specular reflectivity profile from the silicon/air interface. The figure in the top right corner of the figure 4.14 is the scattering length density (SLD) profile of the silicon/PANI/air interface. This SLD profile has been obtained by fitting the data using the Parrat formalism [26]. We used a model consisting of two layers ($\chi^2_{2\ layer}$=2.4790*10^{-2}) the details of parameters used to fit the data are presented in the table 4.1

Layer	Thickness (Å)	Scattering length density (Å^{-2})	Roughness (Å)
Air	-	-	-
1	66.26	4.814*10^{-6}	14.108
2	38.38	1.726*10^{-5}	13.254
Silicon (substrate)	-	2.012*10^{-5}	2

Table 4.1. The fitting parameters used to fit the data of figure 4.14

The value of the SLD of the second layer is high compared to the value for the liquid aniline (9.3×10^{-6}Å^{-2}). However, the difference between the values of the SLD of the first and second layer gives us an idea about the structure of PANI film normal to the surface of the electrode. The values of the SLD suggest that the PANI film is formed of two different parts. The first part, which is close to the electrode surface, is a 38.38 Å dense film. The second part is formed from a looser polymer film. The high value of roughness parameters suggests that the interface between the film and the two

surrounding media is not very well defined. This roughness can be due to a geometrical roughness or the interpenetration of the two media.

The fitting suggests that the total thickness of the formed PANI film after 5 cycles is around 100 Å, but this is really poorly defined. The film can be considered as a dense part next to the electrode and of a looser part in the external region. In order to check this observation we measured the X-ray reflectivity profile of the same PANI film under water. Figure 4.15 shows the reflected profile of the PANI film under water.

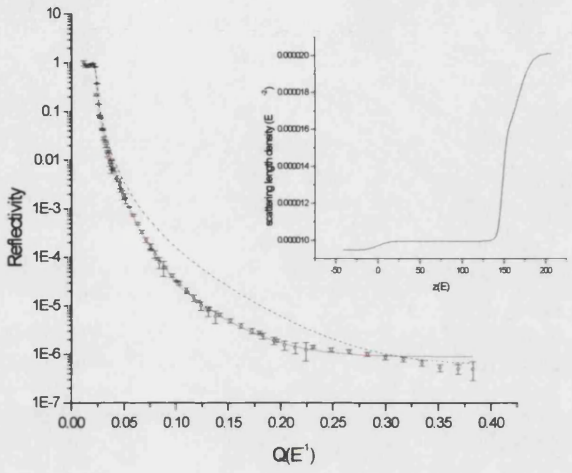

Figure 4.15. The reflectivity profile from polymer film formed by cyclic voltammetry after 5 cycles at water interface. The dashed line corresponds to the reflectivity curve from silicon/water interface. The red line corresponds to the fit and the black squares correspond to the experimental data. The scattering length density profile is presented in the top right insert.

The details of the fitting parameters are described in table 4.2.

Layer	Thickness (Å)	Scattering length density ($Å^{-2}$)	Roughness (Å)
Water	-	$9.475*10^{-6}$	-
1	147.66	$9.962*10^{-6}$	15.611
2	17.82	$1.499*10^{-5}$	5.26
Silicon (substrate)	-	$2.012*10^{-5}$	18.518

Table 4.2. The fitting parameters used to fit the data of figure 4.15

As in the case of the reflectivity from silicon/PANI/air, we modelled the data by using the Parrat formalism. Once again we used again two layers to model the PANI film

($\chi^2_{2\ layer}$=6.6144*10^{-2}). We cannot clearly distinguish between the surrounding water and the outer layer. The overall thickness of the PANI film has increased ($d_{2\ layer}$~165Å), compared to the values obtained by fitting the reflectivity profile from silicon/PANI/ air interface.

The SLD values of each layer are still high. The shape of the SLD profile gives us a qualitative idea about the structure of the PANI film. One of the reasons that it is very difficult to model these reflectivity profiles (both silicon/PANI/air and silicon/PANI/water) by the classical techniques is the fact that these methods cannot accurately model systems that possess very high roughness (see Chapter II and V). In fact, for a very rough film (geometrical roughness or in plane inhomogeneities in SLD) the error on the position of the specular reflection peak (in the Q space) at a given incident angle becomes more important [27, 28]. Since we do not have access to the quantitative description of the in-plane structure of the PANI film we cannot obtain from the specular reflection profile absolute quantitative values for the thickness, density and roughness of the film. However, by comparing the data and the fit obtained from the silicon/PANI /air and silicon/PANI/water interface we can have a qualitative idea about the structure of the PANI film in the direction normal to the silicon electrode.

All these observation drive us to the conclusion that the PANI film formed by cyclic voltametry is formed of two parts: the first part is a thin layer of dense polymer film near the surface of the electrode. This layer is completed after the second cycle. Then the mechanism of the film formation changes and a more open structure is formed. This layer, formed by looser polymer packing, corresponds to the second part of the PANI film. The fact that the thickness of the overall film and the roughness of the external layer increases when the PANI film is placed in the water media suggest that the second part of the film is formed of a porous material, which allows water to penetrate into the pores and make the film swell. This conclusion is supported by the fact that the classical fitting algorithm used here to model the data cannot fit the data accurately; we explained this failure by considering the film to be very rough. This hypothesis is confirmed by a Brewster Angle Microscope (BAM) picture of a poly(aniline) film formed by cyclic voltametry (Figure 4.16).

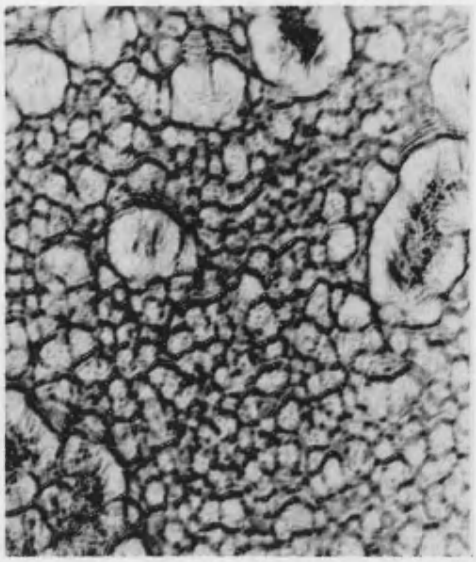

Figure 4.16. The Brewster angle microscope image of the PANI film after 5 cycles.

As we can see the film presented here is porous and very rough. The resolution of the BAM is 400 × 400 μm^2. The grey colour corresponds to the holes and the black one to the contours of the polymer film.

4.3.4) Conclusion

In this section we studied the growth of the poly (aniline) film on n-type silicon electrode by potential cycling technique. We showed that the polymer film formed on the silicon electrode exhibits the same features as the one grown electrodynamically on a platinum electrode. However, the thickness of the film calculated from the electrochemical technique is very different from the one measured by X-ray reflectivity.

The inner layer of the polymer film seems to be completed after the two first cycles and be formed of a dense layer. The X-ray reflectivity measures a thickness of 36.12 Å while the thickness suggested from the electrochemical data is about 1000 Å. It is reported in the literature that for PANI films of thickness less than 100 nm (1000 Å), the interface film / air is relatively smooth [20, 21]. We reach the same kind of conclusions by analysing the *in situ* measurements. For the first four applied potential ramps the thickness of the film does not change and the scattering length density of the film increases, however after the fourth potential ramp the reflected intensity from the film decreases due to the roughening of the film/solution interface. However, the value of the thickness extracted from the X-ray reflectivity data is significantly less

than the one calculated using the electrochemical data. This difference could be explained by the fact that the current measured during the electrochemical experiment does not correspond only to the PANI film formation and contains the participation of other processes. Therefore, the thickness suggested by electrochemical data is not reliable. The second interesting point in this work is that we are able to observe the presence of a rough porous layer by X-ray reflectivity. In fact by using the difference in scattering length density between water (9.45×10^{-6} $Å^{-2}$) and air (0 $Å^{-2}$) we were able to observe the penetration of water into the top layer of the film and therefore we concluded that the film must be porous. This conclusion has been confirmed by a BAM picture of the film / air interface.

In the next section we will discuss the case of a film grown at constant potential on top of a silicon electrode, these films are supposed to be of poorer quality and rougher than the film grown by using cycling potential [20].

4.4) Potentiostatic growth.

A current transient from the constant-potential electropolymerization of aniline in sulphuric acid on a n-type silicon electrode is presented in figure 4.17. The PANI film is formed at 0.9 V *vs.* Ag/AgCl on the n-type silicon electrode in 0.5M H_2SO_4 +0.1M aniline aqueous solution under illumination. The potential is held for 1000s and the transient current is recorded.

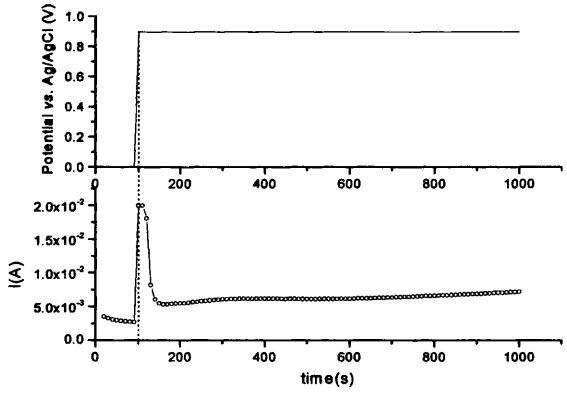

Figure 4.17. The top curve corresponds to the variation of the applied potential as a function of time. The bottom curve corresponds to the current produced during the potential step experiment.

The potential is kept constant, equal to 0 V, for 100s and then it is switched to 0.9V and kept at this value for 900s. As we can see from the cyclovoltamogram anodic wave (figure 4.4.a) at this potential the aniline monomer is oxidized and the

polyemeraldine form of poly (aniline) is formed [13]. During the initial stage (when the potential is switched from 0 to 0.9V) the anodic current increases with time. This increase corresponds to the instantaneous oxidation of the aniline monomers. Figure 4.18 represents the chronoamperogram, after the initial stage, during the electropolymerization at 0.9 V.

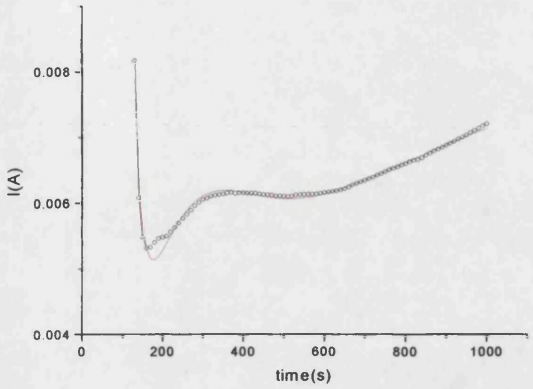

Figure 4.18. The current produced during the electroformation of PANI by a potential step on a silicon electrode under illumination. The open circles are experimental data and the red line is the fit by the equation?

As we can see the current transient exhibits a complex behaviour (figure 4.18). The deconvolution of these current transients is consistent with the participation of at least three processes. Initially a rapid decrease in the apparent current is observed which follows the exponential relationship:

$$I_1 = 0.02024e^{-0.04841t}$$

Equation 4.3

The value of I_1 corresponds to the initial relaxation of the charge preceding the growth of surface species at active substrate sites [20]. This process occurs at the same time as the growth of the PANI film [20]. In this case the apparent current follows the expression developed in reference 20:

$$I_2 = 0.00087t^{0.30967} + 0.00004te^{-0.00005t^2}$$

Equation 4.4

The first term in equation 4.4 corresponds to the three dimensional growth of a self-affine structure [20, 29] the second term corresponds to the instantaneous growth of a

two-dimensional structure [20, 30]. By following the analysis made in reference20, we should use an exponential term in order to model the polymer branching:

$$I_3 = 2.112 \times 10^{-9} e^{0.00738t}$$

Equation 4.5

Hence, this term can be neglected when compared to the two others terms. The entire current transient will be satisfactorily reproduced by considering the total current as the sum of the two currents (figure 4.19)

$$I = I_1 + I_2$$

Equation 4.6

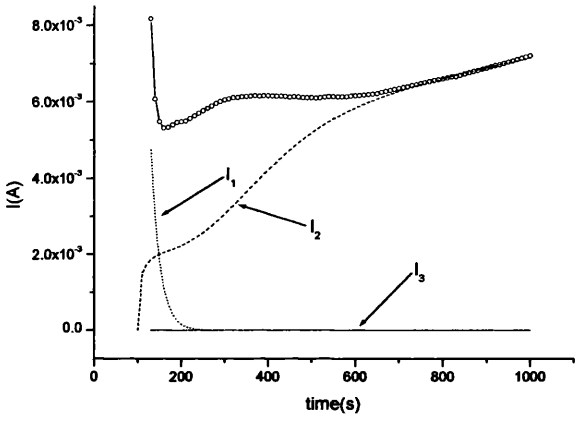

Figure 4.19. This figure represents the decorrelation of the current transient. It shows that it is formed by the sum of two processes.

By integrating the current transient as a function of time we obtain the total amount of charge transferred during the electropolymerization, and by using equation 4.1 we obtain the thickness of the PANI film:~ 2000 Å.

At this stage of the presentation of the results we need to clarify few points. The first term in equation 4.4 (the power law) starts to become important after a certain amount of time and dominates the growth process at large times. Therefore, the poly (aniline) film must be formed of two parts: a first part close to the electrode surface which is very compact and has been formed by a two-dimensional growth process. The second part is an open structure on the most outer part of the film formed by the self-affine process; therefore this part must have a very rough surface. In order to verify the proposed structure of the PANI film we undertook some X-ray reflection on the PANI film in two different mediums: air and water.

Figure 4.20 represents the reflectivity profiles from the sample/air interface.

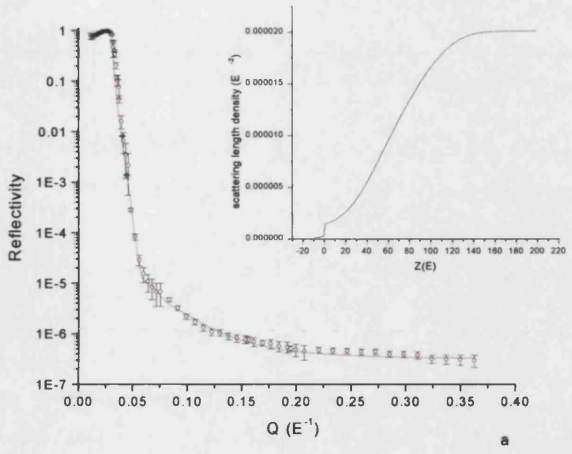

Figure 4.20. The reflectivity profile from polymer film formed by potential step at air interface. The red line corresponds to the fit and the black squares correspond to the experimental data. The scattering length density profile is presented in the top right insert.

As we can see the drop in the reflectivity profile is very sharp (the drop in the reflectivity profile is faster than $1/Q^4$) therefore the PANI film has a very rough interface with air. Data are fitted with Parrat formalism. The red line corresponds to the fit. The data has been modelled by a system composed of two layers ($\chi^2_{2\ layer}=6.9638*10^{-2}$) (figure 4.20). Values of the fitting parameters are shown in table 4.3.

Layer	Thickness (Å)	Scattering length density ($Å^{-2}$)	Roughness (Å)
Air	-	-	-
1	46.99	$1.172*10^{-6}$	0
2	47.57	$1.213*10^{-5}$	34.354
Silicon (substrate)	-	$2.012*10^{-5}$	35.889

Table 4.3. The fitting parameters used to fit the data of figure 4.20

The value of the roughness parameter for PANI / air interface seems to be unlikely (table 4.3) and the value of the scattering length density of the closest layer to the electrode surface is also large compared to the SLD of the liquid aniline.

The reflectivity profile from the same sample under the water is shown in figure 4.21

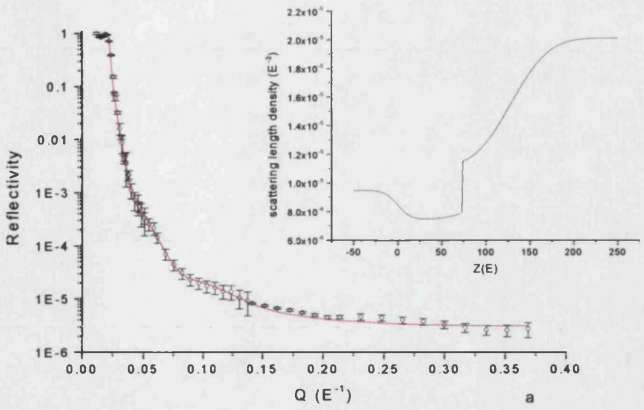

Figure 4.21. The reflectivity profile from polymer film formed by potential step at water interface. The red line corresponds to the fit and the black squares correspond to the experimental data. The scattering length density profile is presented in the top right insert.

The reflectivity profile has once again been fitted by using Parrat formalism. A two layer model has been used ($\chi^2_{2\ layer}=1.3862*10^{-2}$). Values of the fitting parameters are presented in table 4.4.

Layer	Thickness (Å)	Scattering length density ($Å^{-2}$)	Roughness (Å)
Water	-	$9.475*10^{-6}$	-
1	73.11	$7.463*10^{-6}$	16.814
2	55.38	$1.098*10^{-5}$	0
Silicon (substrate)	-	$2.012*10^{-5}$	47.942

Table 4.4. The fitting parameters used to fit the data of figure 4.21

However, in order to fit the reflectivity profile with two layers the roughness parameter of the substrate must be set to a very high value.

The interesting point is that total thickness of the film has increased in the water compared to the value of the total thickness of the film in the air. This observation suggest that the outer layer of the film is formed of a porous and loose polymer film therefore the water can penetrate into the film and change the thickness and the scattering length density of the polymer film. This hypothesis is supported by the

increase of the roughness parameter of the outer layer of the film. The value of this parameter increases when the medium is changed from air to water, this increase can be attributed to the diffusion of the water into the film.

The modelling process suggest that the polymer film is composed of two parts, the first layer is formed of a compact polymer film near the surface of the electrode and the second part is a loose polymer film in contact with the medium.

In this section we presented the data obtained by X-ray reflectivity during the growth of a poly (aniline) film on a n-type silicon electrode by cyclic voltammetry and potential step technique from an acidic solution. The analysis of the data suggests that the PANI film is formed of two parts: the first part is a compact polymer film and the second part is a loose and porous polymer film. However, the value of the scattering length density of the compact part of the film is too high. In the next section we will discuss the obtained results and the validity of this model. We will show how we can link the results obtained to the existing literature and we will point out the novelty of the set-up and the model that we used here to study the structure of PANI film.

4.5) Conclusion

In the last sections we presented the results obtained by *in-situ* and *ex-situ* X-ray reflection from an electropolymerised PANI film by potential dynamic technique and by potential step technique on a n type silicon [111] electrode. We showed that the film can be treated as two separate regions.

The novelty in this work, which allows us to use the X-ray radiation to follow the *in-situ* polymerisation of aniline, is the use of silicon as a working electrode. In fact all the published work (on the in-situ X-ray or neutron reflection from an electrochemical system) in the literature uses platinum [7, 20, 30] or gold [19] as working electrode. Scattering length densities of these materials are very high compared to silicon (silicon: 2.012×10^{-5} Å^{-2}, platinum: 14.5×10^{-5} Å^{-2}, gold: 13.14×10^{-5} Å^{-2}) and therefore it would be difficult to study the variation of the scattering length density at the electrode / electrolyte interface due to the polymerisation of a polymer (the scattering length density of the polymer film is expected to be in order of magnitude of 10^{-6}-10^{-5}) at the surface of these electrodes. As an example in figure 4.22 we represents the simulated reflectivity profile at electrode / air interface and scattering length density profile of the PANI film deposited by potential dynamic technique. In order to perform this simulation we use the values represented in table 4.1 and we only change

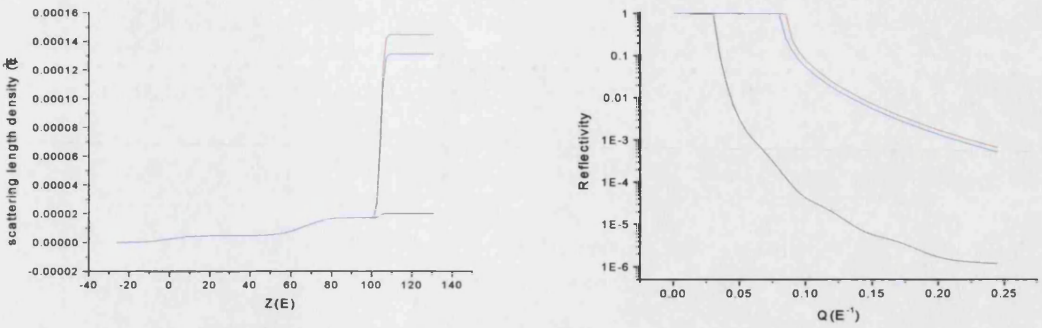

Figure 4.22. This figure represents the influence of the scattering length density of the substrate on the shape of the reflectivity profile. The figure in the left-hand side represents the scattering length density profile of the poly (aniline) film grown by potential dynamic technique for three different substrates: silicon (black), gold (blue) and platinum (red). The right-hand side figure represents the reflectivity profile for each system.

the value of the scattering length density of the electrode to the value of the scattering length density of platinum and gold respectively.

As we can see in these simulations in the case of gold or platinum the reflected intensity is mainly due to the working electrode and it is difficult to observe interference fringes due to the presence of the PANI film on top of the electrode. However, because the scattering length density of silicon is lower than the two others materials it is easier to observe the interference fringes and therefore, to model the data. As was discussed in the section 4.3.3 and 4.4 the outer part of the poly (aniline) film is porous. Therefore, the solvent can penetrate into the polymer film. The process of solvent penetration into the polymer film has been detected by X-ray reflectivity. However this effect can be detected more easily by neutron reflection. As silicon is relatively transparent to neutrons, the solid / liquid interface can be illuminated through the silicon electrode. Furthermore, by changing the degree of deuteration of the subphase the solvated polymer structure perpendicular to the electrode surface can be determined with high resolution. Therefore, the effect of solvent penetration can be used to resolve the structure of the polymer film by neutron reflection technique.

The interpretation of the *ex situ* and *in situ* X-ray reflectivity data, in correlation with the electrochemical data, helps us to propose a mechanism for the film growing processes. At the earliest stage of the of PANI film formation the aniline units create growing sites at the surface of the electrode. These growth centres undergo a two dimensional growing process and form a dense layer of poly (aniline) film. When the size of these centres reaches a critical value they begin to form a self-affine three-

dimensional structure. The latter structure corresponds to a loose and porous polymer film. However, the most problematic feature in this study was the roughness of the surface of the electrode. As the dimension of this roughness is large, the diffuse scattering from the surface of the sample perturbs the reflected intensity in the specular direction [28]. The classical numerical modelling techniques (Parrat, matrix method,..) do not take into account the effect of these large surface structures during the fitting of the reflectivity profile. In the next chapter we will develop a complete and self-consistent approach to describe the effect of this large roughness on the specular reflectivity profile.

References:

1 R. Noufi, A. J. Nozik, J. White, et al., J. Electrochem. Soc **129**, 2261 (1982).

2 J.-C. Lacroix, J.-L. Camalet, S. Aeiyach, et al., Journal of Electroanalytical Chemistry **481**, 76 (2000).

3 J.-L. Camalet, J.-C. Lacroix, T. D. Nguyen, et al., Journal of Electroanalytical Chemistry **485**, 13 (2000).

4 A. R. Hillman, A. Glidle, R. M. Richardson, et al., Journal of American Chemical Society **120**, 12882 (1998).

5 C. M. G. S. Cruz and E. A. Ticianelli, Journal of Electroanalytical Chemistry **428**, 185 (1997).

6 H. Yang, N. Coombs, O. Dag, et al., Journal of material chemistry **7**, 1755 (1997).

7 D. E. Stilwell and S.-M. Park, J. Electrochem. Soc **135**, 2254 (1988).

8 S. J. Roser, D. J. Caruana, and M. Gerstenberg, Journal of Electroanalytical Chemistry **411**, 153 (1996).

9 R. M. Richardson, M. J. Swann, A. R. Hillman, et al., Faraday Discuss **94**, 295 (1992).

10 L. Bailey, M. J. Henderson, A. R. Hillman, et al., Physica B **276-278**, 373 (2000).

11 H. N. Dinh, J. Ding, S. J. Xia, et al., 1998 **459**, 45 (1998).

12 V. E. Kazarinov, V. N. Andreev, and M. A. Spitsyn, Electrochemica Acta **41**, 1757 (1996).

13 G. P. Evans, in *Advances in Electrochemistry Science*, edited by H. Gerischer and C. W. Tobias (Verlagsgesllschaft, New york, 1990), Vol. 1.

14 J. C. Lacroix, K. K. Kanazawa, and A. Diaz, J. Electrochem. Soc **136**, 1308 (1989).

15 J. Yano, T. Ohnishi, and A. Kitani, Synthetic Metals **101**, 752 (1999).

16 A. Watanabe, K. Mori, Y. Iwasaki, et al., Journal of polymer science: Part A: Polymer Chemistry **27**, 4431 (1989).

17 A. Kitani, J. Izumi, J. Yano, et al., Bull. Chem. Soc. Jpn **57**, 2254 (1984).

18 H. Yang and A. J. Bard, J. Electroanal. Chem. **339**, 423 (1992).

19 K. Roβberg, G. Paasch, L. Dunsch, et al., Journal of Electroanalytical Chemistry **443**, 49 (1998).

20 M. E. Vela, G. Andreasen, R. C. Salvarezza, et al., J.CHEM. SOC. FARADAY TRANS **92**, 4093 (1996).

21 E. C. Venancio, C. A. R. Costa, S. A. S. Machado, et al., Electrochemisty Communications **3**, 229 (2001).

22 G. Mengoli and M. M. Musiani, Progress in Organic Coatings **24**, 234 (1994).

23 R. Greef, M. Kalaji, and L. M. Peter, Faraday Discussion Chemical Society **88**, 277 (1989).

24 K. Itaya, R. Sugawara, Y. Morita, et al., Applied Physics letter **60**, 2534 (1992).

25 Z. Nagy, H. You, R. M. Yonco, et al., Electrochimica Acta **36**, 209 (1991).

26 L. G. Parratt, Physical Review **95**, 359 (1954).

27 J. Daillant and A. Gibaud, *X-Ray and Neutron Reflectivity: Principles and Applications*, 1999).

28 D. K. G. d. Boer, Physical Review B **49**, 5817 (1993).

29 L. Barbabsi and H.E.Stanley, *Fractal Concepts in Surface Growth* (Cambridge university press, Cambridge, 1995).

30 R. D. Amstrong and J. A. Harrison, J.Electrochemical Societey : Electrochemical Science **116**, 328 (1969).

Chapter V

Specular reflectivity from textured surfaces

"The huger the mob, and the greater the apparent anarchy, the more perfect is its sway. It is the supreme Unreason. Whenever a large sample of chaotic elements are taken in hand and marshalled in the order of their magnitude, an unsuspected and most beautiful form of regularity proves to have been latent all along. The tops of the marshalled row form a flowing curve of invariable proportions, and each element, as it is sorted into place, finds, as it were, a preordained niche, accurately adapted to fit it."

Francis Galton, Natural Inheritance

5.1) Introduction

In the geometrical optics approximation the optical laws are formulated in the language of geometry. The energy radiated may then be regarded as being transported along certain curves (light rays)[1]

In practice, one can use the laws of geometrical optics as long as the wavelength of the electromagnetic wave can be neglected in comparison with the dimension of the scattering object. On reducing the size of the scattering objects down to the dimension of the wavelength, phenomena appear which need more refined study [1].

In this chapter we investigate the possibility of using the geometrical optics laws in order to describe specular reflection of X-rays or neutrons from rough surfaces.

A rough surface is described in term of lateral (in plane) correlation length (ξ) and the root-mean-square (rms) surface height variation $(\sigma)^2$. It is known that for a rough surface the specular reflectivity, among other things, depends on the rms value of the surface roughness [3]. If R is the reflection coefficient from a smooth surface, the intensity of the specular reflectivity from a rough surface is reduced by a factor depending on σ. This factor has two forms: The first form, which is generally applied at large Q [4], is the *static Debye-Waller* factor (DW) [5]; and the reflectivity coefficient for a rough surface becomes:

$$R_{rough} = R \cdot e^{-Q^2\sigma^2}$$

Equation 5.1

The second form, which is generally applied in the vicinity of the region of total reflection [4], has been formulated by *Nevot and Croce* (NC) [6, 7], Where the reflectivity coefficient for a rough surface can be written as:

$$R_{rough} = R \cdot e^{-QQ'\sigma^2}$$

Equation 5.2

Where Q is the perpendicular moment of the wave vector of the incident wave, and Q' is the perpendicular moment of the wave vector inside the material, after refraction.

The lateral correlation length produces nonspecular scattering (see Chapter II)[8], it is somewhat contra intuitive that it should also influence the specular reflectivity.

In order to solve the general problem of scattering by rough surfaces of different kind of waves, several methods, all based on diffraction theory, have been proposed. The older and most celebrated theories are due to Lord Rayleigh and Kirchoff [5]. More specifically, methods based upon the Born approximation [8], the distorted-wave Born approximation (DWBA)[8], and the use of Green functions have been more recently applied to solve the problem of scattering of X-ray by a single rough surface. However, all these methods suppose that the in-plane correlation length of the rough surface is smaller or equal to the dimensions of the coherence length of the incident wave.

De Boer [4] showed that the NC and DW form of the reflectivity coefficient (Equation 5.2 and 5.1 respectively) are the limiting case of a more general form. He showed that the exact form of the factor containing the effect of the roughness depends on the lateral correlation length of the roughness profile. De Boer derived the general expression using the second-order distorted-wave Born approximation:

$$R_{rough} \approx R_0 \cdot e^{\left[-2QQ'\sigma^2 - \frac{1}{2\pi^2}QQ_c^2 \int_{|p_{II}|} \frac{dp_{II}}{p_0+p_1} C(p_{II}-Q_{II})\right]}$$

Equation 5.3

Where $p_{\|}$ corresponds to the in-plane modes of the surface, Q_c is the critical transfer moment of the material and p_0 and p_1 are two specific modes of the surface, R_0 is the reflection coefficient from the sharp interface. However, in his derivation he supposed that the rms value of the surface roughness is small, and can be analysed as a perturbation to the smooth surface. Also he assumed that the lateral correlation length ξ is smaller than the coherence length of the radiation parallel to the surface [4].

In this chapter we follow a method developed by Daillant et al [9] . Their theory is based on a method originally suggested by Croce and co-workers [6, 7, 10, 11]. The main advantage of this method is to give a transparent description of the scattering mechanisms in term of electric field (we have already introduced this method in Chapter II).

The chapter is organized as follow: In the second section we discuss the general conditions under which the geometrical optics approximation is valid. The vector form of the reflection law is given in the third section. In the fourth section a complete and rigorous treatment of the specular reflection by optical geometry approximation in the case of arbitrary rough surface is given. In the fifth section we present the general conclusions.

5.2) Conditions and limits of validity of geometrical optics [1]

According to traditional terminology, in geometrical optics electromagnetic energy is transported along a *light ray*. These rays are perpendicular to the *wave fronts* (Fig.5.1).

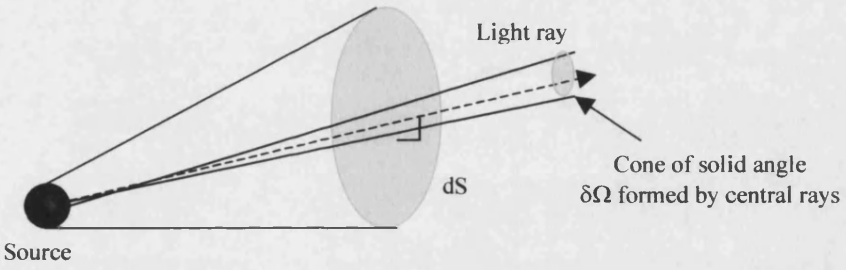

Figure. 5.1. Illustrating the configuration for the propagation of intensity law of geometrical optics.

The source may be regarded as arising from a large number of individual scattering centres. To obtain the intensity at a typical point P one has to sum the individual fields produced by each scattering centre (element of the source). If the fields are *incoherent* one can write the intensity at a point P as a function of the electromagnetic energy S:

$$I(P) = \left| \sum_n \langle S_n \rangle \right|$$

Equation 5.4

Where S_n is the electromagnetic energy due to the nth element of the source. The symbol $\langle\rangle$ represents the averaging over time. The exact definition of an incoherent field will be given later.

Let dS (Figure 5.1) be a small portion of a wave-front associated with one particular element of the source. Every element of the source sends a tube of rays through dS, and the central rays of these tubes fill a cone of solid angle $\delta\Omega$. The energy scattered

by each centre, S_n, depends on the direction of propagation. The total energy flux, which crosses the element dS per unit of time, is given (in the continuous limit) by:

$$\delta F = B\delta\Omega ds$$

Equation 5.5

Where B depends on the direction of propagation.

We must now briefly consider the limits of validity of geometrical optics. The most important assumption, in this case, is to consider that the magnitude of changes in the amplitude of the electric and magnetic fields are small compared with the magnitude of these fields over domains whose linear dimensions are of the order of a wavelength. In other words one must consider the dimension of the wavelength small compared to the dimension of each element of the source. If this condition is violated, geometrical considerations cannot be expected to correctly describe the behaviour of the field.

5.3) Geometrical optics expression for the reflection and refraction law

Firstly it is assumed that the changes of the refractive index, ν, are a continuous function of the space variable r, when the rays cross a surface, T, separating two homogeneous media of different refractive indices.

Let θ_1 and θ_2 be angles which the incident ray and the refracted ray make with the vector $\mathbf{n}_{12}$, the unit normal to the boundary pointing from the first into the second medium.

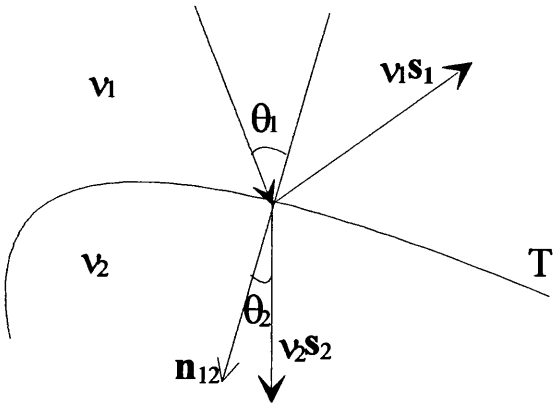

Figure 5.2. Illustrating the law of reflection

The direction of propagation of the beam is given by the vector vs sometimes called the *ray vector* (Figure 5.2).

In this case it is easy to notice that the classical law of refraction (Snell's law) can be expressed as a vector equation [1]:

$$v_2(\mathbf{n}_{12} * \mathbf{s}_2) = v_1(\mathbf{n}_{12} * \mathbf{s}_1)$$

Equation 5.6

where "*" represents a vector product. By expanding the vector product, the classical form of Snell's law can be find:

$$v_1 \sin(\theta_2) = v_2 \sin(\theta_1)$$

Equation 5.7

There are several advantages to considering the Snell's law in its vector form. It applies to waves and refracting surfaces of general form, and makes a direct link between the direction of the reflected beam and the normal to the surface. However, the vector expression can only be used provided that the wavelength of incident beam is sufficiently small. This condition means, in practice, that the radii of curvature of the incident wave and of the boundary surface must be large compared to the wavelength of the incident light [1].

5.4) Application of geometrical optics to the specular reflectivity from a rough surface

In this section we describe the specular reflectivity of X-rays and neutron in the frame of the geometrical optics. The main advantage of this method is its simplicity; it can be applied to any kind of rough surfaces as long as the surface profile is considered to be continuous and slowly changing. The important parameter in this method is the direction of the normal to the interface. It will be demonstrated that if one describes the interface in terms of the changes in the local normal direction one would be able to consider the surface as a two-dimensional Ising lattice [12] where the spins are replaced by the local normal. This analogy will help us to introduce the notion of coherence length and correlation length naturally by the use of basic scaling concepts [13].

5.4.1) Expression for the differential cross section of a series of radiating sources.

5.4.1.1) Case of one two-dimensional source

In an ideal scattering experiment one exactly measures the differential cross-section. It is defined as the flux of the electromagnetic energy (in the case of X-ray)

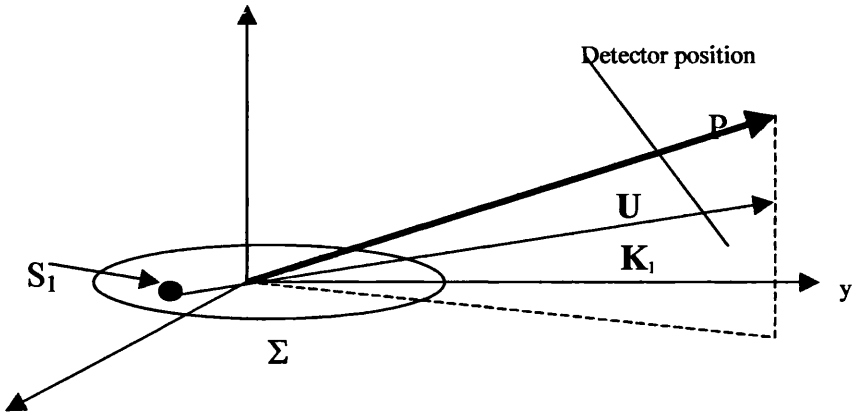

Figure 5.3. Illustration of a two-dimensional source S_1, positioned on a surface Σ, and radiating in the direction K_1. A detector in the direction U detects the radiation.

through a surface *ds* located at the position ***R*** of the detector. One assumes that the detector located at ***R*** is placed far from the source of the radiation (hence, the radiated field may be considered to be a plane wave, known as the 'far field approximation') [3]. Suppose that we measure the intensity, *I*, produced by point source S_1 at the point *P* (Figure 5.3) in the direction ***U***. Also assume that the source S_1 radiates an electric field E_1 in the direction K_1.

Maxwell's equations [14] imply for a plane wave that the electric field is perpendicular to the direction of propagation. Therefore:

$$\vec{E}_1.\vec{K}_1 = 0$$

Equation 5.8

We consider the pointing vector as the vector product between the electric field and the magnetic field:

$$\vec{\Pi} = \vec{E}(\vec{r},t) \times \vec{H}(\vec{r},t)$$

Equation 5.9

Where *E(r,t)* is the electric field and *H(r,t)* is the magnetic field. Again, by considering Maxwell's equations, the electric field is related to the magnetic field in a homogeneous and isotropic medium by:

$$\vec{K} \times \vec{E}(r) = \omega\mu\vec{H}(r)$$

Equation 5.10

Where *K* is the wave vector, which determines the direction of propagation of the electric and magnetic field. By introducing equation 5.10 into equation 5.9, using equation 5.8 and the following vector identity:

$$\vec{a} \times (\vec{b} \times \vec{c}) = \vec{b}(\vec{a}.\vec{c}) - \vec{c}(\vec{a}.\vec{b})$$

Equation 5.11

we find that

$$\vec{\Pi}(r) = \frac{E(\vec{r})^2}{\omega\mu}\vec{K}$$

Equation 5.12

This relation implies that the direction of propagation of the electromagnetic energy is given by the wave vector *K*. Therefore, the differential cross section of the radiation is equal to

$$\frac{d\sigma}{d\Omega} = \vec{\Pi}(\vec{R}).\vec{u}$$

Equation 5.13

Where U is the normal to the surface of the detector. If the angle between the direction of propagation and the normal U to the detector surface is defined as α, equation 5.13 may be written as:

$$\frac{d\sigma}{d\Omega} = \Pi(\vec{R})\cos(\alpha)$$

Equation 5.14

5.4.1.2) General case.

In their work on scattering from rough surfaces, *Nevot* and *Croce* , and later *Daillant et al* [10, 11, 15] used the reciprocity theorem in order to derive the electric field scattered by a rough surface at a distance r (where r is far from the surface). *Croce and Nevot* [11] suggest that one can decompose the rough surface to a series of independent sources, as illustrated schematically in figure 5.4.

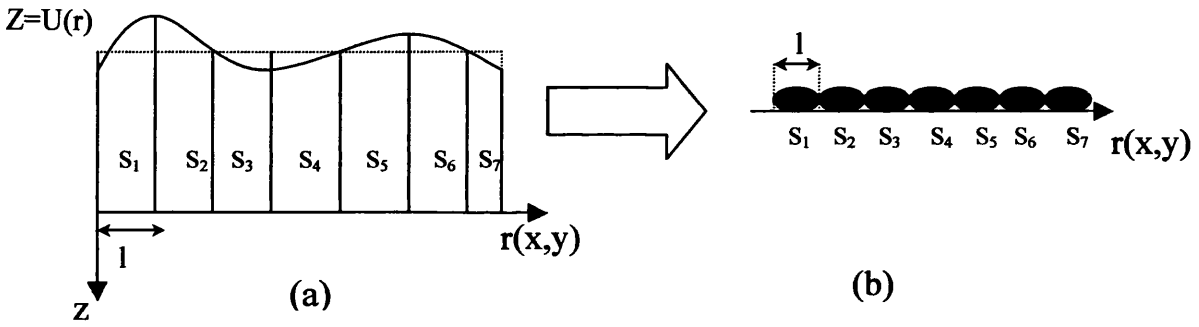

Figure 5.4. Schematic representation of the decomposition of the surface to a series of independent sources. (**a**) Represents a rough surface described by the surface profile U(r). l is the dimension over which the radiating points are correlated. (**b**) Represents the decomposition of the surface to a series of independent sources with dimension l.

In fact we can consider the sample to be cut into a series of *independent* domains of dimension l^2 (Figure 4.5a), such that the radiation from each domain is independent of the radiation from its neighbours, and l can be considered to be a coherence length of the incoming beam. Therefore, since two points outside the domain do not interact, the total energy radiated by the surface is given by the sum of the energy radiated by each domain [1]. In other words we can represent the sample as a series of independent sources positioned in the (xy) plane, as shown in figure 4.5.b. Thus, the total energy radiated by the ensemble of sources is given by

$$\vec{\Pi}_{total} = \sum_{i=1}^{n} \vec{\Pi}_i$$

Equation 5.15

where n is the number of sources at the surface and Π_i is the *pointing vector* of the i^{th} source. If the radiated energy is detected in a direction U, the total energy detected in this direction is given by:

$$\Pi_{total} = \sum_{i=1}^{n} \Pi_i \cos(\alpha_i)$$

Equation 5.16

where α_i is the projection angle between the scattering direction of the i^{th} source and the direction of observation. Until now we have considered that the surface consists of a series of discrete sources. However, as the number of these sources becomes large (1^2~10^{-10}-10^{-8}cm^2, the size of the illuminated area over the sample is generally around 5 cm^2, then the number of sources are around 10^6-10^8), we can replace the discrete sum with continuous distribution by considering that the radiated energy and the angle of radiation depends on the position of the source at the surface:

$$\sum_{i=1}^{n} \rightarrow \int_{surface}$$

Equation 5.17

In this continuous limit, equation 5.16 may be written as

$$\Pi_{total} = \int_{surface} \Pi(r)\cos(\alpha(r))dr$$

Equation 5.18

where r is the in-plane position vector. In physical terms, equation 5.18 means that over the large but finite surface S (surface area of the sample) in which r is defined, the total radiated energy depends on all the possible values that the angle α can take at any point of the surface. Now, if we assume that we know the distribution function, $P(\alpha)$, for the variable α over its statistical ensemble, we could imagine a situation

were α takes all its possible values at one point of the surface. Therefore, equation 5.18 can be re-written not as a function of the variable r integrated over the sample surface, but as a function of the angle of projection α integrated over its statistical ensemble. Relying on an *ergodic hypothesis* [12] to assert the following equality:

$$\Pi_{total} = \int_{surface} \Pi(r)\cos(\alpha(r))dr = \int_{\alpha_1}^{\alpha_2} \Pi(\alpha)\cos(\alpha)P(\alpha)d\alpha$$

Equation 5.19

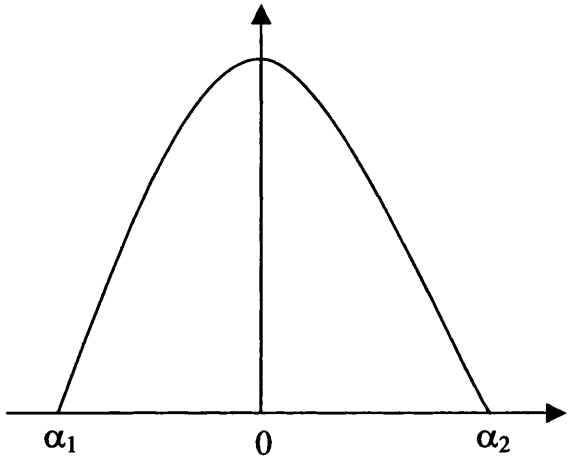

Figure 5.5. The general appearance of distribution function P(α). P(α) is small around two limits value α_1 and α_2 (the angular range imposed by the spectrometer or by the system) and large around 0 (i.e. the direction of observation and the direction of propagation are parallel)

The state of alignment of the pointing vector and the direction of observation U can be described by a distribution function $P(\alpha)d\alpha$ (giving the probability of finding pointing vectors in a small angle $d\alpha$.)

The direction of propagation is imposed by the position and the characteristics of the source (such as position, orientation). Therefore, the projection angle α must be linked to the characteristic parameters of the surface, and as we detect only the projection of the direction of propagation over the direction of observation U, the state of projection angle α and $-\alpha$ are indistinguishable. Therefore, the distribution function $P(\alpha)$ must be even, and its general appearance is shown in figure 5.5. Using equations 5.14 and 5.19, the differential cross section is therefore given by

$$\left\langle \frac{d\sigma}{d\Omega} \right\rangle_{\alpha} = \int_{\alpha_1}^{\alpha_2} \Pi(\alpha)\cos(\alpha)P(\alpha)d\alpha$$

Equation 5.20

Equation 5.20 will be the basis of our discussion. For instance, if P(α) is strongly peaked around α=0 (parallel alignment) and falls quickly to zero, the cosine term can be approximated to 1 and in this case the differential cross-section is equal to the pointing vector. This means that the direction of radiation and the direction of observation are parallel.

5.4.2) Reflected intensity from a rough surface

Equation 5.20 is the expression for the differential cross section from a rough surface. The detected intensity is given by the integral of the differential cross section over the solid angle Ω around the direction of observation, and normalised to the size of the radiating object. For example the detected intensity radiated by a surface of dimension *S* is proportional to:

$$I_r \propto \frac{1}{S} \int_{\text{detector}} \left\langle \frac{d\sigma}{d\Omega} \right\rangle d\Omega$$

Equation 5.21

As was pointed out earlier, *Croce and Nevot* [11] suggest that one can decompose the rough surface to a series of independent sources (Figure 5.4). In order to calculate the reflected intensity they decomposed the surface to an ensemble of non-interacting dipoles polarized by the incident beam and acting as a secondary sources (the reciprocity principle) [3, 15]. In this case the intensity of the reflected beam is proportional to the intensity, I_0, of the incident beam and equation 5.21 is written as,

$$I_r = \left[\frac{1}{S} \int_{\text{detector}} \left\langle \frac{d\sigma}{d\Omega} \right\rangle d\Omega \right] I_0$$

Equation 522

where the term in the bracket is known as the *reflection coefficient*, *R*. Therefore, by introducing equation 5.20 into the expression of the reflection coefficient we find that:

$$R = \int_{\alpha_1}^{\alpha_2} \cos(\alpha) P(\alpha) \left(\int_{detector} \Pi(\alpha) \frac{d\Omega}{S} \right) d\alpha$$

Equation 5.23

In order to derive equation 5.20 we consider the surface as a series of independent domains of dimension l^2. Therefore, the pointing vector $\Pi(\alpha)$ must be calculated over a domain of dimension l^2.

In this work we are interested to study the effect of the surface roughness on the *specular reflection* coefficient. In other words, that the angle of incidence and the angle of observation are equal ($\theta_{specular}$), as illustrated in Figure 5.6.

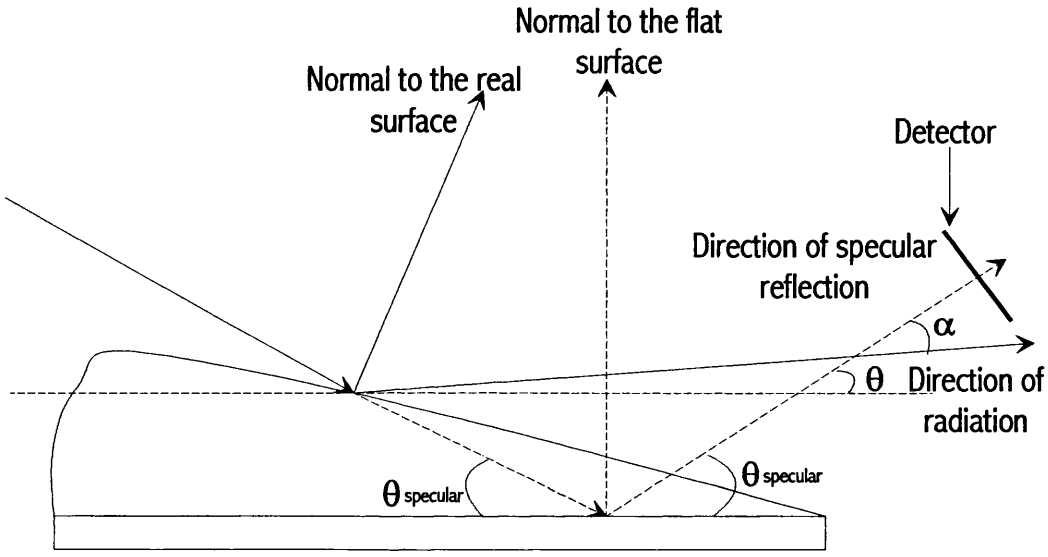

Figure 5.6 Reflection configuration. As can be seen, the divergence angle α can be written as the difference between the angle of specular reflection, $\theta_{specular}$, and the angle of radiation, θ.

As we can see the angle α can be considered as the difference between the ideal specular direction, $\theta_{specular}$ and the real angle of radiation θ. If we consider the surface to be ideally flat, the distribution function $P(\alpha)$ is very peaked around the value of $\alpha=o$. Therefore, equation 5.23 may be reduced to:

$$R_0 = \int_{detector} \frac{\Pi}{S} d\Omega$$

Equation 5.24

Equation 5.24 is the reflection coefficient from a system, in the limiting case, where all the local normals are parallel to each other and perpendicular to the ideal flat surface. For a more general case of nonzero α, equation 5.23 becomes

$$R(\theta_{specular}) = \int_{\alpha_1}^{\alpha_2} \cos(\alpha) P(\alpha) R_0(\theta_{specular} - \alpha) d\alpha$$

Equation 5.25

In this derivation we have considered only the specular component of the reflected intensity, and assumed that the spatial dimensions of the detector were infinite. Evidently, in real situations the detector has a finite size, and therefore has a range of acceptance angles in the plane of scattering. This experimental constraint therefore defines the limits of integration in equation 5.25.

Two limiting cases can exist (Figure 5.7). In the first case the angular acceptance of the spectrometer is wider than the angular divergence introduced by the sample (Figure 5.7.a).

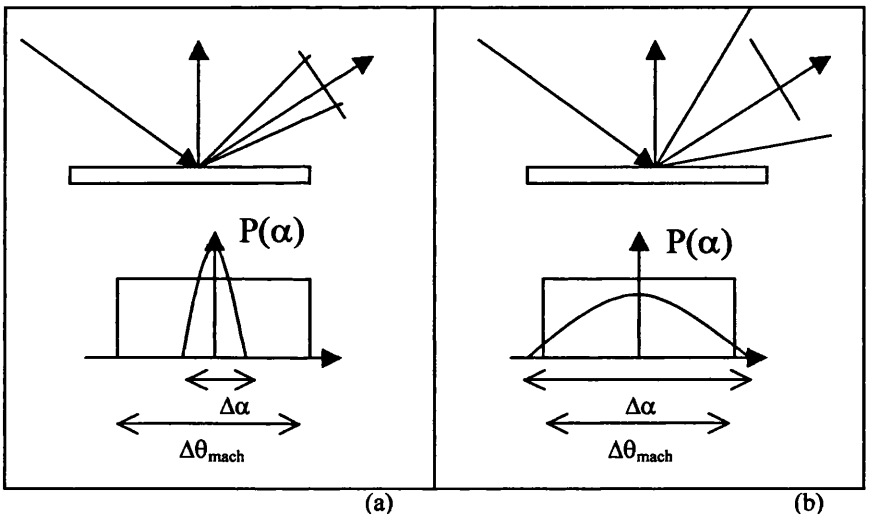

Figure 5.7 Schematic representations of two possible cases for the divergence of the reflected beam. (**a**) the divergence introduced by the sample is smaller than the acceptance window of the spectrometer. (**b**) the divergence introduced by the sample is bigger than the acceptance window of the spectrometer

Therefore, the detector can detect all the radiated intensities. In the second case the angular divergence introduced by the sample is bigger than the angular acceptance of the spectrometer (Figure 5.7.b). Therefore, the detector does not detect all the radiated intensity and the calculated intensity must be rescaled in order to take into account the angular spread of the reflected beam.

In fact, the first case corresponds to the scattering from a surface, which processes a very peaked distribution function around zero, and the second case is the case of a surface which possesses a rough surface with large in-plane correlation length. In order to calculate the scaling factor for the intensity in each situation, we need to define the angular range over which we calculate the intensity. Let $\Delta\theta_{mach}$ be the angular acceptance of the spectrometer and $\Delta\alpha$ the width of the angular divergence introduced by the sample. In the first case $\Delta\theta_{mach}$ is bigger than $\Delta\alpha$ therefore no scaling factor is needed. In the second case the situation is reversed the angular width over which we calculate the intensity is $\Delta\theta_{mach}$, therefore a scaling factor is needed. Therefore, we must multiply equation 5.25 by the following scaling factor:

$$A = \max\left(1, \frac{\Delta\alpha}{\Delta\theta_{mach}}\right)$$

Equation 5.26

The operator '*max*' chooses the maximal value between the two values. The first value corresponds to the case where the angular divergence of the reflected beam is smaller than the acceptance angle of the spectrometer and the second ratio to the case where the angular divergence of the reflected beam dominates. Finally we can write the calculated reflection coefficient as:

$$R(\theta_{specular}) = \max\left(1, \frac{\Delta\alpha}{\Delta\theta_{mach}}\right) \int_{-\frac{\Delta\theta_{mach}}{2}}^{\frac{\Delta\theta_{mach}}{2}} \cos(\alpha) P(\alpha) R_0(\theta_{specular} - \alpha) d\alpha$$

Equation 5.27

In this section we calculated the reflection coefficient from a rough surface. We demonstrate that in the case of speculary reflected beam the reflection coefficient can be expressed by equation 5.27. However, we must keep in mind that this expression is valid in the limit where we can cut the surface to a series of independent regions of dimension l^2.

An angular divergence not equal to zero introduces an uncertainty over the reflectivity as a function of momentum transfer, Q, defined as $Q=4\pi\sin(\theta)/\lambda$, where θ is the angle between the incoming beam and the flat surface. The introduced broadening changes the signal amplitude and broadens sharp features in the reflection profile. In

particular, the total reflection edge in the reflectivity profile is transformed from a sharp change to a rounded one.

It is well known that adsorption has a similar effect on the shape of the total reflection edge for X-rays [4]. However, we consider here only the reflection of X-rays or neutrons from soft condensed matter, where the adsorption cross-section is very small (in order of 10^{-11}) and can be neglected. Hence, we will demonstrate that it is possible in principle to determine the angular divergence, including instrumental and surface effects, by studying the shape of the reflectivity profile near the total reflection edge. Figure 5.8 shows the simulated data from a textured silicon/air interface, where we assumed that the angular divergence α follows Gaussian statistics. It can be seen, that increasing the angular divergence produces a rounding of the total reflection feature.

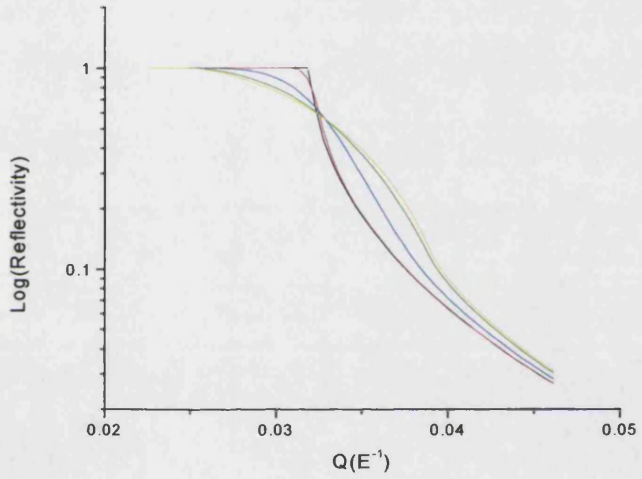

Figure 5.8 Suite of reflectivity profiles for different value of $<\alpha^2>$ from a silicon/air interface (Black: $<\alpha^2>=0$, Red: $<\alpha^2>=0.01$, Blue: $<\alpha^2>=0.05$, Green $<\alpha^2>=0.1$, Yellow: $<\alpha^2>=0.15$) The value of the instrumental angular acceptance is set to 0.3°.

5.4.3) Relation between the projection angle α and the surface profile.

In this section we demonstrate the relation between the projection angle α and the surface profile. We will show that the angle α can be considered as the difference between the angle of specular reflection from the flat surface and the angle of specular reflection from the real surface. We will apply the obtained result to a slowly varying surface profile with large lateral correlation length. Before any consideration, we must

keep in mind that we assume that we can use the law of geometrical optics. Therefore, the direction of the propagation of the electromagnetic energy can be represented by a line (*light ray*)[1], and the size of the scattering object is large compared with the wavelength of the incoming beam. In this case we can consider the surface to be locally plane and flat (i.e. we can approximate the surface locally by its tangent).
Figure 5.9 represents the configuration that we consider in order to describe the scattering from a rough surface.

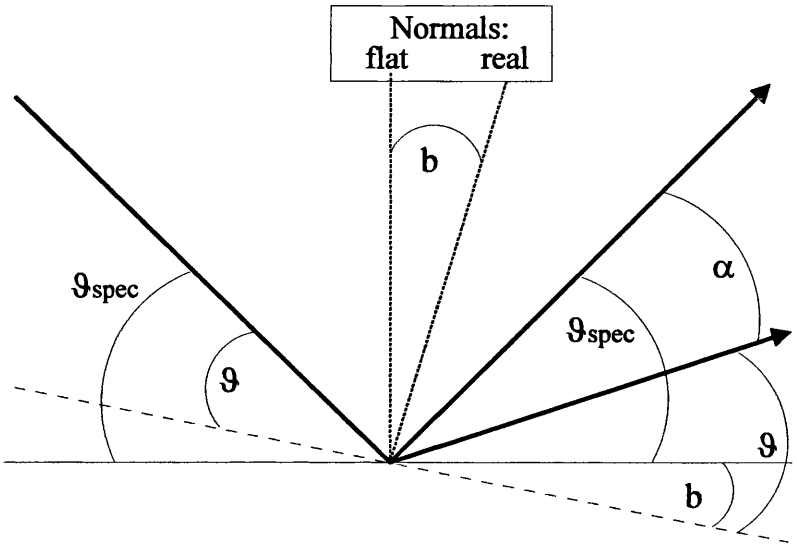

Figure 5.9 Schematic representation of the surface of a rough sample. The projection angle α is linked to the angle, b, between the normal to the real surface and the normal to the ideally flat surface. We suppose that the surface is illuminated with an incoming beam of incident angle θspec with the flat surface and θ with the real surface. Only specular reflection is considered here.

First we calculate the angle *b*, between the normal to the flat surface and to the real surface as a function of the two scattering angles θ and $\theta_{specular}$. We can write the following angular relations:

$$b = \theta_{specular} - \theta$$

Equation 5.28

and

$$\alpha + \theta = \theta_{specular} + b$$

Equation 5.29

therefore

$$\alpha = b + \theta_{specular} - \theta$$

Equation 5.30

Therefore, by introducing equation.5.28 into the equation.5.30 we finally express the angle α as a twice the value of the angle b:

$$\alpha = 2b$$

Equation 5.31

This relation links the *angular divergence* of the reflected beam to the angle between the local normal to the real surface and the normal to the ideally flat surface. Therefore, the angle of projection α measures the *angular divergence* of the reflected beam. It is clear that the reflected beam becomes more divergent as the dimension of the surface roughness increase. In other words as the dimensions of the surface roughness increase the angle α can take a larger number of values, and the distribution function $P(\alpha)$ becomes wider.

The distribution function $P(\alpha)$ is linked to the degree of roughness of the surface. But this would still not provide adequate information about the distribution function $P(\alpha)$. In order to define $P(\alpha)$ it is necessary to calculate its first statistical moment (average value) and the second statistical moment (variance).

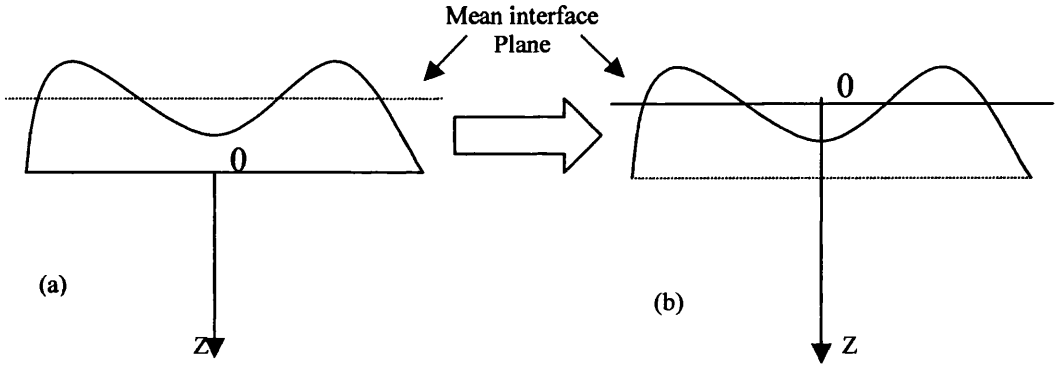

Figure 5.10. The figure on the right hand side represents the rough surface (the plane curved line) and the dashed line represents the mean interface plane and the reference plane is considered as the base line of the rough surface. The figure in the left-hand side represents the same surface but the reference plane is the mean interface plane.

If we consider the average plane of the rough interface as the origin plane (Figure 5.10), then we do not change the scattering properties of the surface [7] if we take into account the change of the sign for the part of the surface which is under the mean plane. In this case, by averaging the variation of the surface profile, *u(r)*, over the surface we find that this average value is equal to zero (because there are as many parts of the surface above and under the reference plane) [1]. Therefore, the mean angular divergence of the scattered beam from the surface is equal to zero (because the mean curvature of the surface is equal to zero). Hence, we can write for the first statistical momentum of *P(α)*:

$$\langle \alpha \rangle = \langle b \rangle = 0$$

Equation 5.32

to calculate the second statistical moment of the distribution *P(α)*, we firstly consider the variation in the direction of the local normal to the surface, and consider the reference direction to be the direction of the normal to the flat surface. Let *n(r)* denote the normal to the surface at the point *r*, and n_0 the normal to the flat surface (Figure 5.11)

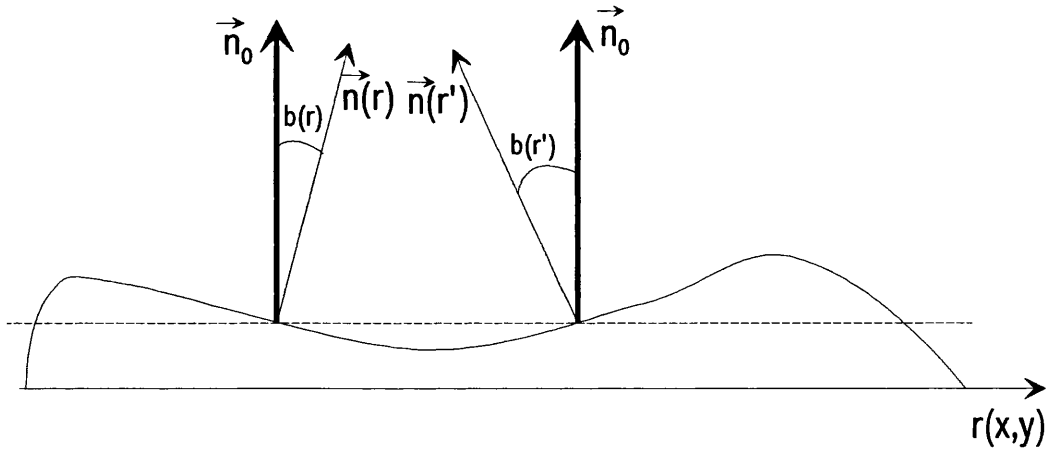

Figure 5.11 We consider two points at the surface r and r'. The direction of the local normal to the surface depends on the in-plane coordinate r and the surface orientation. Therefore the value of the angle between the normal to the flat surface n_0 and the normal at point r depends also on the spatial coordinate r and the local direction of the surface. The vector difference between the two local normal give an insight into the variation of the local surface direction, and the degree of roughness of the surface.

The first idea to characterize the changes in local surface direction is to use the average value of the difference between directions of the local normal at two distinct

points of the surface. Figure 5.11 shows a schematic representation of the situation that we consider. Let ***n(r)*** be the local normal vector at point of in-plane coordinate *r* and ***n(r')*** the local normal vector at point of in-plane coordinate *r'*. The average of the difference between these two normals over the surface vanishes as a result of the fact that the mean curvature of the surface is equal to zero. Thus we must resort to higher order in statistical moment for this difference. The first statistical moment giving a non-trivial answer is the variance of the difference, which is defined as:

$$G(r,r') = \left\langle (\vec{n}(r) - \vec{n}(r'))^2 \right\rangle_{surface} = \left\langle (\delta\vec{n}(r) - \delta\vec{n}(r'))^2 \right\rangle_{surface} = 2\left\langle \delta\vec{n}(r)^2 \right\rangle_{surface} - 2\left\langle \delta\vec{n}(r)\delta\vec{n}(r') \right\rangle_{surface}$$

Equation 5.33

with

$$\delta\vec{n}(r) = \vec{n}(r) - \vec{n}_0$$

Equation 5.34

As the direction of the normal to the flat interface is chosen to be the reference direction, we would rather consider the changes in the value of the expression 5.34 as a function of the in-plane coordinate than the changes in the local normal direction. Equation 5.33 measures the degree of dependence between the normal to the surface at two different points. This quantity depends only on the distance, $r''=|r-r'|$, which separates these two points, and is commonly called the *pair correlation function.*

As we can notice the function *G(r, r')* can be written as the difference between the average value of the norm of δn, and the average of the projection of the quantity δn at point *r* over the quantity δn at point *r'*. The average of the projection is called *correlation function* and denoted $C(r, r')^{\sim}$. Now we wish to expand the correlation function and express it clearly as a function of the angle *b(r)*. This function is defined as a vector product between the normal at point *r* and *r'* to the surface. From figure 5.11 it is easy to notice that the angle between these two quantities is equal to the difference between the angle *b(r)* and *b(r')*. Therefore, we can write the correlation function as:

$$C(r,r') = \left\langle \left|\delta\vec{n}(r)\right\| \delta\vec{n}(r')\left| \cos(b(r) - b(r')) \right\rangle_{surface} \right.$$

Equation 5.35

At this stage of our demonstration, we consider that the magnitude of the quantity δn is independent of the cosine term. Therefore we can write the correlation function as:

$$\frac{C(r,r')}{\left\langle \delta\vec{n}^2(r)\right\rangle} = \left\langle \cos(b(r)-b(r'))\right\rangle_{surface}$$

Equation 5.36

By using the addition formula for cosine and by noticing that the sine term is odd we can simplify equation 5.36 to:

$$\frac{C(r,r')}{\left\langle \delta\vec{n}^2(r)\right\rangle} = \left\langle \cos(b(r))\cos(b(r'))\right\rangle_{surface}$$

Equation 5.37

At this point of this derivation we use for the first time the assumption that the surface profile is varying slowly. This assumption means that the changes of the local surface orientation are small compared to the flat surface. This assumption is the key hypothesis of this development because it assumes that the surface keeps the same orientation over a distance larger than the wavelength of the incoming beam. If $b(|r-r'|)$ is defined over a characteristic distance ξ that we call the lateral correlation length of the surface, we can consider the angle b to be small (since the changes of the local surface orientation are small compared to the flat surface), and approximate equation 5.37 to second order as:

$$\frac{C(r,r')}{\left\langle \delta\vec{n}^2(r)\right\rangle} \approx 1-\left\langle b\left(|r-r'|\right)^2\right\rangle_{surface} + O\left(\left\langle b(|r-r'|)^2\right\rangle_{surface}\right)$$

Equation 5.38

Where the term $O(\langle b(r-r')^2\rangle)$ represents all the components of the correlation function which are at the higher degree than $\langle b^2\rangle$. By using equation 5.31 and the *ergodic hypothesis* we can finally write the variance of the divergence angle α as:

$$\left\langle \alpha(r)^2\right\rangle_{surface} = 4\left\langle b(r)^2\right\rangle_{surface} = 4(1-\frac{C(r,r')}{\left\langle \delta\vec{n}^2(r)\right\rangle})$$

Equation 5.39

In this paragraph we calculated the first and the second moment of the distribution $P(\alpha)$. However, what we measure from the reflectivity data is the angular average of the divergence of the reflected beam per source, therefore equation 5.39 can be written as:

$$\left\langle \alpha(r)^2 \right\rangle_{angular} = \frac{4l^2}{S}\left(1 - \frac{C(r,r')}{\left\langle \delta\vec{n}^2(r) \right\rangle}\right)$$

Equation 5.40

Equation 5.39 links directly the variance of the divergence angle α to the degree of roughness of the surface. If the surface is perfectly flat the correlation function $C(r)$ is equal to one (because the entire local normal has the same orientation as the normal to the flat surface). Therefore the variance of the variable α is equal to zero. Conversely, if the surface is very rough, the correlation function $C(r)$ is equal to zero, hence the variance of the variable α become very large.

5.4.4) Choice of the distribution function

In the last section we calculated the first and the second statistical momentum of the distribution function $P(\alpha)$. We demonstrated that these values depend on the statistics of the rough surface. Figure 5.5. represents the general shape of $P(\alpha)$. Few known distributions function (Gaussian distribution, Lorentzien distribution, Bessel function....) present the same general behaviour as that represented in figure 5.5.

As we noticed in the second section, one can reduce the surface to a series of independent sources. We supposed that each source radiates in a direction, which is independent of the radiation direction of its neighbour. Therefore, we can assume that α is distributed randomly over the range defined by the direction of radiation of the sources. Since the number of these sources is very big (10^6-10^8) α is distributed over a quasi-infinite number of possible values. This picture satisfies the conditions for the *central limit theorem* [16]. Assuming the hypothesis that α can takes a large number of possible values, $P(\alpha)$ can be considered as a *normal* or *Gaussian* distribution of the standard form:

$$P(\alpha) = \frac{1}{\sqrt{2\pi\langle\alpha^2\rangle}} e^{\frac{\alpha^2}{2\langle\alpha^2\rangle}}$$

Equation 5.41

The advantage of considering *P(α)* as a Gaussian is simplicity. It is clear that one could consider other form of distribution function for the angular divergence α, however, in the asymptotic limit (when the number of terms in the range that α is distributed becomes quasi-infinite) according to the *central limit theorem* all the distributions are approximated by a normal distribution. In the following sections we consider that the surface of the sample is very large compared to the characteristic dimension l^2, and we consider *P(α)* as a normal distribution

Figure 5.12 shows the behaviour of this distribution function as its variance increases. We notice that the amplitude of the function decreases as the value of the variance increases, and the function is centred at α=0.

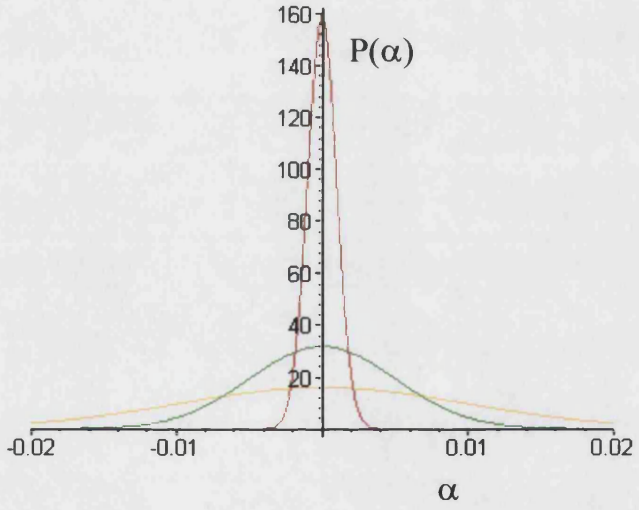

Figure 5.12 Variation of the function P(α) as a function of the variance $<\alpha^2>$. The red curve represents the function for a variance equal to 0.001, the green one for a variance equal to 0.05 and the yellow one for a variance equal to 0.01. We notice that as the value of the variance increase the value height of the function decreases.

The value of the parameter $<\alpha^2>$ depends on the degree of roughness of the surface. If the surface is perfectly flat the value of $<\alpha^2>$ is very small and therefore P(α) is very peaked around the position α equal to zero. This means that all the sources radiate in the direction of observation. But if the surface is very rough the value of $<\alpha^2>$

increases, and the amplitude of the distribution function decreases. In other word, the range of angle over which α is distributed become wider, and all the sources don't radiate in the direction of observation, therefore the observed intensity must be smaller than the one from the flat surface.

If we assume the shape of the distribution function for the angular divergence, α, is known we can recalculate the value of $<\alpha^2>$ in the general case. The starting point of our derivation is equation 5.37. As we notice before, the *ergodic hypothesis* rules over the statistical properties of this system. Therefore, we can change the averaging process over the surface to the averaging process over the angular distribution. The angle b(r) and α(r) are linearly dependent (equation 5.31) therefore the distribution function for the variable b must follow the same distribution law as the variable α. According to these considerations we write equation 5.37 as:

$$C(r'') \approx \left(\int_{angular} \cos(b) \frac{1}{\sqrt{2\pi \langle b^2 \rangle}} e^{\frac{b^2}{2\langle b^2 \rangle}} db \right)^2$$

Equation 5.42

The cosine term can be expanded to a sum of two complex exponential terms, and by integrating them we find:

$$C(r'') \approx e^{-\langle b^2 \rangle}$$

Equation 5.43

This expression is valid if the local normal is normalised. In the general case, where we suppose that the norm of local normal is independent of cosine term, the parameter $<b^2>$ is expressed as:

$$\langle b^2 \rangle_{surface} \approx -\ln\left(\frac{C(r'')}{\langle \delta\vec{n}(r'')^2 \rangle_{surface}}\right)$$

Equation 5.44

By introducing equation 5.31 into equation 5.44 we find finally the general relation between the variance of the angular divergence and surface roughness:

$$\langle \alpha^2 \rangle_{surface} \approx -4\ln\left(\frac{C(r'')}{\langle \delta\tilde{n}(r'')^2 \rangle_{surface}}\right)$$

Equation 5.45

Equation 5.45 is the key relation of this work. As we can see, it links the variation of angular divergence of the reflected beam to the degree of roughness of the surface, through the correlation function C(r"). However, at this stage of our development we re-write equation 5.45 as the function of the pair correlation function G(r"), in order to derive equation 5.40 from equation 5.45. We introduce equation 5.33 into equation 5.45:

$$\langle \alpha^2 \rangle_{surface} \approx -4Ln\left(1-\frac{G(r'')}{2\langle \delta\tilde{n}(r'')^2 \rangle}\right)$$

Equation 5.46

We assume that the changes in the local normal direction is small, hence the variation of the pair correlation function is small along the surface of the sample. In this case the quantity $G(r")/(2<\delta n(r")^2>)$ is small compared to one. Therefore we can approximate equation 5.46 to the first order as:

$$\langle \alpha^2 \rangle_{surface} \approx 2\frac{G(r'')}{\langle \delta\tilde{n}(r'')^2 \rangle} = 4\left(1-\frac{C(r'')}{\langle \delta\tilde{n}(r'')^2 \rangle}\right)$$

Equation 5.47

Which is the same expression as equation 5.33.

5.4.5) Definition of the dimension l^2 [1]

In the last section in order to calculate the reflected intensity from a rough surface we demonstrated that it is possible to cut the surface to a series of n independent sources each of dimension l^2. In this section we initially justify this argument and secondly identify the dimension l^2 as the *in plane coherence length* of the incoming beam.

Consider a collimated incoherent source with a radiating surface of dimension S. The source is assumed to have a uniform distribution of intensity at its surface, therefore the intensity, I_0, emitted by the source is independent of the position on the radiating

surface. The source is positioned at a distance R far from the surface D that it illuminates (Figure 5.13).

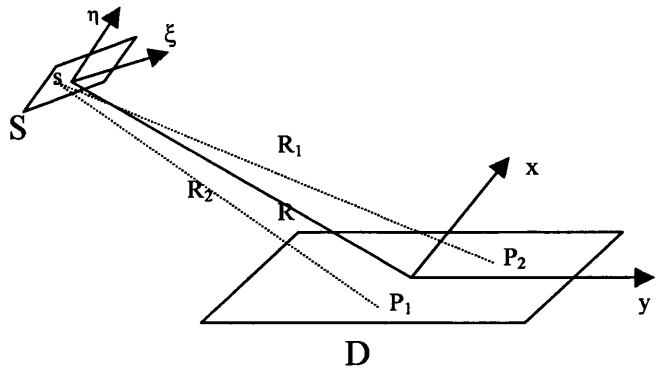

Figure 5.13 Illustrating the situation where a source of dimension S illuminates a surface D.

The task is to find the relationship between the change of the intensity at point P_1 and P_2 on the surface D. In order to calculate the relation between the intensity at these two points we use Van Cittert-Zernike theorem [1]. This theorem determines the correlation between the intensity at two distinct points of an illuminated surface. In the case of a uniform source illuminating a surface we find that the correlation between intensity at the points P_1 and P_2 is given by the norm of the *mutual intensity* $J(P_1,P_2)$:

$$J(P_1,P_2) = I_0 \int_S \frac{e^{ik(R_1-R_2)}}{R_1 R_2} ds$$

Equation 5.48

Where I_0 is the intensity of the incoming beam and k is the wave number in the medium.

Let (ξ,η) be the coordinates of the point s positioned at the surface of the source, referred to source's axes, and (X_1,Y_1) and (X_2,Y_2) the coordinates of points P_1 and P_2 respectively, referred to surface's axes (Figure 5.13). R is the distance between the source and the surface. The plane of the surface makes an angle θ with the direction of propagation of the incident beam. In this case we can calculate the distance R_1:

$$R_1^2 = (X_1 - \xi\sin(\theta))^2 + (Y_1 - \eta\sin(\theta))^2 + R^2$$

Equation 5.49

Here we consider that the distance R between the surface and the source is much bigger than the dimension of the source. In this case we can approximate the distance R_1 as:

$$R_1 \approx R + \frac{(X_1 - \xi\sin(\theta))^2 + (Y_1 - \eta\sin(\theta))^2}{2R}$$

Equation 5.50

A strictly similar expression can be obtained for R_2:

$$R_2 \approx R + \frac{(X_2 - \xi\sin(\theta))^2 + (Y_2 - \eta\sin(\theta))^2}{2R}$$

Equation 5.51

so that

$$R_1 - R_2 \approx \frac{(X_1^2 + Y_1^2) - (X_2^2 + Y_2^2)}{2R} - \frac{(X_1 - X_2)\xi + (Y_1 - Y_2)\eta}{R}\sin(\theta)$$

Equation 5.52

Here only the leading terms in X_1/R, Y_1/R, ξ/R and η/R have been retained. In the denominator of equation 5.48, R_1 and R_2 may to a good approximation (first order) be replaced by R. For simplicity we also set:

$$p = \frac{(X_1 - X_2)}{R} \qquad q = \frac{(Y_1 - Y_2)}{R}$$

Equation 5.53

$$\psi = \frac{K\left[(X_1^2 + Y_1^2) - (X_2^2 + Y_2^2)\right]}{2R}$$

Equation 5.54

Then equation 5.48 is reduced to:

$$J(P_1, P_2) = \frac{I_0 e^{i\psi}\sin^2(\theta)}{R^2}\int_S e^{-ik(p\xi + q\eta)\sin(\theta)} d\xi d\eta$$

Equation 5.55

This equation expresses the correlation between the intensity at point P_1 and the intensity at a point P_2 situated at a distance l far from P_1. From equation 5.54 it is clear that when the distance l is smaller than the wavelength of the incoming beam we can neglect the term due to the phase difference (the exponential containing the variable ψ) between the incident beam at point P_1 and at the point P_2.

At this stage of the calculation, we consider that the source has a rectangular shape (the shape of a slit) (figure 5.14).

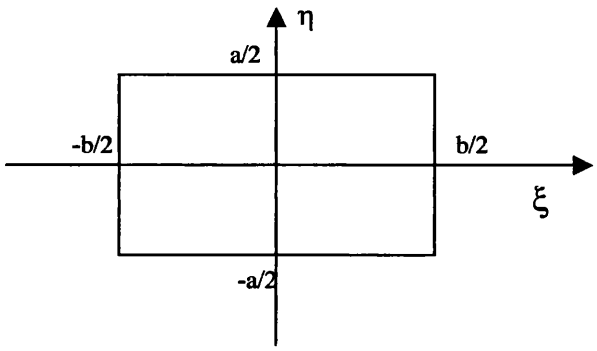

Figure 5.14 Illustration of a uniform rectangular source with dimension a*b

In this case we can easily find an analytical expression for equation 5.55, by integrating over the surface of the source:

$$J(P_1,P_2) = e^{i\psi}\frac{abI_0\sin^2(\theta)}{R^2}H(x)H(y)$$

Equation 5.56

Where the variables x and y are:

$$x = kp\sin(\theta)\frac{b}{2}$$

$$y = kq\sin(\theta)\frac{a}{2}$$

Equation 5.57

And the function H(i) is :

$$H(i) = \frac{\sin(i)}{i}$$

Equation 5.58

Figure5.15 illustrates the behaviour of this function. It decreases from the value unity to zero when i=3.2

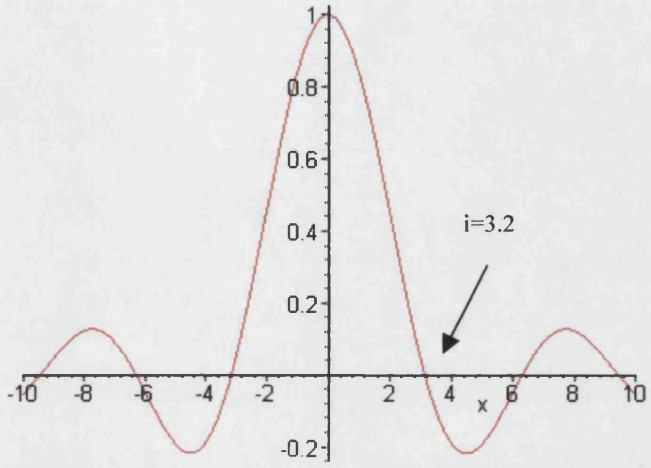

Figure 5.15. Variation of the function H(x) as a function of x.

Therefore equation 5.56 is equal to zero when x=3.2 or y=3.2. As we said before, the norm of equation 5.56 expresses the correlation between the intensity at points P_1 and P_2. When correlation between intensities is equal to zero the intensities between these points is no longer correlated. The shape of the function H(i) shows that as the point P_1 and P_2 are increasingly separated the degree of correlation between the intensities decreases steadily and there is a complete independence between the intensity at these points when x=3.2 and y=3.2. In other words, when P_1 and P_2 are separated by the distance:

$$l_{coh} = P_1P_2 = \sqrt{(X_1 - X_2)^2 + (Y_1 - Y_2)^2} = \frac{6.4R}{k\sin(\theta)}\sqrt{\frac{1}{a^2} + \frac{1}{b^2}}$$

Equation 5.59

In a physical sense, this means that intensities at two points on the surface separated by a distance equal to l_{coh} are completely independent. Therefore, the disturbances of electromagnetic fields at these points are also independent.

We used the fact that in a reflection arrangement, the surface can be considered as a series of dipoles [3] (in the case of X-rays). We cut the surface to a series of independent sources of dimension l^2. In fact each source can be seen as a series of correlated dipoles (coherent source) [1]. Therefore, as these dipoles radiate under the influence of the incoming electromagnetic field the region over which they are correlated is the area of the surface over which the electromagnetic field is correlated. In other words, l_{coh} is the linear dimension for each source. Hence, it is possible to cut the surface to a series of coherent sources with a linear dimension equal to l_{coh}.
l_{coh} is called the *in plane coherence length* of the incoming beam . However, as we can see in equation 5.56 the coherence length in X and Y direction are different and independent in the case of a rectangular source. In this specific case we define the *coherence surface*, l^2, as:

$$l^2 = (X_1 - X_2) * (Y_1 - Y_2) = \frac{40.96R^2}{k^2 \sin^2(\theta)} \frac{1}{ab}$$

Equation 5.60

This dimension corresponds to the dimension l^2 of each source.
As an example, consider that the wavelength of the incident beam is equal to 4.75Å and the distance between the source and the surface is equal to 13cm and the angle of incidence is equal to 0.04°. The dimension of the source is given by a=50μm and b=1cm, therefore the size of the coherence surface is $l^2=16.23*10^{-7}cm^2$. Hence, for a surface of dimension 5 cm^2 the number of sources is $3*10^6$.

5.4.6) Analogy with scaling and renormalization of critical phenomena

In the last section we have demonstrate the possibility to use the variation of the direction of the local normals in order to calculate the specular reflectivity profile from a rough surface. We assumed that the surface profile variations are slow and the surface can be represented by a smooth and continuous function. We showed that the degree of roughness of the surface is linked to the variation of the direction of the local normal. We also derived equation 5.45 which links the variation of the local normal direction to the divergence of the reflected beam through the function $S(r")=C(r")/\langle n^2 \rangle$.

For a perfectly flat surface this function is equal to one but for a rough surface the value of S(r") decreases continuously from unity to zero. Therefore one can consider this function as a probe of the surface roughening process. However, in our demonstration we considered the dimension of each unit area of the surface equal to the dimension of the coherence area of the incoming beam, l^2_{coh}, hence the function S(r") is a "macroscopic" parameter which measures the correlation between these domains. At this point of our work we encounter a problem: generally the problem of scattering from rough surfaces is formulated by considering the in plane correlation length of the surface smaller than the coherence length of the incoming beam and the effect of the roughness is treated as a "microscopic " quantity [8]. In our derivation we assume that the in-plane correlation length is larger than the coherence length. By introducing this point we have to answer the question: What is the relation between the function S(r") and the microscopic configuration of the system?

To answer to this question we use an analogy between a two dimensional Ising system [16] and a system where each points of the lattice is occupied by a local normal vector. This analogy allows us to express the relationship between the function S(r") and the "microscopic" configuration of the surface and also clarifies the relationship between the in-plane coherence length and the correlation length.

5.4.6.1) Lattice picture of a surface

For simplicity reasons let us consider a one-dimensional rough interface (figure 5.16)

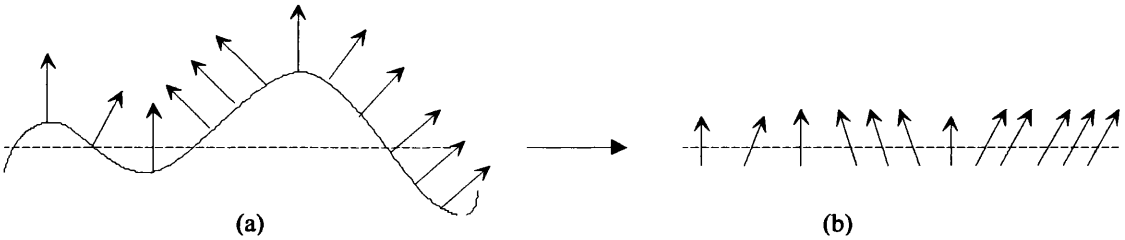

Figure 5.16 The schematic representation of the transformation of a rough interface (a) to an one dimensional Ising model (b). The arrows represent the local normal direction to the interface.

As we described before, in the limit where the dimension of the radiating object is bigger than the wavelength of the incoming beam, we can describe the reflection law by the direction of the local normals to the surface. Figure 5.16.a represents an one-dimensional rough interface with its local normals. By using equation 5.27 to calculate the reflection coefficient from a rough interface, we are no longer interested

in the shape of the surface profile, but only on the direction of the local normals. Therefore one can represent the rough interface only by the direction of its local normals (Figure 5.16.b). In this picture all the properties of the interface (periodicity, correlation length) can be expressed by the *"interactions"* between these normals. This picture allows us to make the analogy between the reflection from a rough surface and the Ising model.

The function S(r"), measures the correlation between the directions of these normals. This function acts exactly in the same way as the correlation function in a disordered system [16]. In order to describe the degree of roughness of the surface, we need to study the behaviour of the function S(r") as a function of distance r" between the sites of the lattice.

The structure of the surface can be described by the self-affine geometry [2, 17]. Therefore, the height-height correlation function is given by [18]:

$$\Gamma(r) = \sigma^2 e^{-\left(\frac{r''}{\xi}\right)^{2h}}$$

Equation 5.61

Where the exponent h describes how rough the surface is [18]. This exponent is a positive real value smaller than 1. Small values of h produce extremely rough surfaces, however, as h approaches 1 the surface appears to have smooth valleys and hills [18]. Following Ogilvy's calculations [19], in the case of a slowly changing surface profile, the correlation function between the normals to the surface is proportional to the second derivative of the height-height correlation function, therefore

$$S(r'') = \left[1 - 2\frac{h}{2h-1}\left(\frac{r''}{\xi}\right)^{2h}\right] e^{-\left(\frac{r''}{\xi}\right)^{2h}}$$

Equation 5.62

And the rms value of the normals to the surface is equal to:

$$\left\langle n(r)^2 \right\rangle = 2h\frac{\sigma^2}{\xi^2}(2h-1)\left(\frac{r}{\xi}\right)^{2h-2}$$

Equation 5.63

In the case of h = 1, we recover the height-height correlation function and the RMS local normals value in the case of a Gaussian surface [19].

Equation 5.62 defines the general formula for the function S(r"). As this function measures the degree of correlation between local normals its values should be positive and smaller, or equal to, one. As we showed in section 5.4.5, the coherence length corresponds to the minimal distance necessary to distinguish two points on the surface. Therefore we can define the following inequality:

$$1-\frac{2h}{2h-1}\left(\frac{l}{\xi}\right)^{2h} \geq 0$$

Equation 5.64

This inequality lets us define the domain of validity of the developed theory.

$$0 \leq l \leq \xi\left(\frac{2h-1}{2h}\right)^{\frac{1}{2h}}$$

Equation 5.65

Therefore we find that theory is valid only if the coherence length is smaller than the correlation length and if 0.5 < h < 1. The constraint in h means that the developed theory is only valid in the case of a smoothly changing surface.

The behaviour of the correlation length, ξ, as a function of the dynamic parameters of the system (time, temperature, magnetic field..) is thus a description of the variation of "randomness" in the system. If the directions of the local normals are correlated strongly and over a large distance (long range interaction limit) the correlation length ξ becomes infinite and the function S(r") becomes equal to one. In the case of a perfectly flat surface the correlation length is infinite and the exponent h is equal to 1. However in the case of a very rough surface the correlation length tends to zero therefore the function S(r") is equal to zero. If we look carefully to the behaviour of S(r") we notice that this function defines the state of the surface, *i.e.* how rough the surface is, hence we consider this function as an "*order parameter*".

Figure 5.17 shows the behaviour of the function S(r") for different values of the correlation length and the dimension parameter h.

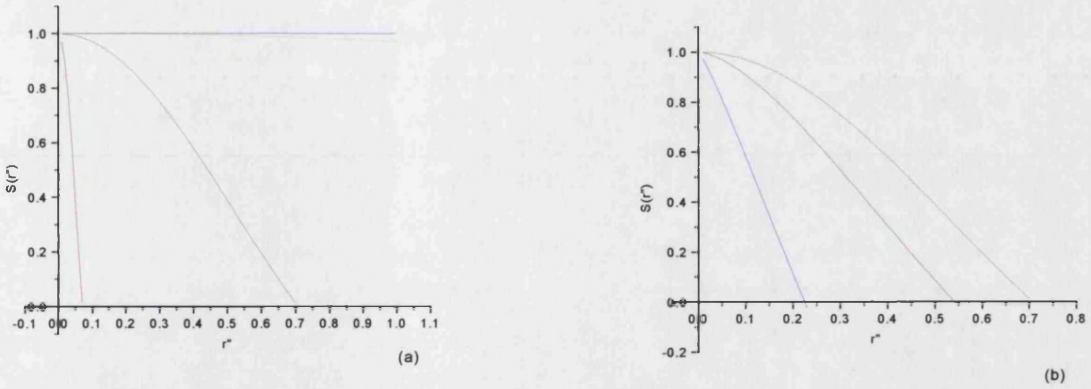

Figure 5.17. Behaviour of the order parameter as a function of the distance. (**a**) The dimension parameter h is fixed to 1 and the correlation length changes as: 0.1 (red), 1 (green), 10 (yellow), 100 (blue). (**b**) The correlation length is fixed to 1 and the dimension parameter h changes as: 0.6 (blue), 0.8 (red), 1 (green).

In this section we have shown the possible analogy between the Ising model and the method that we proposed. We identified the function S(r") as the order parameter and showed that its behaviour could be described by the equation 5.62. By using this equation we defined the domain of validity of the developed theory: the coherence length is smaller than the correlation length and the surface profile varies slowly. In the next section we introduce the notion of the scale invariance of we describe how to link the coherence length l to the correlation length ξ.

5.4.6.2) Scale invariance

As we said, it is possible to cut the surface to a series of cells of dimension l^2 (figure 5.18)

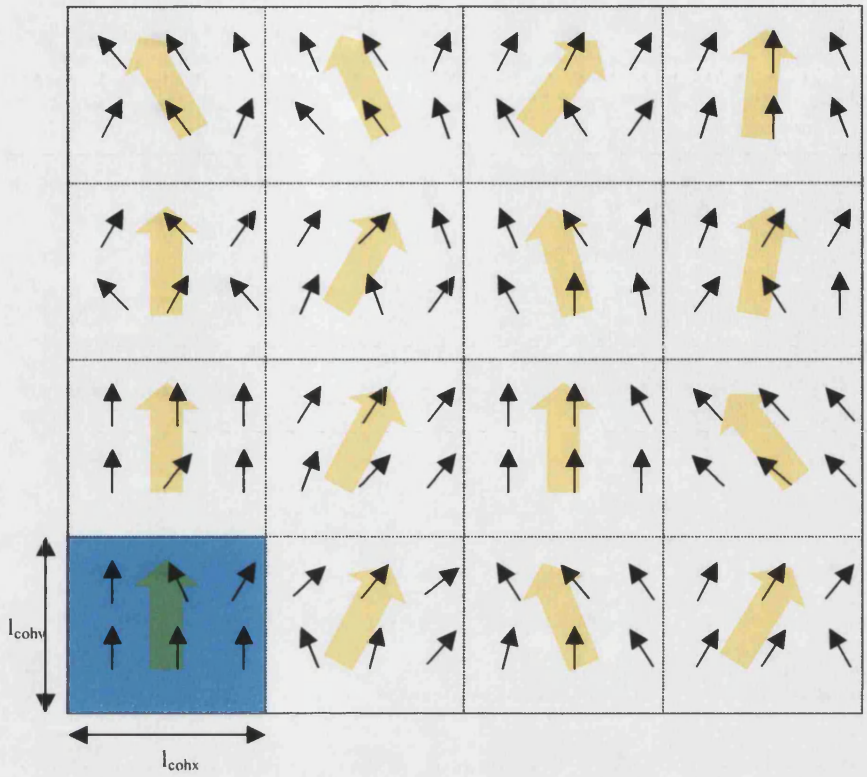

Figure 5.18 Schematic representation of a rough surface by the Ising model lattice. The surface is cut into a series of cell of dimension l^2. The yellow arrows represent the average direction of each cell.

Each cell represents one independent source of dimension l^2, and has an average orientation, which depends on the microscopic internal orientation of each block. If the correlation length ξ is large, i.e. the correlation between the directions of local normals is strong, then we can consider that the directions of local normals in each block are strongly correlated. In other words, inside a block of dimension l^2, where $l << \xi$, all the normals are so nearly aligned that they tend to behave as a single unit. Therefore we can ignore the internal structure of each block and think of the rough surface as a collective phenomenon of an assembly of blocks, interacting via long-range correlation.

Suppose that in our original model the order parameter S(r") contains only nearest neighbour interaction (variation of direction of the local normals between two adjacent points on the surface). Therefore, the order parameter for block i can be expressed by the averaged of the product of two normal neighbours:

$$\widetilde{S}_i(r'') \propto \frac{\sum_{l,m} \vec{n}_l . \vec{n}_m}{l^2}$$

Equation 5.66

It is clear from equation 5.66 that, the order parameter S(r") has the same functional form over the whole surface or over a block. In this case we can write the order parameter over the sample as a function of the order parameter over a block by multiplying the last expression by l^2:

$$S(r'') \propto l^2 * \widetilde{S}(r'')$$

Equation 5.67

This result shows the scale invariance of the order parameter. The order parameter defined over a block of dimension l^2 has the same behaviour as the order parameter over the whole surface. This result can be obtained also by considering the self-affine properties of the surface [2, 17, 20].

However, this result would be inconsistent if the condition $l << \xi$ is not satisfied. physically grounds this means that if the interaction between the directions of the local normals is short range (the range of interaction is smaller than the size of the block), then by averaging the variation of the normal direction over a block, we consider all the configurations and the average value would give us the same direction as the normal to the flat surface. On the contrary, if the interactions between the normal direction are long range, averaging over the dimension of a block considers only the a fraction of the configuration that the normal direction can accept, hence the direction of the normal is imposed by the range of the interaction.

In this section we demonstrated the scale invariance of the behaviour of the order parameter. We showed that the order parameter follows a *scaling law* [13]. The formal analogy between the results describes in this section and the thermodynamic theory of the *critical phenomena* is very strong [16]. This is the reason why in the next section we consider the case where the value of the correlation length varies as a function of a dynamic parameter (time, temperature, magnetic field, electric field...) and we will show how this variation can be measured by the divergence of the reflected beam. In other words we propose a new view on the roughening transition of a flat surface.

5.4.6.3) Attempt at a dynamic view: the kinetics of a roughening process.

By definition a roughening process transforms a flat surface to a rough surface. The kinetics of this process is generally described by a non-linear diffusion equation (Burges equation, KPZ) [2]. The common feature in all these equations is the change in the length of the correlation length. This picture become evident when one describes a surface by the direction of its local normals.

Before the roughening process began the surface is perfectly flat, therefore all the normals are perfectly aligned (figure 5.19). In other words the correlation length is very large.

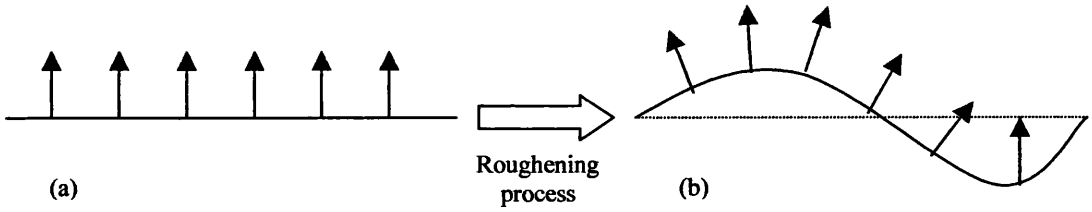

Figure 5.19. The roughening transition of a flat surface (**a**) to low frequency rough surface (**b**)

However, as the roughening process begins the local normals are not aligned any more. Therefore, the dimension of the correlation length decreases.

The change in the dimension of the correlation length strongly affects the divergence of the reflected beam. To explicitly define the relationship between the correlation length and the angular divergence of the reflected beam through the order parameter, we use the definition of the correlation function and equation 5.34.

$$\left\langle \delta\vec{n}(r)\delta\vec{n}(r')\right\rangle_{surface} = \left\langle \vec{n}(r).\vec{n}(r')\right\rangle_{surface} + 1 \qquad \text{(a)}$$

$$\left\langle \delta\vec{n}(r)^2\right\rangle = \left\langle \vec{n}(r)^2\right\rangle_{surface} + 1 \qquad \text{(b)}$$

Equation 5.68

The first term in the right hand side of the equation 5.68.a (the local normals correlation function) corresponds to $< n^2 > \times S(r")$. By introducing equations 5.62 ,5.61 and 5.68 into the equation 5.45 we can express clearly the behaviour of the divergence of the reflected beam as a function of the correlation length ξ:

$$\left\langle \alpha^2 \right\rangle_{surface} = -4\ln\left(\frac{1+\left\langle \vec{n}^2 \right\rangle S(r)}{1+\left\langle \vec{n}^2 \right\rangle} \right)$$

Equation 5.69

Now we wish to study the kinetics of the roughening process. We assume that the correlation length ξ, and therefore the order parameter, is a function of time and the external field h, which induces the roughening transition of the surface; this field can be time dependent. As the roughness of the surface increases the dimension of the correlation length diminishes, the value of the order parameter approaches zero and the divergence of the reflected beam become lager. This result is valid in the limit of $l < \xi$.

Figure 5.20.a represents the simulated reflectivity profile in the region of total reflection for X-rays from the surface of water (scattering length density: 9.475×10^{-6} $Å^{-2}$) for different values of the order parameter, S(r").

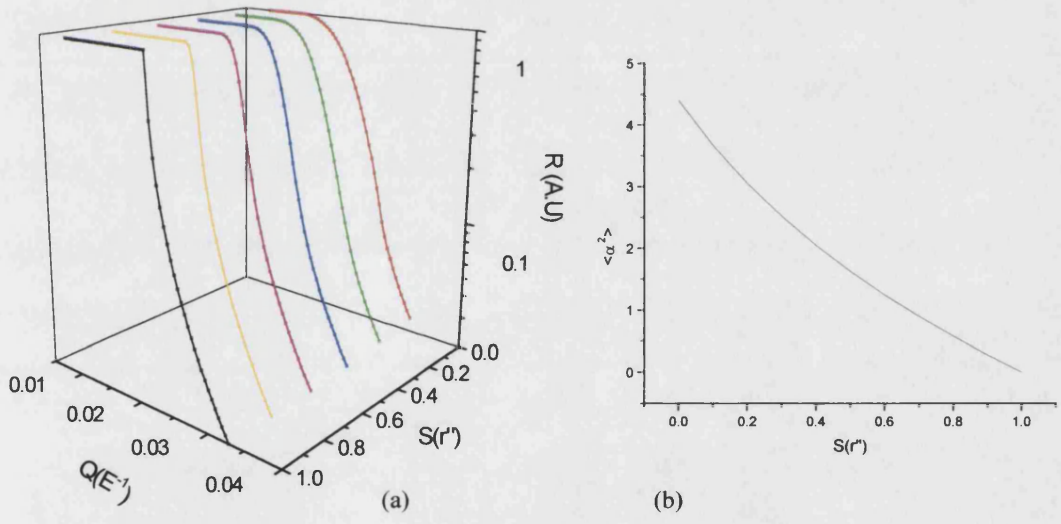

Figure 5.20. (a) Simulated X-ray reflectivity profile near the total reflection region from the surface of water for different values of the order parameter. **(b)** Variation of the angular divergence as a function of the order parameter.

Figure 5.20.b shows the variation of the angular divergence as a function of the order parameter. As the roughness of the surface become important (the value of the order parameter approach to zero) the rounding of the critical angle increases.

5.5) General conclusion

In this section we proposed a simple technique to analyze X-ray and neutron reflection data from a macroscopically rough surface. It was shown that in the limit that the correlation length and the height of the surface roughness are larger than the wavelength (at least 100 time bigger) of the incoming beam, the total reflection edge in the reflection profile becomes rounded. Using neutrons or X-rays to study the structure of an interface the wave length of the incoming beam is in the range of 1 Å to 8 Å, it is possible to use the formalism described above to analysis if the correlation length of the surface structure is in the range of 100 to 800Å or even bigger.

One of the must interesting characteristics of this technique is the possibility to apply it near the region of the total reflection. In this region the flux of the reflected beam is high, and it allows one to measure directly the *kinetics* of the surface roughening transition as chosen parameters of the system varies. We demonstrate that it is possible to consider the rough surface as an Ising lattice and to apply the thermodynamic theory of the phase transition to the variation of the divergence of the reflected beam as a function of time and to follow the kinetic of a roughening process by analysing the variation of the latter as a function of time. However, one must keep in mind that this analogy is only a formal one and therefore, no energetic consideration can be carried out from the obtained results.

We have applied this technique to diverse systems, and for each of them we were able to determine the kinetics of the roughening transition. They include the ripple phase transition in a model bilayer [21] and the roughening of a silicon surface by hydrogen evolution (Chapter VI and VII)

References

1 M. Born and E. Wolf, *Principles of Optics, Sixth edition* (Pergamon, 1980).

2 L. Barbabsi and H.E.Stanley, *Fractal Concepts in Surface Growth* (Cambridge university press, Cambridge, 1995).

3 J. Daillant and A. Gibaud, *X-Ray and Neutron Reflectivity: Principles and Applications*, (1999).

4 D. K. G. d. Boer, Physical Review B **49**, 5817 (1993).

5 P. Beckmann and A. Spizzichino, *The Scattering of electromagnetic waves from Rough surfaces* (Pergamon, London, 1963).

6 P. Croce and L. Nevot, Revue de Physique Appliquee **11**, 113 (1976).

7 L. Nevot and P.Croce, Revue. Phys. Appl **15**, 761 (1980).

8 S. K. Sinha, E. B. Sirota, S. Garoff, et al., Physical Review B **38**, 2297 (1988).

9 J. Daillant and O. Belorgy, Journal of Chemical Physics **97**, 5837 (1992).

10 P. Croce, L. Nevot, and B. Pardo, C. R. Acad. Sc. Paris **Serie B**, 855 (1972).

11 P. Croce, L. Nevot, and B. Pardo, C. R. Acad. Sc. Paris **Serie B**, 803 (1972).

12 L. Landau and E. Lifchitz, *Physique statistique* (Edition Mir, 1994).

13 H. E. Stanley, Reviwe of Modern Physics **71**, S358 (1999).

14 J. D. Jackson, *Classical Electrodynamics*, New York, 1975).

15 J. Daillant and O. Belorgey, J. Chem. Phys. **97**, 5824 (1992).

16 J. M. Ziman, *Models of desorder*, (Cambridge, 1979).

17 B. B. Mandelbrodt, *The fractal Geometry of Nature* (Freeman, New York, 1982).

18 S. K. Sinha, M. Tolan, and A. Gibaud, Physical Review B **57**, 2740 (1998).

19 J. A. Ogilvy, *Theory of wave scattering from random rough surfaces* (Adam Hilger, Bristol U.K, 1991).

20 P. Meakin and H. E. Stanley, Physical Review Letters **51**, 1457 (1983).

21 A. V. Hughes, A. Goldar, M. C. Gestenberg, et al., submitted to PCCP, (2001).

Chapter VI

The Effect of Hydrogen on the Morphology of n-type Silicon Electrode Under Electrochemical Conditions

"It's an experience like no other experience I can describe, the best things can happen to a scientist, realizing that something that's happened in his or her mind exactly corresponds to something that happens in nature. It's starling every time it occurs. One is surprised that a construct of one's own mind can actually be realized in the honest-to-goodness world out there. A great shock, and a great, great joy."

Leo Kadanoff

6.1) Introduction.

It is well known that under electrochemical conditions, hydrogen can have a considerable role in determining the surface morphology of silicon electrodes, and the incorporation of hydrogen into the silicon lattice is both of applied and fundamental interest[1]. *Mandal et al*[2] have shown that hydrogen atoms can be incorporated into the silicon electrode electrochemically, and have suggested that the hydrogen modifies the morphology of the electrode surface increasing its rms roughness. However, the detailed behaviour of hydrogen at the silicon surface has not been investigated thoroughly, and the kinetics and mechanism of the incorporation process are still relatively poorly understood.

In the case of silicon as well as for other electrode materials, under cathodic polarization the hydrogen evolution reaction takes place through two successive steps[3]. The first is proton discharge and formation of an adsorbed hydrogen species:

$$H^+ + e^- \rightarrow H_{ads}$$

Equation 6.1

The second step may be either a chemical recombination step or an electrochemical desorption step

$$H_{ads} + H_{ads} \rightarrow H_2$$

Equation 6.2

$$H_{ads} + H^+ + e^- \rightarrow H_2$$

Equation 6.3

However, in the case of silicon, the hydrogen adsorbed at the surface may penetrate into the electrode material, where its diffusion coefficient is not negligible, even at room temperature. *Mandal et al* [2] showed by investigation on Ge and Si, that for both semiconductors a thin layer (~ 100 Å)[3] of disordered and highly concentrated hydrogen (~ 10^{21} cm^{-3}) could be formed below the electrode surface.

The efficiency of the electrochemical loading of hydrogen into semiconductors has been demonstrated by secondary-ion mass spectroscopy profiling of deuterium [4]. In silicon, the profiles indeed exhibit a high concentration of deuterium atoms near the surface. On the other hand, several authors have reported roughening of the silicon surface when silicon is maintained under cathodic conditions during several hours. *Mandal et al*[2] suggest that the damaging of the surface is associated with the high density of incorporated hydrogen for two reasons. Firstly, massive penetration of hydrogen will induce a high density of lattice defects, and secondly, the H atoms will tend to form H_2 molecules, and the subsequent evolution of the H_2 gas will damage the already weakened surface.

To gain a better understanding of the processes occurring at the electrode surface, some form of *in-situ* characterisation is desirable. Neutron scattering methods are ideally suited to this task since silicon is almost transparent to neutrons, and thus the incident beam can be transmitted through the electrode without significant attenuation, allowing the silicon/electrolyte interface to be easily reached. Neutron reflectivity measurements from the interface can provide information about the roughness and morphology of the electrode surface. For example, *Penfold and Thomas* [5] showed that by analysing the specularly reflected beam from a surface one can extract the roughness normal to the surface and the diffuse scattering gives some information about the structure of the in plane roughness and its statistics[6].

In Chapter V, we have shown that in addition to the information obtained from conventional fitting of reflectivity profiles, information about the macroscopic roughness of the interface can be obtained by close inspection of the changes that occur near the region of the total reflection. Specifically, where a significant roughness exists, the specular component of the reflection is decreased by a greater scattering from the rough surface, and this changes the shape of the reflectivity profile near to the critical edge. A detailed analysis of the shape of the critical angle allows information about the surface morphology to be obtained. The advantage of this method for kinetic measurements is that the reflected intensity at the critical angle is high (compared with the off-specular intensity and the intensity at high wavevector transfer Q), allowing rapid collection of data in the region of interest. Hence by observing the kinetics of the changes in intensity near the critical angle one can study the kinetics of morphological changes of the interface on a macroscopic scale. In this

chapter, we have utilised this effect to investigate *in-situ* the surface roughening of a n-type silicon electrode in 40% NH_4F solution under cathodic polarization.

6.2) Experimental

6.2.1) Electrochemistry

The electrochemical cell used for the *in-situ* neutron measurements is shown in Figure 6.1.

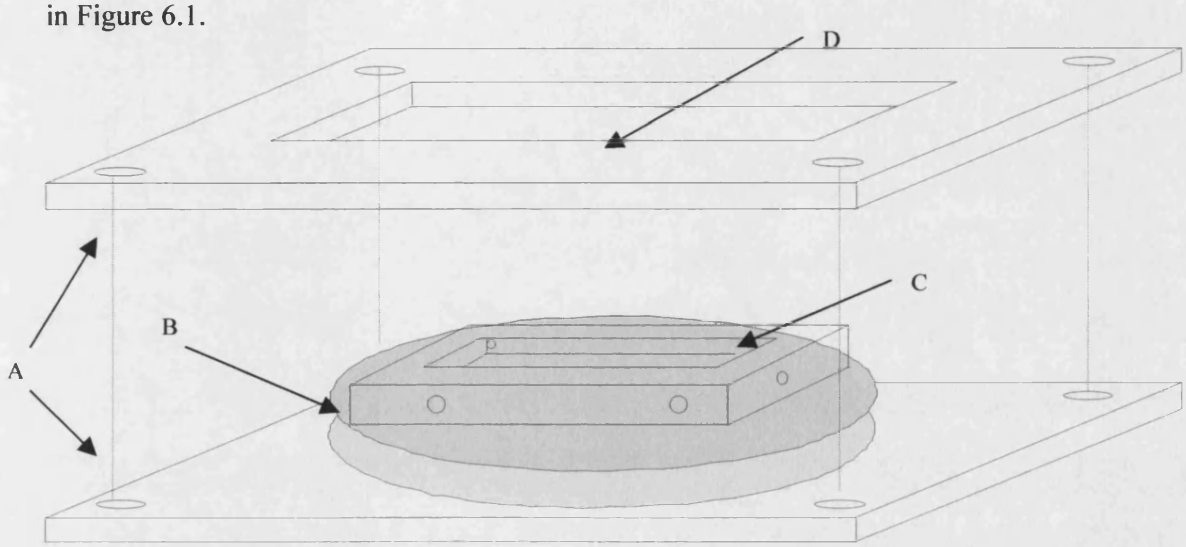

Figure 6.1. The schematic representation of the cell used in the neutron reflectivity experiment. (A) Two stainless steel plate. (B) silicon ingot. (C) The PTFE spacer. (D) Quartz window

A large circular silicon ingot (diameter: 10cm, thickness: 1cm, resistivity: 0.1-0.4 Ω.cm crystal orientation [111]) is in contact with a PTFE reservoir (internal dimensions 5cm x 4cm x 1cm). The back of the silicon ingot was coated with an evaporated gold film to facilitate electrical contact with the electrode. A platinum grid (5cm x 1cm) was mounted within the PTFE cell to act as the counter electrode such that the separation between the platinum and the silicon surface was 0.5 cm. Three Omnifit taps in the edge of the PTFE were used to enable exchange of electrolyte during the reflectivity measurements. The opposite side of the PTFE spacer was covered by a quartz window (which was closed during this experiment) and the whole assembly was clamped between two stainless steel plates and sealed with silicone grease to prevent leakage. All potentials applied across the cell are quoted relative to a

Saturated Calomel Electrode (SCE), which was connected to the cell by a PTFE Luggin capillary.

The electrolyte solution used is summarised in Table 6.1.

pH	NH_4F/mol.dm^{-3}	NH_4Cl/mol.dm^{-3}	NH_4Ac/mol dm^{-3}	HAc/mol.dm^{-3}
4.5	0.1	0.86	0.04	0.06

Table 6.1. The composition of the electrolyte.

Ammonium chloride and ammonium acetate are the background electrolytes and the acetic acid is used in order to adjust the pH to 4.5. The solutions were made up in both D_2O and H_2O to allow measurements at two neutron contrasts. All solutions were thoroughly de-gassed before use by bubbling N_2 through the solutions for 10 minutes. The potential across the cell was applied by a computer and controlled by a DT131 Hi-TEK potentiostat.

6.2.2) Reflectivity

6.2.2.1) Neutron Measurements

The experiment was carried out on the reflectometer beam line (TAS 8) at the Risø National Laboratory, Denmark. The cell was mounted vertically on the reflectometer beamline. The silicon/electrolyte interface could be illuminated through the silicon block, because of the relatively high transparency of silicon to neutrons. Cold neutrons of wavelength $\lambda = 4.75$Å were used. The neutron beam was collimated by two sets of slit packages (comprising vertical and horizontal slits) placed up- and downstream of the sample. The horizontal slits were kept at an aperture of 20 mm during the measurements to reduce the background, the vertical slit are set at: 0.3,0.35,0.7 and 1.0 mm. The apertures were chosen such that the footprint of the beam was kept smaller than the size of sample to avoid corrections to the measured intensity, except at the lowest angles.

6.2.2.2) X-Ray Measurements.

The X-ray reflection experiment was carried out with a home made X-ray reflectometer with energy sensitive detection at the University of Bath (Chapter IV).

6.3) Results and Discussion.

As was described in the introduction, it is well known that the electrical incorporation of hydrogen into a silicon lattice produces a severe roughening of the surface. This in turn should change the shape of the reflectivity profile at the critical edge. Figure 6.2.a shows standard X-ray reflectivity data for a virgin silicon electrode/air interface, and figure 6.2.b the reflectivity model which fits the data. Table 6.2 shows the fitting parameters used to fit the data (χ^2=7.2519*10^{-2}). All the data are fitted by using Parrat formalism which is discussed elsewhere[7].

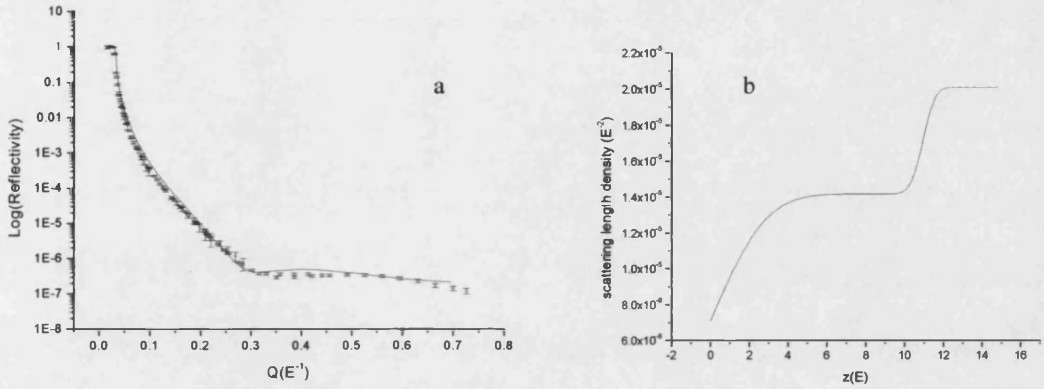

Figure 6.2. a. X-ray Reflectivity profile from a native silicon wafer surface. The open circles represent the data and the black line the fit. **b.** The scattering length density profile of the silicon wafer/air interface

	Thickness (Å)	Scattering length density ($Å^{-2}$)	Roughness (Å)
Silicon oxide	10.93	1.419*10^{-5}	3.15
Silicon substrate		2.012*10^{-5}	0.7

Table 6.2. Parameters obtained by fitting the reflectivity profile by Parrat formalism.

As we can see a layer of 10.93Å of silicon oxide covers the silicon electrode and the roughness parameters are of the order of a few Angstroms. Figure 6.3.a shows neutron reflectivity data near the total reflection region for a virgin silicon electrode against a D_2O subphase. The reflectivity from the same region of the same electrode after cathodic polarization at –0.7V in 40% NH_4F for 4 hours is shown by curve 6.3.b. As can be seen, there is a dramatic difference in the reflectivity profile between the two cases. In the profile from the smooth substrate, the critical angle is well defined and a little rounded due to the resolution of the spectrometer whereas after the cathodic

polarization the profile is smoother and does not show such a well-defined critical edge.

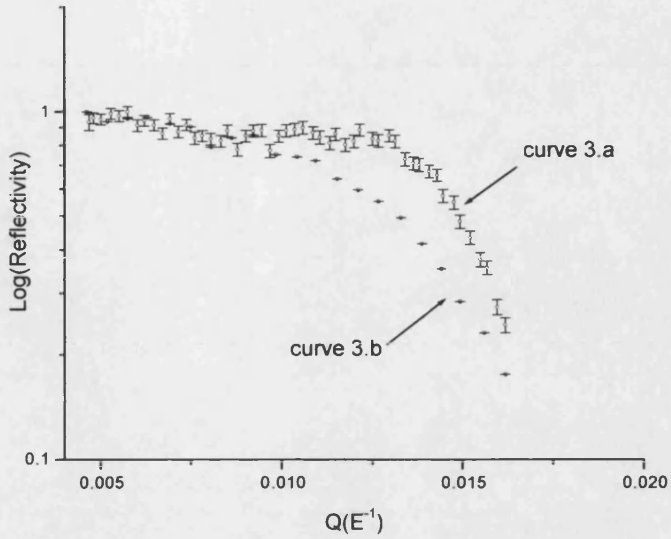

Figure 6.3 a. The reflectivity profile from the native silicon electrode/deuterium interface near the total reflection edge. **b**. The Reflectivity profile from the silicon electrode after the cathodic polarisation /deuterium interface near the total reflection edge.

By keeping the angle of incidence constant and varying the detector position in the vertical direction, it is possible to examine the degree of divergence of the reflected beam. As the detector is moved through the beam, a plot of intensity versus position should yield a Gaussian, with the maximum at the specular angle, and the FWHM

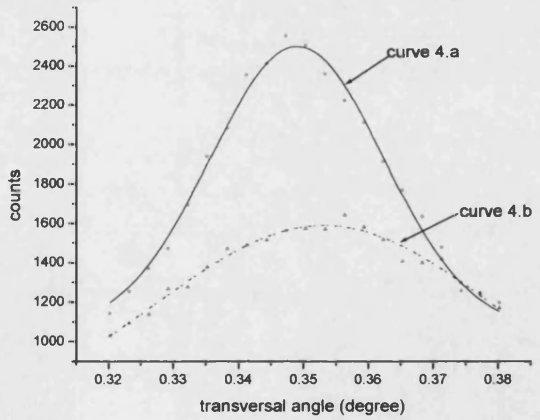

Figure 6.4. a. The "rocking curve" around the direction of specular reflection for the native silicon wafer/ deuterium interface. The open circles are the experimental data and the black line is the fit. **b**. The "rocking curve" around the direction of specular reflection for the silicon electrode/ deuterium interface after cathodic polarization. The triangles represent the experimental data and the dashed line the fit.

corresponding the to 'spread' or divergence of the beam. As can be seen, the beam reflected from the roughened surface (Figure 6.4.b) is far more diffuse than that reflected from the flat silicon surface (Figure 6.4.a).

Table 6.3 shows the fitting parameter used to fit the data of figure 6.4 by a gaussian. The parameter w represents the width of the gaussian function. As we can see the value of w is increased after the cathodic polarization.

$2*\theta_c$=0.44	$2*\theta$	y_0	A	W	Ω_c	R^2
Native silicon	0.7	1059.492+/- 53.26877	47.995+/- 3.58345	0.02659+/- 0.00124	0.34902+/- 0.00025	0.9897
After cathodic polarization	0.7	592.879+/- 291.15718	63.86409+/- 31.03983	0.05122+/- 0.01032	0.35313+/- 0.00041	0.97122

Table 6.3. The fitting parameters to the "rocking curves" around the specular direction.

It should be emphasised that neither the sample position nor the reflectometer configuration were altered during these measurements, hence an increase in the angular divergence of the reflected beam cannot be explained by a loss of instrument alignment. In this case, therefore, the loss of beam coherence must be caused by intrinsic changes in the nature of the interface. Specifically, that the roughened surface scatters the incident beam causing an effective increase in the angular divergence of the reflected beam.

Information regarding the microscopic roughness of the interface is, of course, available from a more conventional fitting of the full reflectivity profile. However, these techniques cannot handle macroscopic roughness. The advantage of considering only the region at the critical edge is the speed of data acquisition. Whilst collecting a full reflectivity profile (up to Q_z of ~0.4Å^{-1}) generally takes several hours, data in the region of the critical edge can be collected within a matter of seconds. This then affords the possibility of collecting kinetic data about the morphological changes as the hydrogen is adsorbed into the silicon.

Figure 6.5 shows the variation in the reflected intensity at the critical edge as a function of time, together with the applied potential. As can be seen, before a potential is applied the intensity remains essentially constant, indicating that the surface of the silicon is not spontaneously changing in the chemical, as opposed to

electrochemical environment and that the configuration of the instrument is stable (there is no loss of alignment). After the potential is applied, a sudden dramatic decrease in intensity is observed, followed by an exponential increase, until a new,

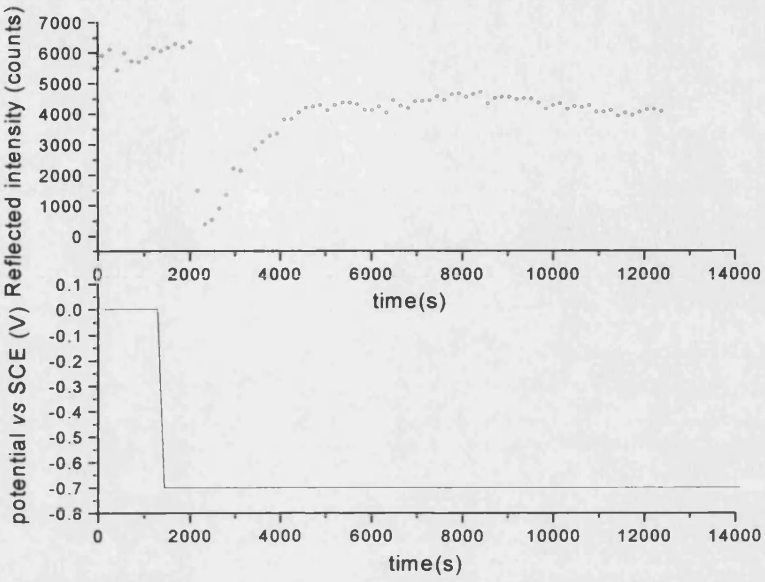

Figure 6.5. The reflected intensity from the silicon electrode/ deutrated electrolyte solution at $2\theta=0.6°$, during the cathodic polarization (at Q= 0.0138 $Å^{-1}$).

constant value is obtained approximately 2000 seconds after the potential was first applied. Thus, the critical edge measurements do indeed contain information regarding the kinetics of the hydrogen adsorption process.

In Chapter V, we have shown that the change in the shape of the critical angle can be quantitatively related to the change in the morphology of the substrate. Here we outline again the aspects of the theory necessary to understand these results.

If an incident wave of wavelength λ illuminates a rough surface the intensity scattered by the sample can be measured in a broad range of directions. The effect of the surface roughness on the reflectivity profile depends on the lateral correlation length of the surface and the ratio between the rms value of the surface roughness and the wavelength of the incoming beam [8]. When the ratio and the correlation length are small, the "off-specular" component of the reflected beam does not affect the specular component[8]. However, when the ratio and the surface lateral correlation length become bigger, the roughness cannot be considered as a perturbation to the surface

profile, and affects dramatically the specular reflectivity profile near the total reflection edge, where the interaction between the incoming radiation and the substrate is important.

In this case one can consider that the intensity of the reflected beam is distributed over a range of angles, θ, around the angle of the incident beam $\theta_{specular}$. We consider that difference between the angle θ and the angle of incident beam ($\alpha=\theta_{specular}-\theta$) is a gaussian variable. In this case the reflectivity can be written as:

$$R(\theta) = A \int_{-\theta_{mach}}^{+\theta_{mach}} R(\theta_{specular} - \alpha)\cos(\alpha)P(\alpha)d\alpha$$

Equation 6.4

Where P(α) is the distribution of the angular divergence of the reflected beam, A is a normalization constant and θ_{mach} is the angular acceptance of the spectrometer in the scattering plane divided by two.

Since the movement of hydrogen into and out of the lattice roughens the surface, the change in substrate morphology should be related to the rate of movement of hydrogen, therefore consideration of the kinetics of the roughening should provide an insight into the mechanism of hydrogen diffusion.

6.4) Mathematical model

We use equation 6.4 and make the following assumption: The hydrogen incorporation process perturbs the perfectly flat interface and changes the average value of the reflectivity from that from the flat surface. If the effect of the perturbation on the reflectivity is weak (i.e. we can still detect reflection from the sample in specular direction) the changes in reflectivity coefficient can be expressed by using the limited expansion of the reflection coefficient as a function of α. In other words we can consider α to be small:

$$R(\theta_{specular}-\alpha)\approx R_f(\theta_{specular})-\alpha\frac{dR(\theta_{specular}-\alpha)}{d\alpha}\bigg|_{\alpha=0}+O(\alpha^2)$$

Equation 6.5

Where the third term in equation 6.5, $O(\alpha^2)$, represents terms of the expansion whose order is equal or bigger then α^2.As α is small we limit our approximation to the first term of the equation 6.5. By introducing equation 6.5 into equation 6.4 we can express the value of the reflection coefficient in term of two integrals:

$$R(\theta)\approx AR_f(\theta_{specular})\int_{-\theta_{mach}}^{+\theta_{mach}}\cos(\alpha)P(\alpha)d\alpha-\int_{-\theta_{mach}}^{+\theta_{mach}}\alpha\left(\frac{dR(\theta_{specular}-\alpha)}{d\alpha}\bigg|_{\alpha=0}\right)\cos(\alpha)P(\alpha)d\alpha$$

Equation 6.6

The integrand in the second integral is odd and as the integration is over a symmetric region, the value of the second integral is zero. The first integral is just the value of the ideal reflectivity coefficient multiplied by the angular average of the cosine term. The reflectivity coefficient is the ratio between the reflected intensity from the sample and the intensity of the incoming beam, which impinges on the sample. Hence, by multiplying both sides of equation 6.6 by the intensity of the incoming beam we obtain the intensity of the reflected beam:

$$I(\theta)=I(\theta_{specular})A\langle\cos(\alpha)\rangle_{angular}$$

Equation 6.7

Equation 6.7 has the same form as *Lambert's (cosine) law*[9]. The first term in the right hand side of the equation 6.7 is the reflected intensity by an ideal surface in the specular direction. The second term represents the angular difference between the specular direction of reflection and the real direction of reflection averaged over the angular range accepted by the spectrometer. If the angular divergence, α, is very small we can neglect the cosine term and the divergence of the reflected beam. Therefore, the average value of the cosine term depends on the angular distribution of the reflected beam.

As we showed in the Chapter V, two factors can contribute to the divergence of the reflected beam: the resolution of the spectrometer and the surface of the sample. In fact, if the resolution of the spectrometer were bigger than the angular divergence introduced by the sample, one would see only the effect of the spectrometer resolution (this is the normal case). However, if the angular divergence of the reflected beam is mainly due to the sample, one would see the effect of this divergence. In order to be able to take into account these conditions in equation 6.7, we defined the constant A as[10] :

$$A = \max(1, \frac{\Delta\alpha}{\Delta\theta_{mach}})$$

Equation 6.8

Where, $\Delta\theta_{mach}$ is the angular resolution of the spectrometer, $\Delta\alpha$ is the size of the angular range over which the beam is divergent. Therefore, the normalization constant is defined as the ratio between the resolution of the machine and the angular divergence of the reflected beam. As we are interested in the case where the divergence of the reflected beam is mainly due to the sample, we can write the equation 6.7 as:

$$I(\theta) = I(\theta_{specular}) \frac{\Delta\alpha}{\Delta\theta_{mach}} \langle \cos(\alpha) \rangle_{angular}$$

Equation 6.9

At this stage of our model, we have demonstrated that by use of equation 6.9 one can describe the intensity of reflected beam from a very rough sample. However, we are interested in a system whose roughness changes as a function of time, and therefore the divergence of the reflected beam is time dependent. In other words, the variable α depends on time. In this case, we do not have to take any ensemble average in the above equations since we are considering a particular surface structure of the sample[11] at a time t. In order to quantify this dependence we have to take into the account the diffusion process.

By following the roughening mechanism proposed by Mandal *et al*[2] one can explain the shape of the reflected intensity as a function of time at critical angle (Figure 6.5).

The first part of the curve corresponds to the region where the potential applied to the wafer is equal to zero. Here there are no changes at the silicon surface, but as the

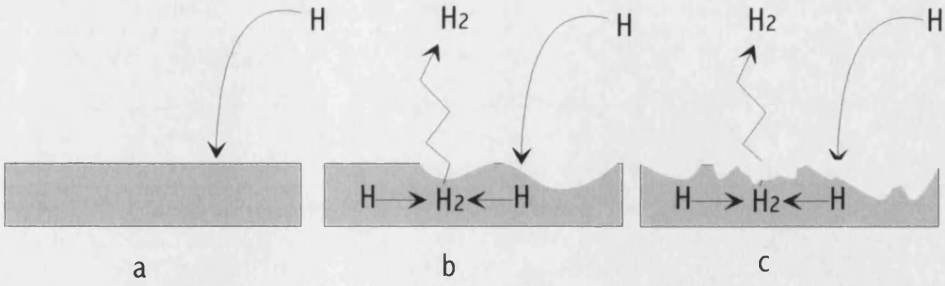

Figure 6.6. Schematic representation of roughening of the electrode surface during the cathodic polarization. The first scheme (a) represents the native surface before the roughening process. As the potential is switched to a negative value, a few H_2 bubbles are desorbed from the electrode and break the lattice, which create a rough surface with a low frequency (b). However as the potential is held at a negative value more and more H_2 bubbles are desorbed from the electrode. This process breaks more and more of the lattice and transforms the low frequency rough surface to a high frequency one (c).

potential is switched to –0.7V a large amount of hydrogen (or deuterium) is adsorbed at the surface of the silicon and penetrates into the silicon lattice. The hydrogen atom diffuses into the silicon lattice and as it encounters another hydrogen atom forms H_2 or D_2 molecule which break the silicon lattice and transform the flat surface to a macroscopically rough surface. However, as the adsorption/desorption process is isotropic over the surface it diminishes gradually the height and the lateral correlation length of the macroscopic roughness and acts as a process which changes the low frequency surface roughness to a high frequency one (Figure 6.6).

This is the reason why the reflected intensity at low Q increases as a function of time. Hence, we suppose that the rate of the roughening process is a combination of the adsorption of the atomic hydrogen, the diffusion of the hydrogen (or deuterium) in the silicon lattice, the reaction rate and the desorption kinetics.

As we consider the effect of the perturbation weak, we can approximate the angle α by Figure 6.7:

$$\alpha = \sqrt{\frac{\left\langle u(r,t)^2 \right\rangle_{surface}}{d^2}}$$

Equation 6.10

Where, $< >_{surface}$ is the average over the surface of the sample, u(r,t) is the local height of the surface at the coordinate r of the surface at time t and d is the characteristic length over which the surface keeps a constant orientation.

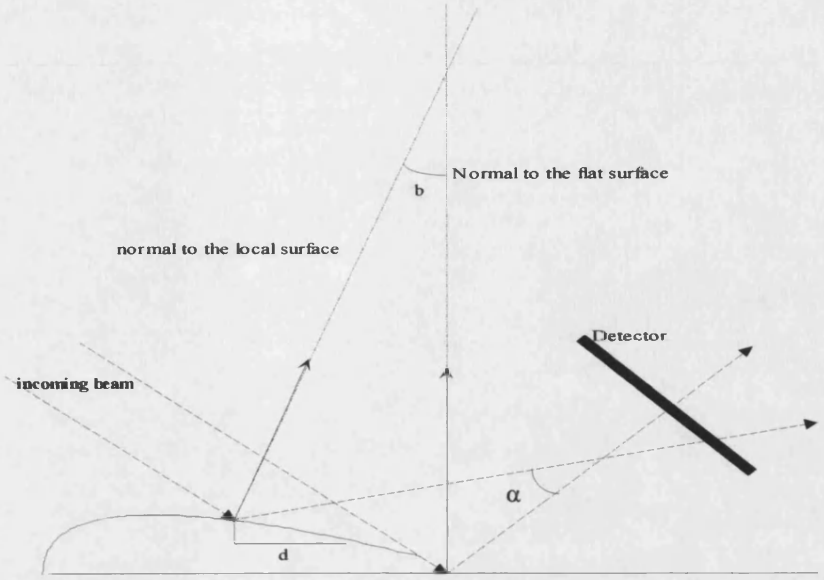

Figure 6.7. . Schematic representation of the surface of a rough sample. The projection angle α is linked to the angle, b, between the normal to the real surface and the normal to the ideally flat surface by the relation α=2b. We suppose that the surface is illuminated with an incoming beam of incident angle $\theta_{specular}$ with the flat surface and θ with the real surface. Only specular reflection is considered here.

Equation 6.1 describes the adsorption process of the hydrogen into the silicon electrode. As we can see this process is dominated by the rate of electron transfer between the electrode and the electrolyte. Equations 6.2 and 6.3 describe the desorption process. This step may be either due to the fact that two adsorbed hydrogens encounter each other in the silicon lattice or adsorbed hydrogen encounters a H^+ atom in the solution and gains an electron. In this step the rate of the reaction is a combination between the rate of the diffusion of the adsorbed hydrogen in the silicon lattice and the rate of the electron transfer reaction. *Allongue et al* [12] show that at cathodic bias the large density of free electrons in silicon favours the recombination of adsorbed hydrogen with protons present in the solution. Furthermore *Mandal et al* [2] suggest that the improvement of the hydrogen evolution kinetics observed on a n-Si[111] electrode, is strongly linked to the roughening of the electrode surface by the formation of H_2 molecules from the adsorbed hydrogen. Diffusion is faster in the solution than in silicon, so the formation of H_2 molecules is slower in the silicon

lattice than in the solution. As the kinetics of the change in the surface roughness must be limited by the slowest step in the reaction we assume that the change in time of the height u(r,t) (the local height of the surface) is linked to the diffusion of hydrogen (or deuterium) in the silicon lattice. Therefore, as the H_2 bubbles are desorbed from the silicon electrode the local height of the surface changes. In the previous paragraph we argued that the periodicity of the surface roughness becomes smaller as the H_2 bubbles are desorbed from the silicon electrode. In this case we can write the variation of the angle α as a function of time as:

$$\alpha \sim \frac{D^{\frac{1}{2}}}{d} t^{\frac{1}{\beta}}$$

Equation 6.11

Where the constant D is the diffusion constant of the hydrogen (or deuterium) in the silicon lattice. The exponent β depends on the kind of diffusion regime.
We can use also equation 6.11 to calculate the variation of the size of the domain over which the reflected beam is divergent. So we can write equation 6.9 as:

$$I(\theta) = I(\theta_0) * Bt^{\frac{1}{\beta}} \cos(2Bt^{\frac{1}{\beta}})$$

Equation 6.12

Where

$$B = \frac{D^{1/2}}{d}$$

Equation 6.13

Equation 6.12 expresses the variation of the reflected intensity as a function of time. As we can see the constant B depends on the diffusion constant D and the length d. The parameter d is the distance over which the surface of the sample has the same orientation. The variation of B as a function of time would be significant if the in-plane resolution of the spectrometer permitted us to follow the variation of the distance d as function of time. In our case, the typical in-plane coherence length of the incoming beam is of the order of microns, which means that if the orientation of the

surface changes on a distance scale smaller than a micron, we wont be able to see any effect of B on the reflected intensity, and B is effectively a constant.

To summarise, in this section we have linked the variation of the reflected intensity to the diffusion of the hydrogen (or deuterium) in the sample. In the next section we apply this formalism to the data described previously and compare the obtained results to the existing literature.

6.5) Application of Theory and Discussion.

Figure 6.8 shows the variation of reflected neutron intensity as function of time during the hydrogen evolution reaction at three different angles.

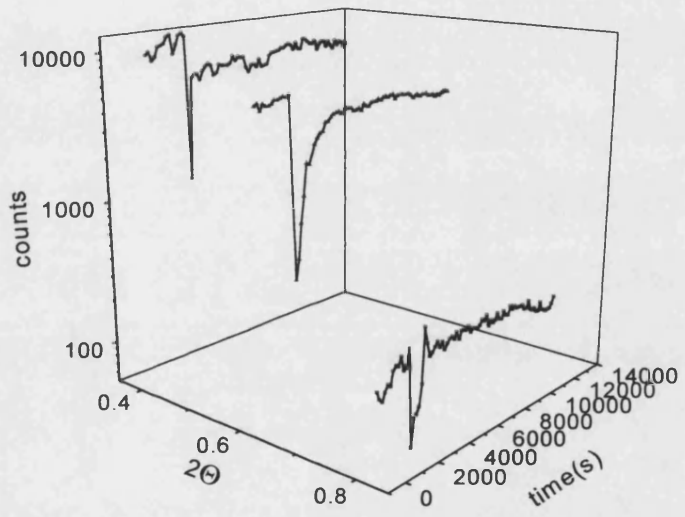

Figure 6.8. Reflected intensity from the sample at three different angles of incidence, as a function of time and the angle of incidence θ.

Figure 6.9 shows the variation of reflected intensity as a function of time during the hydrogen evolution reaction for two angles above the critical angle. The open circles represent the experimental data and the black line the fit with the equation 6.12. The fitting parameters are shown in Table 6.4. As can be seen, the parameter B and the exponent $1/\beta$ have the same value for the two different angles. However, for the sub-

critical (curve at θ=0.4 in Figure 6.8) region we observe only a drop in the value of the reflected intensity. The intensity of the reflected beam in the sub-critical region (where all the incident intensity is reflected) is not very sensitive to the variation of the momentum transfer. In this region all the intensity of the incoming beam is reflected, so the intensity of the reflected beam, from a perfectly flat surface, remains constant as the momentum transfer Q varies[10]. However, as the surface becomes rough the reflected intensity is smeared over a range of angles. The smearing of the reflected intensity can be considered by combining the reflected intensity from a perfect surface with a resolution function, as if a whole series of beams independently scatter from the sample, thus giving for observed intensity at nominal wave vector transfer Q a value of intensity average over many different Q values. As the intensity

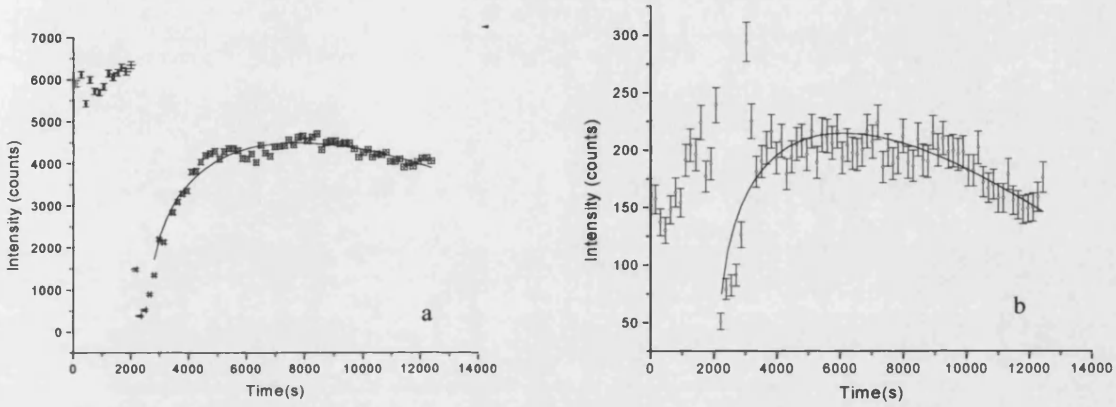

Figure 6.9. (**a**) The reflected intensity from the silicon electrode/deutrated electrolyte at 2θ=0.6°. The open circles represent the experimental data and the black line the fit. (**b**) The reflected intensity from the silicon electrode/deutrated electrolyte at 2θ=0.8°. The open circles represent the experimental data and the black line the fit

in the sub critical region is independent of the wave vector transfer the averaging over this region has the effect of dropping the overall reflected intensity.

$2*\theta_0$	$I(\theta_0)$	B	t_0	$1/\beta$	R^2
0.6	16044.9655 ±127.41679	0.01293 ±0.00156	2629.3114 ±15.04751	0.41042 ±0.01346	0.92577
0.8	764.8368 ±19.18519	0.0153 ±0.00644	2133.3751 ±129.24283	0.40267 ±0.0455	0.45771

Table 6.4. The fitting parameters to the reflected intensity.

The exponent 1/β is linked to the diffusion of hydrogen atoms in the silicon lattice. Diffusion process generally describes a Brownian motion, whose spatial and temporal distribution follow gaussian statistics, and thus Fick's second law describes the mean squared displacement in the course of time of a parameter x(t) as a linear temporal variation:

$$\langle x^2(t) \rangle \sim \psi t$$

Equation 6.14

Where ψ is a constant. However, if the hypothesis that the spatial and temporal distributions of a diffusion process follow Gaussian statistics breaks down, one can observe deviations from the linear time dependence of the mean squared displacement. This breakdown can be caused by either a broad distribution or a long-range correlation (such as broad spatial jump or waiting time distribution). In this case the non-linear growth of the mean squared displacement over the course of time can be expressed by a power law pattern:[13]

$$\langle x^2(t) \rangle \sim \psi . t^{\frac{2}{\beta}}$$

Equation 6.15

According to the value of the anomalous diffusion exponent 2/β one can usually distinguish several domains:

$0<(2/\beta)<1$ sub-diffusive regime

$(2/\beta)=1$ normal diffusion regime

$(2/\beta)>1$ super-diffusive regime

The first significant point is that the exponent 1/β in our experiments is smaller than 0.5. This result suggests that the diffusion of hydrogen atoms follows a sub-diffusive regime in the silicon lattice.

Panzarini and Colombo[14] suggest a model for the diffusion of hydrogen in the silicon lattice. Figure 6.10 is representative of their model: H moves *via* a jump-like mechanism visiting preferentially the bond-centre (BC) site- the midpoint of a Si-Si bond- because it is the minimum energy position. H diffusion is a sequence *of stop-and-go* processes in which the pauses can have different durations. Moreover, forward

and backward jumps are equivalent and occur with the same frequency, but the length of the jumps depends on the temperature.

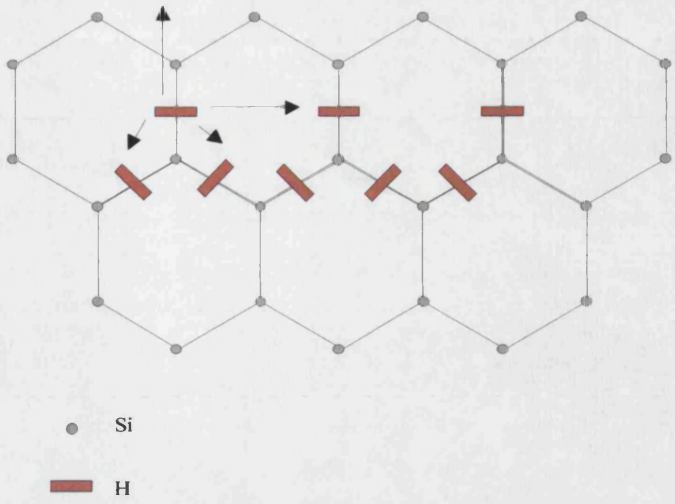

Figure 6.10. The schematic representation of the hydrogen diffusion in the silicon lattice. The red bars represent the hydrogen atoms. Two hydrogen atoms can encounter each other and form H_2 molecule that desorb from the silicon electrode by breaking the lattice.

If one discusses this model in term of a diffusion model, one would conclude that as the distribution of the waiting time ("pauses") is not uniform, the diffusion of the hydrogen atoms in the silicon lattice must deviate from the normal diffusion regime into the sub-diffusive one [14].

From equation 6.13 is possible to calculate the order of magnitude of the generalized diffusion coefficient [14] of the hydrogen atoms in the silicon lattice. The value of the parameter B is 0.01293. By using the definition of $B=D^{1/2}/d$ we find $D\sim10^{-11}$ $cm^2.s^{-0.8}$. By comparing this value to the value described in literature[13], $10^{-13}<D<10^{-11}$ $cm^2.s^{-1}$, we notice that the order of magnitude of the two values is in perfect accordance.

According to Figure 6.5 a sharp drop in reflectivity occurs some time after polarising the electrode (typically 10 min). The same kind of delay is seen in Figure 6.8 and Figure 6.9. As we noticed before, the roughening of the surface is due to the desorption of hydrogen bubbles from the surface. Before the hydrogen has to desorb from the silicon it has to absorb into the silicon lattice. This absorption is proportional to the difference of potential. Then the absorbed hydrogen has to diffuse in the silicon lattice in order to meet another hydrogen atom and to form a bubble. In order to change the reflected intensity, the size of the roughness created by the hydrogen

desorption must be equal or bigger than the coherence length of the incoming beam [11]. The size of the coherence length of the incoming beam is typically 1μm, the diffusion coefficient of hydrogen in the silicon lattice[13] at 298 K is equal to 7×10^{-11} $cm^2.s^{-1}$, therefore the time necessary for hydrogen to diffuse a distance equal to 1μm is calculated by the relation, $t \sim (d / D^{0.5})^{1/0.4}$~8.23 min. From this approximate calculation, the average time necessary for hydrogen to diffuse a length equal to the size of the coherence length of the incoming beam is around 8 minutes. Hence, the fact that the sharp drop in the reflectivity intensity happen 10 minutes after the polarization can be considered due to the formation of the first surface roughness which has a dimension bigger than the coherence length of the incoming beam.

On one hand, the value of the exponent 1/β, which demonstrates a sub-diffusive regime for the diffusion of hydrogen into the silicon lattice, is in good agreement with the model described by Panzarini and Colombo[14].

The second significant point is that we can suggest an interpretation of the temporal variation of the reflected intensity, and a mathematical model (equation 6.10), which fit the experimental data.

In order to establish equation 6.12 we made two important assumptions. The first assumption is that the silicon surface roughening process under cathodic polarization is directly linked to the diffusion of the hydrogen atoms in the silicon lattice (which represent the limiting step in the roughening process): As two absorbed hydrogen atoms encounter each other they form a H_2 molecule. The H_2 molecules form a bubble, which breaks the lattice and transforms the flat surface to a macroscopically rough surface. The second assumption is to consider that the angular deviation α is small. In Chapter V ,we showed that the shape of the total reflection feature (where the interaction between the incoming beam and the sample is important) is dependent on the size of the surface roughness and particularly on how this roughness changes the local surface orientation. One of the ways to characterize changes in surface orientation is to measure the changes in local normal direction in respect to a reference direction. This quantity is generally measured by the autocorrelation function. Hence, by considering that the value of the angular divergence α is small we translate the fact that the lateral correlation length of the surface structure is large (but smaller than the in-plane coherence length of the incoming beam), and the equation 6.7 is the mathematical translation of the dependence of the intensity on the

local normal direction in the first approximation. Therefore, equation 6.12 is only valid if the perturbation produced by the polarization of the electrode is weak. Hence the sharp drop in the reflected intensity, which corresponds to a macroscopic roughening of the surface (the reflected intensity drops to zero), cannot be considered as a weak perturbation. However, if knowledge of the in-plane distribution of surface roughness is accessible equation 6.4 can be used to model the drop in intensity.
Finally, in this section we showed that we are able to fit the variation of the reflected intensity as a function of time by the equation 6.10. This result suggests that the rate of roughening process is determined by the anomalous diffusion of the hydrogen atoms in the silicon electrode.

6.6) Conclusions.

In this chapter we show that it is possible to correlate the changes of the specularly reflected intensity from silicon/electrolyte solution to the diffusion of hydrogen into the silicon electrode. We used the formalism developed in the Chapter V and the following picture: at the beginning of the process only a few H_2 molecules are desorbed from the electrode and therefore the surface lateral correlation length is big. However as the desorption process is carried out this correlation length becomes smaller. This picture suggests that the rate determining step for the roughening process of the silicon surface during the hydrogen evolution reaction is the desorption of hydrogen from the silicon electrode, which is why we have linked the changes of reflectivity intensity to the kinetics of the hydrogen diffusion into the silicon lattice. We have demonstrated that it is possible to use the specularly reflected intensity at a fixed angle to study the kinetic of the interface roughening process. Generally, the off-specular reflectivity technique is used to measure the structure of a rough surface. However when the lateral correlation length becomes very big, the surface structure affects the coherently reflected beam [8]. In this work we used this argument to measure the changes of the surface structure as a function of time, and we demonstrate, as the flux of the reflected beam is very high near the total reflection region, that this technique is suitable to study the dynamics of the surface roughening process.
We have shown that the changes of the silicon surface roughness under cathodic polarization are due to the adsorption and desorption of the hydrogen, and the kinetics

of these changes are dominated by the diffusion of the hydrogen atoms in the silicon lattice following a sub diffusive regime.

References:

1 S. J. Pearton, J. W. Corbett, and T. S. Shi, Appl. Phys. A **43**, 153 (1987).

2 K. C. Mandal, F.Ozanam, and J.-N. Chazalviel, Applied physics letters **57**, 2788 (1990).

3 J.-N. Chazalviel, in *Porous Silicon Science And Technology*, edited by J.-C. Vial and J. Derrien (Les Editions de Physique, Les Ulis, 1995), p. 17.

4 P. d. Mierry, A. Etcheberry, and M. Aucouturier, Journal of applied Physics **69**, 1099 (1991).

5 J. Penfold and R. K. Thomas, J.Phys: Condens.Matter **2**, 1369 (1990).

6 S. K. Sinha, E. B. Sirota, S. Garoff, et al., Physical Review B **38**, 2297 (1988).

7 L. G. Parratt, Physical Review **95**, 359 (1954).

8 D. K. G. d. Boer, Physical Review B **49**, 5817 (1993).

9 M. Born and E. Wolf, *Principles of Optics, Sixth edition* (Pergamon, 1980).

10 J. Daillant and A. Gibaud, *X-Ray and Neutron Reflectivity: Principles and Applications*, (1999).

11 L. Landau and E. Lifchitz, *Physique statistique* (Edition Mir, 1994).

12 P. Allongue, C. H. d. Villeneuve, L. Pinsard, et al., Appl. Phys. Lett **67**, 941 (1995).

13 R. Metzler and J. Klafter, Physics reports **339**, 1 (2000).

14 G. Panzarini and L. Colombo, Physical Review Letters **73**, 1636 (1994).

Chapter VII

Changes of the silicon electrode morphology by electrochemical etching

"Shine on, you crazy diamond"
Pink Floyd

7.1) Introduction

The ability to modify the structure and properties of silicon surfaces on an atomic scale by contact with a liquid offers a number of unique opportunities both for the fundamental study of these surfaces[1-11] and for surface processing under ambient conditions [12-15]. The interaction of silicon with fluoride ions has been the subject of several papers. Examples of process involving this interaction include: oxide removal [16], hydrogen passivation [17], porous silicon formation [11], chemical and electrochemical etching [7]and electropolishing [18].

Chemical etching of silicon in HF solution is important for oxide removal and in the formation of stabilised silicon surfaces by hydrogen passivation [17]. Recent works have shown a dramatic relationship between the etching process and surface structure [5, 12, 15, 19]. The advantage of an electrochemical study of the silicon / electrolyte interface is the ability to control the surface structure by changing the applied potential [13, 14, 20, 21].

A survey of the literature indicates that the etching properties of this interface have been correlated to the changes of the morphology of the surface. SEM, TEM, XPS, *in-situ* FTIR and AFM have been the major techniques used to characterize these interfaces. However, none of these techniques allow *in-situ* measurement of the kinetics of the surface morphology changes as a function of applied potential.

In the last chapter we studied the kinetics of the surface roughening of the silicon electrode during the hydrogen evolution reaction by using *in-situ* neutron reflection. In this chapter we investigate the changes of the surface morphology of the silicon electrode during electrochemical etching in 40% NH_4F.

In this chapter we first discuss the electrochemical etching of the silicon electrode in fluoride solution. In the second part we present the obtained results. The third part is devoted to the discussion of the data. Finally we will compare the data from the time resolved *in-situ* X-ray reflection during the chemical etching.

7.2) Electroetching

Fundamental reactions controlling the etching processes of silicon in fluoride solution are electrochemical in nature (because they involve an oxidation and reduction reaction) (figure 7.1) [9]

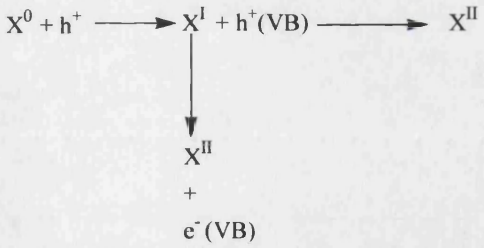

Figure 7.1. Dissolution of silicon in fluoride electrolytes. The first step is supposed to be a hole capture. X^0 is a surface silicon atom and X^I is a dissolution intermediate. In the second step hole capture by X^I competes with electron injection into the conduction band to form the intermediate X^{II} [Searson, #148]

Electrochemical investigations on the silicon / electrolyte interface have led to several surprising observations such as the formation of porous silicon [22] and the dark current transient after the oxide removal which occurs in fluoride electrolyte [23]. It was shown that changing the applied potential to the silicon / NH_4F interface changes the morphology of the silicon surface [20].

From figure 7.1 holes are required in the dissolution process [9]. Ignoring the intermediate step involved in the dissolution mechanism of the silicon electrode in fluoride solution, during the anodic polarisation of a n-silicon [111] electrode under illumination we can write the overall reaction (porous silicon formation) as [11]:

$$Si + 4HF + 2F^- + 2h^+ \longrightarrow SiF_6^{2-} + H_2 + 2H^+$$

Equation 7.1

This reaction takes place at the interface between the electrode and the electrolyte.

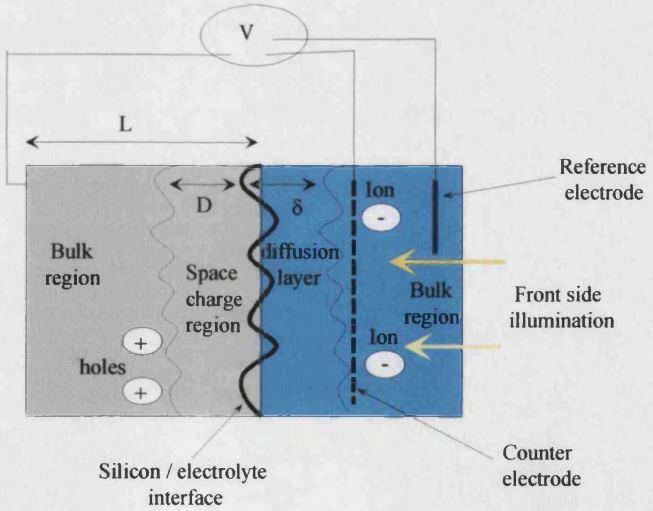

Figure 7.2. Illustration of the semiconductor / electrolyte inteface under front side illumination and an anodic polarisation. L is the thickness of the silicon electrode, D is the thickness of the space charge region and δ is the thickness of the diffusion layer.

The analysis in Chapter III showed that the dissolution of the silicon surface is characterised by the mass transport of holes in the semiconductor and the etchent in the solution and finally the consumption process of the reaction at the interface. A schematic representation of the semiconductor / electrolyte interface is given in figure 7.2 [11].

A.Valance [11] used the combination these three parameters, to model porous silicon formation. He showed that there is a critical wavelength for the fluctuation of the silicon / electrolyte interface which separates the domain of porous silicon formation from that of electropolishing. He demonstrated that if the wavelength of the interfacial fluctuations is smaller than a critical wavelength, λ_c, the formation of the porous silicon is favoured. However, if the wavelength of the interface's fluctuation is larger than λ_c the interface is stable and the electropolishing process is favoured [11]. Therefore, the transition between the porous silicon region and electropolishing region is induced by a change in the morphology, and particularly in the roughness [9], of the silicon / electrolyte interface.

A typical current – voltage curve for n-type silicon in NH_4F solution under illumination is characterised by three distinct regions, as shown in Figure 7.3.

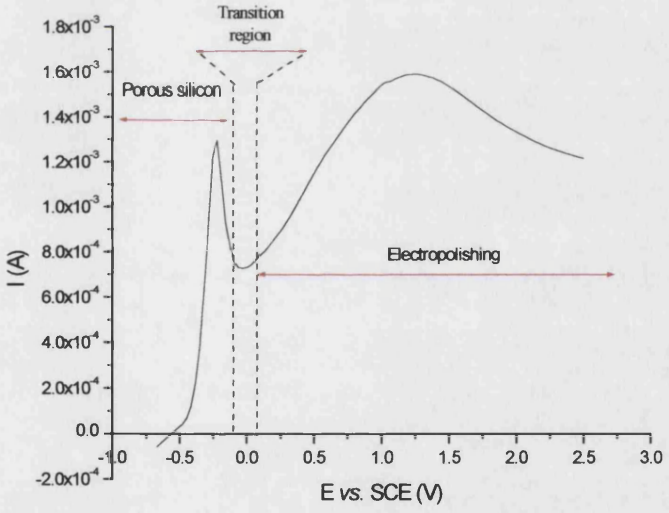

Figure 7.3. Current-voltage curve for a n-Si [111] (1-4 Ω.Cm) under very high light intensity illumination (white light, tungsten wire) in 0.1 M NH_4F solution pH=4.5. One applied ramp in forward direction from – 0.7 to 2.5 V (*vs.* SCE) with a scan rate of 10 $mV.s^{-1}$ was applied.

At low potentials the current increases sharply with potential, whereas at more positive potentials, beyond a characteristic current peak, the current is relatively large and increases with increasing potential. This latter region is the electropolishing region [8]. Between these two potential domains is a transition region [9] There features of both pore formation and electropolishing are observed [9]. The low potential region corresponds to the region of anisotropic etching [20] characterised by pore formation, whereas the higher potential region is characterised by isotropic etching [8]

The porous silicon formation region corresponds to the direct dissolution of the electrode material, and involves the presence of holes at the surface. This process leads to a rough and H-terminated silicon surface [8]. This roughening transition corresponds to the creation of steps with two dangling bonds on the silicon [111] surface [9]. The photo-induced electropolishing corresponds to the formation of an oxide layer on top of the silicon electrode [8, 9, 18]. The electropolishing "plateau" can be divided into two regions: When the potential is increased above the porous silicon formation region (till 1.3 V on figure 7.3), first the hydrogenated coating disappears and is replaced by a wet oxide or hydroxide layer (Si-OH) [8, 24]. Then a true oxide appears (Si-O-Si) but this takes place only above the broad current maximum (after 1.3 V on figure 7.3) [8, 24]. Therefore, in this case silicon dissolution proceeds through the formation of an interfacial silicon oxide layer and the etching process results in a uniform thinning and smoothing of the silicon substrate [9]. The amplitude of the current peak observed in electropolishing regime (at 1.3 V on figure 7.3) exhibits a square root dependence on HF or NH_4F concentration [9]. This suggests that the electropolishing mechanism becomes transport limited at high potential [9].

The above description of the dissolution of n-type silicon electrode under anodic polarisation and illumination in a fluorinated solution shows that the silicon / electrolyte interface undergoes morphological changes during electrochemical etching. These changes are characterised by a transition from a rough surface (produced by porous silicon formation) to a smoother surface (produced by the electropolishing).

The expected distance between the pores for a porous silicon material, formed on a n-type silicon electrode, is around 0.1μm [11]. This distance is 10 times smaller than the usual in-plane coherence length for neutron reflection (~1μm). As we described during electrochemical etching the surface of the silicon electrode undergoes a

transition between a rough surface and smooth surface. Therefore, there must exist an intermediate state during this transition where the surface morphology is characterised by a low frequency surface profile (the surface is "wavy"). By considering the theory and concepts developed in Chapter V we expect to be able to follow this "smoothing transition" by *in-situ* specular neutron reflection and to correlate it to the characteristic kinetic parameter of the transition (*i.e* the rate of silicon surface dissolution).

7.3) Experimental

The experimental procedure, the cell, solution, sample and instruments are the same as the ones described in Chapter VI.

The electroetching of n-type silicon [111] was performed in 0.1 M ammonium fluoride solution, described in chapter VI, under illumination and an anodic potential ramp after the electrode has been maintained at –0.7 V (*vs.* SCE) for 4 hours (see chapter VI). The potential ramp is applied in the forward direction from –0.7 V *vs.* SCE to 2.5 V *vs.* SCE with a scan rate of 1 $mV.s^{-1}$. The surface of the sample is illuminated by a white light through the electrolyte provided by an 110W light bulb (tungsten wire). The neutron beam illuminates the silicon / electrolyte interface through the silicon wafer. The variation of the reflected neutron intensity is collected at three different angles (0.4° , 0.6° and 0.8°) as a function of applied potential. At the end of the electrochemical etching, a full reflectivity profile from the Silicon / D_2O subphase is collected

The chemical etching is performed in the X-ray cell described in chapter IV, and the X-ray reflection experiments were performed at the University of Bath using the reflectometer described previously. The sample (5 cm^2 n-Si [111] (1-4 Ω.cm) provided by ACM) was mounted in the X-ray cell and cleaned by several rinses of acetone and Millipore water (18 Ω.cm). The oxide layer was cleaned by a solution of 30% H_2O_2: 70% H_2SO_4 at ~ 80 °C for 20 min. The sample with clean oxide layer is etched by a solution of 1% HF: 50% NH_4F [17], for 24 min and *in-situ* time resolved X-ray reflectivity data is collected in the region of total reflection at the same time.

7.4) Results and discussion

As was described in the introduction, it is well known that the photo-induced electrical etching of n-type silicon [111] in fluoride containing solutions can produce porous silicon or a smooth oxidised silicon surface. This in turn should change the shape of the reflectivity profile at the critical edge. Figure 7.4.a shows standard neutron reflectivity profiles for a n-type silicon [111] electrode / D_2O subphase before the roughening by the hydrogen evolution reaction, after the roughening process and after the electrochemical etching.

As we noticed in Chapter IV, it becomes difficult to model the specular reflectivity profile by classical existing algorithms when the surface of the sample is very rough. By comparing the three reflectivity profiles (Figure 7.4.a) we notice that the specular reflectivity intensity at high momentum transfer after the roughening of the surface by

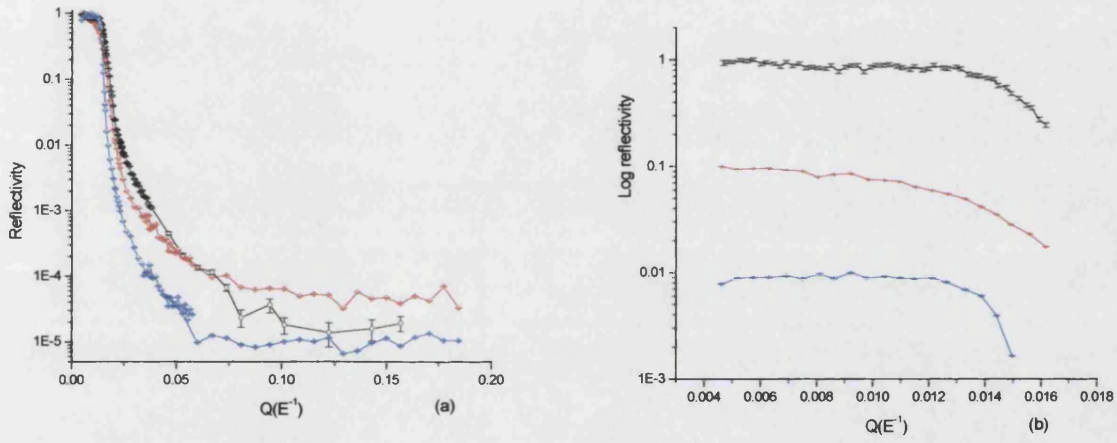

Figure 7.4 (**a**) Neutron reflectivity profile from the silicon / D_2O interface before the incorporation of hydrogen (black curve) after the incorporation of hydrogen (red curve) and after electrochemical etching (blue curve). (**b**) The neutron reflectivity profile from the silicon / D_2O interface in the region of total reflection. The profiles are rescaled. The silicon / D_2O interface before the incorporation of hydrogen (black curve) after the incorporation of hydrogen (red curve) and after electrochemical etching (blue curve)

hydrogen adsorption is higher than the intensities reflected by a virgin silicon surface or an etched silicon surface. This increase in reflected intensity can be relateded to the high degree of macroscopic roughness of the surface [25] which increases the diffuse scattering [26] and therefore the background scattered intensity. Figure 7.4.b shows neutron reflectivity data near the total reflection region for a virgin silicon electrode against a D_2O subphase. The reflectivity from the same region of the same electrode after cathodic polarization at -0.7V in 40% NH_4F for 4 hours and after electroetching

under illumination in 40% NH_4F are shown on the same figure. As can be seen, there is a dramatic difference in the reflectivity profile between the three cases. In the profile from the virgin substrate, the critical angle is well defined and a little rounded due to the resolution of the spectrometer whereas after the cathodic polarization the profile is smoother and does not show such a well-defined critical edge. However, after electroetching of the rough substrate the critical angle is well defined and is very sharp.

It should be emphasised that neither the sample position nor the reflectometer configuration were altered during these measurements, hence an increase or a decrease in the angular divergence of the reflected beam cannot be explained by a loss of instrument alignment. In this case, therefore, the loss of beam coherence must be caused by intrinsic changes in the nature of the interface. Specifically, that the roughened surface scatters the incident beam causing an effective increase in the angular divergence of the reflected beam and that the smooth surface decreases this divergence. .

As we discussed in chapter V and demonstrate in chapter VI, the advantage of considering only the region at the critical edge is the speed of data acquisition. Whilst collecting a full reflectivity profile (up to Q_z of ~$0.4Å^{-1}$) generally takes several hours, data in the region of the critical edge can be collected within a matter of seconds. This then affords the possibility of collecting kinetic data about the morphological changes of the silicon electrode during the photo-induced electrochemical etching.

Figure 7.5 shows the variation in the reflected intensity at the critical edge as a function of time, together with the applied potential during the photo-induced electrochemical etching of the electrode.

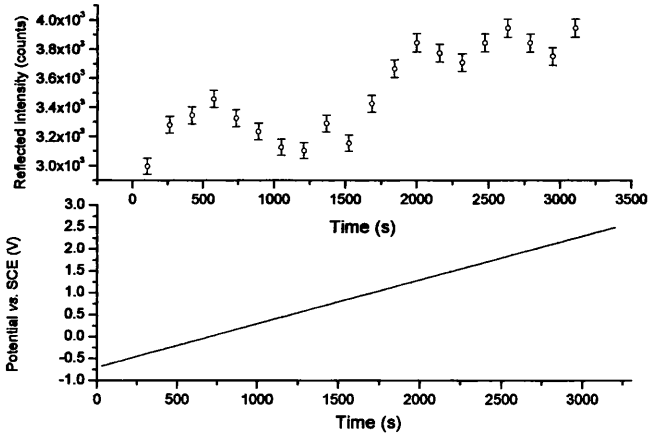

Figure 7.5. The reflected intensity from the silicon electrode / deutrated electrolyte

As can be seen, the total reflected intensity is increased (from 3000 to 4000 counts). Two important features can be observed in the behaviour of the reflected intensity as a function of time. The first one corresponds to the first intensity peak (t ~ 500 s) and the second one is the dramatic increase in intensity (t ~ 1250 s) until a new, "constant" value is obtained (t ~ 2000s). Thus, the critical edge measurements do indeed contain information regarding the kinetics of the photo-induced electroetching of silicon surface electrode.

Figure 7.6 shows the variation in the reflected intensity at the critical edge as a function of the applied potential, together with the current-potential curve during the photo-induced electrochemical etching of the electrode.

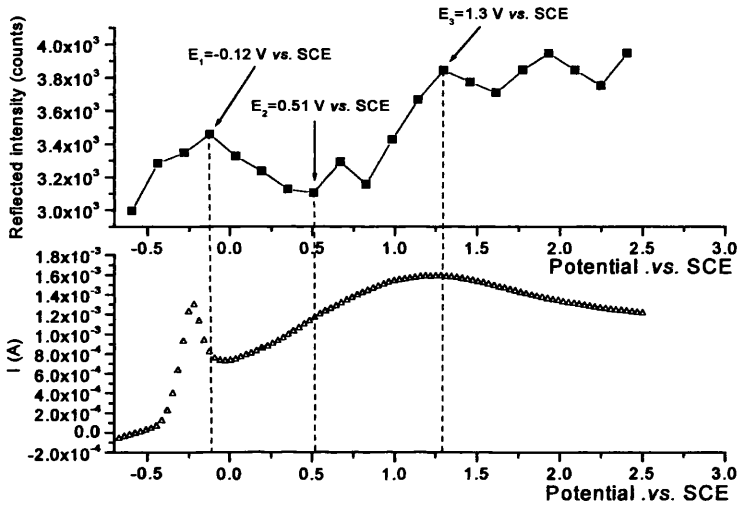

Figure 7.6. The reflected intensity from the silicon electrode / deutrated electrolyte solution at 2θ=0.6°, current-potential curve during the photo-induced electrochemical etching. (at Q= 0.0138 $Å^{-1}$)

As we can see, the first peak in reflected intensity (E_1) corresponds to the beginning of the transition region where both pore formation and electropolishing happen [9]. Then as the electropolishing regime predominates, the reflected intensity diminishes ($E_1 < E < E_2$). Between these two potentials the hydrogen coating of the surface is removed and is replaced by a hydroxide layer [8]. The formation of a smooth hydroxide layer and the dissolution of the porous layer become predominate in the first part of the electropolishing regime which corresponds to the first part of the broad peak observed in the current-potential curve [8] ($E_2 < E < E_3$). In this region of potential the reflected intensity increases sharply with the applied potential to reach a "plateau" at

the potential E_3. After this potential the reflected intensity oscillates slowly around a constant value as the applied potential increases. The domain of potentials lager than E_3 corresponds to the second part of the electropolishing regime where a smooth oxide layer is built at the surface of the electrode [8].

Since the dissolution of the porous layer and the deposition of the oxide layer in the electropolishing regime smooth the surface, the change in substrate morphology should be related to the rate of the dissolution of the silicon and (or) the rate of the oxide layer formation during the electropolishing, therefore consideration of the kinetics of the smoothing should provide an insight into the mechanism of dissolution and (or) the mechanism of the oxide layer formation.

In chapter V we have shown that the changes in the shape of the critical angle can be quantitatively related to the changes in the morphology of the substrate. In Chapter VI we used this observation to analyse the reflected intensity, during the hydrogen adsorption, at the critical angle. Here we will use the same kind of analysis as that used in Chapter VI, to relate the variation of the reflected intensity as a function of time to the changes in the morphology of the silicon electrode / electrolyte interface.

7.5) Mathematical model

In chapter VI we demonstrated that in the case of the roughening transition of the silicon surface by adsorption of hydrogen we could write the reflected intensity as

$$I(\theta) = I_0(\theta_{specular}) \frac{\Delta\alpha}{\Delta\theta_{mach}} \langle \cos(\alpha) \rangle_{angular}$$

Equation 7.2

Where $\theta_{specular}$ is the angle of incidence, $I_0(\theta_{specular})$ is the reflected intensity in the case of a sharp silicon / electrolyte interface, $\Delta\alpha$ is the angular divergence of the reflected beam, $\Delta\theta_{mach}$ is the angular acceptance of the spectrometer and the angle α corresponds to the angular difference between the direction of detection and the direction of reflection (Chapter V). The angle α is related to the surface of the sample by:

$$\alpha = 2\frac{\sqrt{\langle u(r,t)^2 \rangle_{surface}}}{d}$$

Equation 7.3

Where u (r,t) is the height of the surface profile at position r at instant t and d is the characteristic length over which the surface keeps a constant orientation.

The variation with time of the rms value of the height of the surface profile depends on four parameters: (i) transport of molecules and ions in the electrolyte, (ii) the transport and the concentration of holes in the semiconductor, (iii) the consumption process of the reaction at the interface and (iv) the rate of oxide deposition in the electropolishing regime. However, as the reflected intensity is measured near the total reflection region, the reflected intensity is not sensitive to the effect of the oxide layer (this observation is true if the thickness of the oxide layer is approximatively less than 2000 Å. As we cannot notice any interference fringes in the reflection profile (Figure 7.4.a) we assume that this condition is satisfied in our study). Therefore, all the changes in the reflected intensity in the region of the critical angle can be linked to the roughening or smoothing of the surface by the action of the three others parameters. Based on the order of magnitude of the relative importance of these three parameters we shall keep in the model only those parameters that are relevant to describe the variation of the reflected intensity as a function of time,

First, let us consider that the morphology of the interface changes so slowly with time that the density profile of holes adapts itself to any new interface morphology. In other terms we consider an adiabatic quasi-equilibrium state [11, 27] for the holes density profile (i.e. $\frac{\partial p}{\partial t} = 0$). Secondly, we neglect the recombination-generation of holes by thermal motion at the illuminated interface. This is justified provided that the surface of the electrode is illuminated by a constant intensity of white light, therefore the amount of holes presented at the surface is constant at each instant (see Chapter III).

In the electrolyte, the consumption of the reactant ions at the interface due to the etching process induces a concentration difference between the bulk and the interface region which gives rise to an ion current. We shall assume here that this current is essentially supported by fluorine containing species [7]. Equation 7.4 represents the equilibrium path for NH_4F in solution:

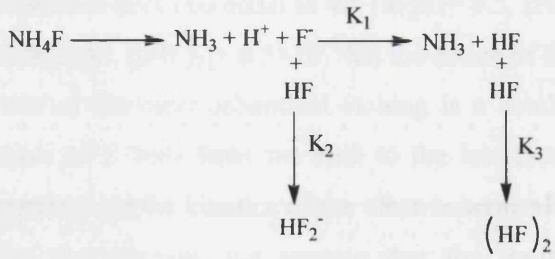

Equation 7.4

where K_1 (K_1=6.85×10^{-4}), K_2 (K_2=3.963) and K_3 (K_3=2.7) are the equilibrium constants [28]. Figure 4.7 shows the concentration of HF, $(HF)_2$, F^- and HF_2^- in the solution as a function of pH. They are calculated using equation 7.4 and the constants described above.

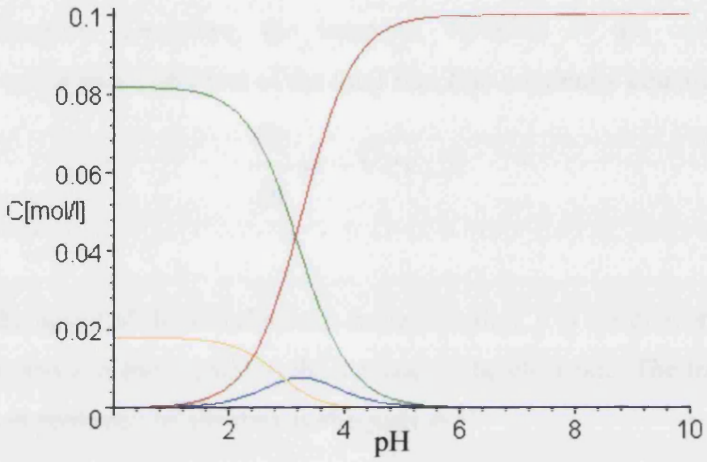

Figure 7.7. The concentrations of HF (green), $(HF)_2$ (yellow), HF_2^- (blue) and F^- (red) in 0.1M NH_4F solution.

The chemical dissolution of silicon in highly acidic NH_4F (pH < 3) solution is dominated by HF species (Figure 7.7) [28], because the concentration of HF in the solution is high, so that hydrogen termination of the surface predominately occurs [28]. Since the hydrogen terminated surface is chemically very stable, the chemical etching rate is expected to be low [28]. The etching of the silicon surface by F^- ions follows an oxidative path [7]. This reaction proceeds competitively with the action of HF and cannot predominate if the concentration of HF is higher than the concentration of F^-, because the HF stabilises the surface by hydrogen termination and thus inhibits the action of F^-. However, as we are studying the photo-induced electrochemical etching of the silicon under oxidative conditions (anodic polarization and hole generation) and

as the pH of the solution is set to be equal to 4.5 (at pH= 4.5, [HF] = 0.0043 M, [F^-]= 0.094 M, [HF_2^-]= 0.0016 M, [$(HF)_2$]= 0.5×10^{-4} M) the action of the F^- ions is favoured [7]. Therefore, the rate of the electrochemical etching is a combination between the speed of the transport of F^- ions from the bulk to the interface and the rate of the electron transfer reaction. As the kinetics of the electrochemical etching is limited by the slowest step in the reaction, we assume that the limiting process for the electrochemical etching is the transport of the F^- ions to the interface. The changes in time of the height u(r,t) are linked to the rate of etching of the surface [28], therefore as the F^- ions reach the surface the local height of the surface changes. As the concentration of fluorine ions is not uniform (because of the etching reaction) the number of ions, which flow from the higher concentration region (the bulk) to the interface (the low concentration region) is larger than the number of ions flowing in the other direction. Therefore, the temporal variation of the concentration is proportional to the space gradient of the total flux (the continuity equation) [29]

$$\frac{\partial c}{\partial t} = -\vec{\nabla} c v_f . \vec{n}$$

Equation 7.5

Where v_f is the speed of the fluorine ions in the solution, c is the concentration of the fluorine ions, and **n** is the normal to the surface of the electrode. The transport of the fluorine ions is governed by the transport equation [29]:

$$\frac{\partial c}{\partial t} = D_f \nabla^2 c$$

Equation 7.6

Where D_f is the fluorine ion diffusion constant. The solution of this equation in the direction normal to the electrode surface has the following form (see Chapter II):

$$c(z,t) = C_\infty erf\left(\frac{z}{2(D_f t)^{\frac{1}{2}}}\right)$$

Equation 7.7

Where erf(x) is the error function and C_∞ is the fluorine ions bulk concentration. This equation is subject to the boundary condition that at the edge of the diffusion layer (of width δ) the concentration of ions must be equal to the bulk concentration. The

velocity of the fluorine ion to reaching the interface is given by the rate of their diffusion across the diffusion layer. This velocity is given by $\frac{D_f}{\delta}$ and is in order of 10^{-2} cm.s^{-1} ($D_f \sim 10^{-5}$ cm.s^{-1} and $\delta \sim 10^{-3}$ cm [11]). The velocity of the ions is, therefore much larger than the dissolution rate (few to hundred of nm.s^{-1} [11]). Considering this fact we can make a simplification: as the velocity of the reactant reaching the surface is bigger than the rate of etching of the surface we can consider that the speed of the fluorine ions crossing the diffusion layer is independent of the position. By considering this simplification, equation 7.5 could be written as:

$$\frac{\partial c}{\partial t} = -v_f \vec{\nabla} c.\vec{n}$$

Equation 7.8

Now we wish to link the variation of the concentration of fluoride at the interface to the speed of dissolution of the interface. The mass conservation law for ions at the interface allows us to relate the normal velocity of the interface to the variation of the concentration of the fluorine ions at the interface.

The variation of the concentration of the fluorine ions at the surface of the electrode at an instant t is due to variation of the volume created by the dissolution of the silicon

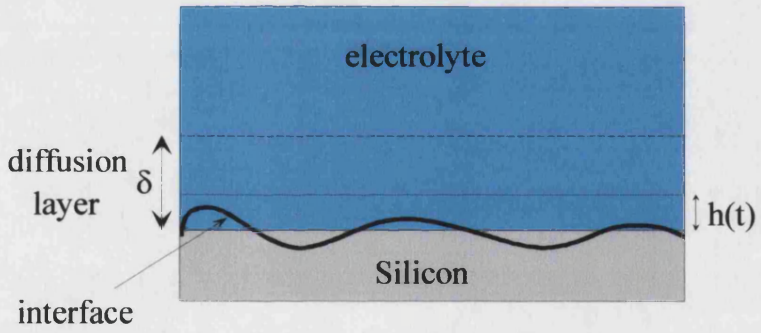

Figure 7.8. Illustration of the configuration between the boundary of the diffusion layer and averaged height of the electrode surface at an instant t.

surface. The accessible reaction volume at the surface of the electrode corresponds to the product between the surface area of the electrode (S) and the width of the diffusion layer. As the position of the interface between the electrode and the electrolyte changes the reaction volume increases, and therefore the variation of the concentration of the fluorine ions at the surface of the silicon electrode is equal to:

$$\frac{\partial c}{\partial t} = -\frac{S}{V}\frac{dh(t)}{dt} \times \left(C_{surface} - C_{reacted}\right)$$

Equation 7.9

Where $C_{surface}$ corresponds to the concentration of the fluorine ions at the surface at an instant t, $C_{reacted}$ is the concentration of the reacted fluorine ions at an instant t and V corresponds to the reaction volume at an instant t. The volume of the reaction at an instant t corresponds to the product of the surface area of the electrode and the sum between the width of the diffusion layer and the dissolved thickness h(t) (figure 7.8).

$$V = S \times (\delta + h(t))$$

Equation 7.10

As we saw before the dissolved thickness at an instant t, h(t), is of order of few to hundred of nanometers. However the width of the diffusion layer is of order of 10^{-3} cm. Therefore we can neglect the dissolved thickness compared to the width of the diffusion layer. This simplification allows us to write equation 7.9 as:

$$\frac{\partial c}{\partial t} = -\frac{1}{\delta}\frac{dh(t)}{dt} \times \left(C_{surface} - C_{reacted}\right)$$

Equation 7.11

As we discussed previously the rate of the reaction was controlled by the diffusion of fluorine ions across the diffusion layer, and we assumed that as the fluorine ions reached the interface, they reacted with the silicon surface. Therefore we can neglect the $C_{surface}$ term in equation 7.11 (because all the fluorine ions are supposed to have reacted). Equation 7.1 shows the general dissolution path for silicon electrode in the region of porous silicon formation [11]. However, in the region of electropolishing the silicon dissolution is expected to be tetravalent [9].

$$Si + 6HF + 4h^{+} \longrightarrow SiF_6^{2-} + 6H^{+}$$

Equation 7.12

Therefore the $C_{reacted}$ in equation 7.9 is equal to

$$C_{reacted} = \frac{1}{\nu} C_{silicon}$$

Equation 7.13

Where ν is the valence of the reaction and $C_{silicon}$ the concentration of silicon atoms. By using equation 7.13 and the assumptions described above we simplify equation 7.9 to

$$\frac{\partial c}{\partial t} = \frac{1}{\delta} \frac{dh(t)}{dt} \times \left(\frac{1}{\nu} C_{silicon} \right)$$

Equation 7.14

Now by considering the conservation of flux (conservation law) of the ions at the interface we can replace the left hand side of equation 7.14 by this value (given by equation 7.8)

$$v_f \nabla c|_{z=0} = \frac{1}{\delta} \frac{dh(t)}{dt} \times \left(\frac{1}{\nu} C_{silicon} \right)$$

Equation 7.15

By remembering that the velocity of the fluorine ions, v_f, is equal to the ratio between the diffusion coefficient of fluorine ions, D_f, and the width of the diffusion layer, δ, we can write the expression for the interface normal velocity as

$$\frac{dh(t)}{dt} = \frac{\nu D_f}{C_{silicon}} \nabla c|_{z=0}$$

Equation 7.16

By differentiating equation 7.7 as a function of space parameter z and calculating its limit for small value of z (at the interface) we find

$$\nabla c|_{z=0} = \lim_{z \to 0} \nabla c = C_\infty \left(\frac{1}{\pi D_f t} \right)^{\frac{1}{2}}$$

Equation 7.17

By replacing equation 7.17 into equation 7.16 we find the normal velocity of the interface as:

$$\frac{dh(t)}{dt} = \frac{v\sqrt{D_f C_\infty}}{\sqrt{\pi} C_{silicon}} t^{-\frac{1}{2}}$$

Equation 7.18

Equation 7.18 expresses the speed of the variation of the position of the interface as a function of time. By using the fact that in the case of a slowly changing surface profile the angular divergence of the reflected beam can be approximated (in the first order) to equation7.3 (Chapter V and Chapter VI) we write the speed of variation of the angular divergence of the reflected beam as

$$\frac{d\alpha(t)}{dt} \approx \frac{2}{d} \frac{v\sqrt{D_f C_\infty}}{\sqrt{\pi} C_{silicon}} t^{-\frac{1}{2}}$$

Equation 7.19

By integrating equation 7.19 over time we can express the variation of the divergence angle as:

$$\alpha(t) \approx 2Bt^{\alpha}$$

Equation 7.20

Where $B = \frac{2}{d} \frac{v\sqrt{D_f C_\infty}}{\sqrt{\pi} C_{silicon}}$ and α=0.5.

Prior to photo-induced electrochemical etching of the silicon electrode, the electrode was maintained at – 0.7 V for 4 hours. During this period the surface of the electrode is roughened (Chapter VI). In the electrochemical etching of the silicon electrode the surface of the electrode undergoes a smoothing transition. Therefore during the etching reaction the divergence of the reflected beam is reduced. This reduction increases the reflected intensity depending on the incident angle (Figure 5.8). Therefore, we use equation 7.20 to calculate the variation of the size of the domain over which the reflected beam is divergent. So we can write equation 7.2 as:

$$I(\theta) = \pm A(\theta_0) * Bt^{\alpha} \cos(2Bt^{\alpha}) + c$$

Equation 7.21

Where

$$A(\theta_0) = \frac{I_0(\theta_0)}{\Delta\theta_{mach}}$$

Equation 7.22

And c is a constant corresponding to the reflected intensity by the interface before the etching process. Equation 7.21 expresses the variation of the reflected intensity as a function of time. As we can see the constant B depends on the diffusion constant D_f and the length d. The parameter d is the distance over which the surface of the sample has the same orientation. The variation of B as a function of time would be significant if the in-plane resolution of the spectrometer permitted us to follow the variation of the distance d as function of time. In our case, the typical in-plane coherence length of the incoming beam is of the order of microns, which means that if the orientation of the surface changes occur on a distance scale smaller than a micron, we will be unable to see any effect of B on the reflected intensity, and B is effectively a constant.

To summarise, in this section we have linked the variation of the reflected intensity to the diffusion of fluorine ions toward the electrode surface and to the valence of the electrochemical etching reaction. We predicted the value of the exponent α to be equal to 0.5. In the next section we apply this formalism to the data described previously and compare the obtained results to the existing literature.

7.6) Application of Theory and Discussion.

Figure 7.9 shows the variation of reflected neutron intensity as function of time

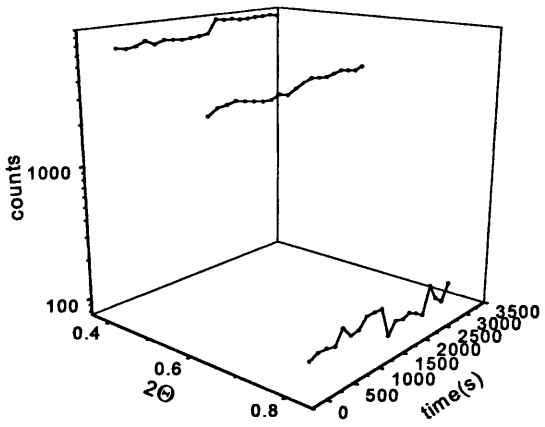

Figure 7.9. Reflected intensity from the sample at three different angles of incidence, as a function of time and the angle of incidence θ.

during the photo induced anodic electroetching reaction at three different angles.

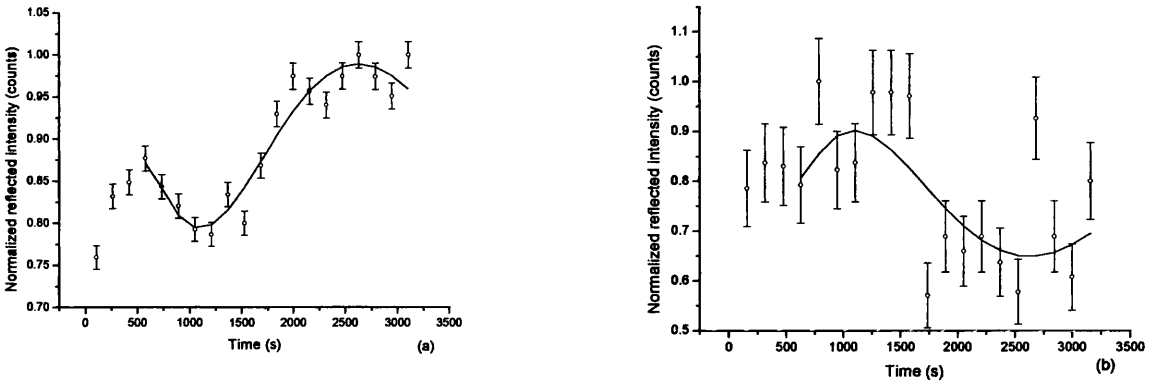

Figure 7.10. (**a**) The normalised reflected intensity from the silicon electrode/deutrated electrolyte at $2\theta=0.6°$. The open circles represent the experimental data and the black line the fit. (**b**) The normalised reflected intensity from the silicon electrode/deutrated electrolyte at $2\theta=0.8°$. The open circles represent the experimental data and the black line the fit.

Figure 7.10 shows the variation of reflected intensity as a function of time during the photo-induced electroetching reaction for two angles above the critical angle. The open circles represent the experimental data and the black line the fit with equation 7.21. Both curves have been fitted simultaneously sharing the parameters α and B. The fitting parameters are shown in Table 7.1.

$2\theta_0$	$A(\theta_0)$	B	t_0	α	C	R^2
0.6	0.0404 ±0.00548	0.09196 ±0.04629	561.6522 ±103.64045	0.46571 ±0.06252	0.86048 ±0.00918	0.86344
0.8	-0.05421 ±0.01831				0.81549 ±0.03846	

Table 7.1. The fitting parameters to the normalised reflected intensity.

However, for the sub-critical (curve at $\theta=0.4$ in Figure 7.9) region we observe only an increase in the value of the reflected intensity. As we noted in Chapter VI, the intensity of the reflected beam in the sub-critical region is not very sensitive to the variation of the momentum transfer. In this region all the intensity of the incoming beam is reflected, so the intensity of the reflected beam, from a perfectly flat surface, remains constant as the momentum transfer Q varies [26]. For a rough surface the reflected intensity is smeared over a range of angles. The smearing of the reflected intensity can be considered by combining the reflected intensity from a perfect surface with a resolution function, as if a whole series of beams were independently scattered

from the sample, thus giving for the observed intensity at a nominal momentum transfer, Q, a value of intensity averaged over many different Q values. As the intensity in the sub-critical region is independent of the wave vector transfer the averaging over this region has the effect of lowering the overall reflected intensity. In the electroetching experiment the surface of the sample changes its morphology from rough to smooth. Therefore the amplitude of the smearing effect in this region decreases and we observe an increase in the reflected intensity when the surface undergoes this smoothing transition.

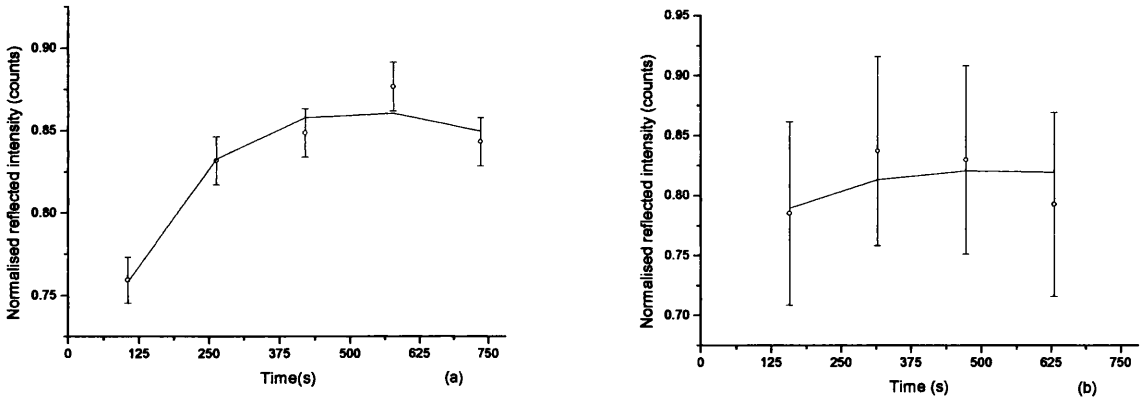

Figure 7.11. **(a)** The normalised reflected intensity from the silicon electrode/deutrated electrolyte interface at $2\theta=0.6°$for potentials smaller than E_1. The open circles represent the experimental data and the black line the fit. **(b)** The normalised reflected intensity from the silicon electrode/deutrated electrolyte interface at $2\theta=0.8°$ for potentials smaller than E_1. The open circles represent the experimental data and the black line the fit.

As we can see, in the parameters presented in table 7.1 a delay time, t_0, is introduced into equation 7.21. As we stressed in the results and discussion section, for potentials above E_1, the electropolishing regime dominates and therefore the state of the structure of the surface changes from rough to wavy and finally to smooth. Below this potential porous silicon is formed [22]. It is well established that during porous silicon formation hydrogen is incorporated into the silicon lattice [30] and the surface of the silicon electrode becomes very rough and hydrogen terminated [9]. Therefore, the variation of reflected intensity below the potential E_1, must be linked to the diffusion of hydrogen into silicon lattice and its behaviour should follow the model described in Chapter VI. Figure 7.11 shows the reflected intensity below the potential E_1 during the photo-induced electrochemical etching for the two angles 0.6° and 0.8°. The open circles are the data and the black line the fit to equation 6.12. Both curves have been fitted simultaneously. The fitting parameters are presented in table 7.2.

$2\theta_0$	$A(\theta_0)$	B	$1/\beta$	C	R^2
0.6	1.2786 ±0.03371	0.03203 ±0.01126	0.41512 ±0.06034	0.50268 ±0.04320	0.94818
0.8	0.58262 ±1.76076			0.749 ±1.7676	

Table 7.2. The fitting parameters to the normalised reflected intensity.

The large spread over the values of the different fitting parameters is due to the large errors in the experimental data in the case of the incident angle equal to 0.8°. As we can see the value of the exponent $1/\beta$ is smaller than 0.5, which is characteristic of the diffusion of hydrogen into the silicon lattice as we demonstrated in Chapter VI.

The parameter B (Table 7.1) and the exponent α have been related to the diffusion of fluorine ions. The value of the exponent α (0.46571 ±0.06252) is close to the predicted value of 0.5.By using the value of the parameter B (0.09196 ±0.04629) and its analytical expression we can find the valence of the overall reaction. The in-plane correlation length of the incident neutron beam is about one micrometer (d = 0.9 μm) and the diffusion coefficient of the fluorine ions is approximatively 10^{-5} $cm.s^{-1}$ [11], the bulk concentration of the fluorine ions is equal to 0.094 M (Figure 7.7) and the concentration of the silicon atoms is equal to 0.0832 $mol.cm^{-3}$. Therefore the valence ν of the overall reaction is equal to $\nu = 2.2 \pm 1.1$. ν is the number of consumed fluorine ions per silicon atom. Therefore the obtained value for the valence of the reaction suggests that on average two fluorine ions are needed to dissolve one silicon atom. This result is in good agreement with the dissolution process described by *Allongue et al* [7]. Under illumination, in the case of n-type semiconductor, holes migrate toward the surface of the electrode and either react with redox species in solution or generate the decomposition of the semiconductor. Therefore, the first step in the reaction corresponds to the hole generation in the semiconductor by illumination (Figure 7.12). The silicon atom at the surface of the electrode captures the hole. The latter liberates a proton. This proton can be temporarily associated with a fluorine ion. Then the radical Si reacts with a fluorine ion via a two steps process including the formation of bond Si-OH. The OH species are substituted quickly with F. After this stage the reaction continues chemically. In this overall reaction the rate-

determining parameter is the concentration of fluorine ions [7]. As we can see two fluorine ions are necessary to remove one silicon atom (Figure 7.12).

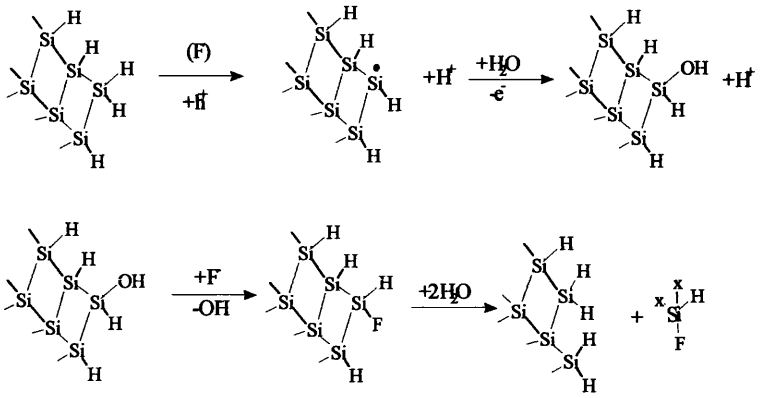

Figure 7.12 Structural 2-D model showing the dissolution of n-Si [111] in NH_4F solution of pH= 4.5. Reactants and reaction products are preceded by + and – respectively. Species in parenthesis are contributing indirectly to reaction steps [7]

7.7) Conclusion

In this chapter we have demonstrated the possibility of studying the kinetics of surface changes of n-type silicon electrode during anodic photo-induced etching. We have demonstrated that the first part of the reflected intensity ($E < E_1$) can be fitted by the developed model in Chapter VI, where the kinetics of the surface changes are related to the adsorption of hydrogen into the silicon lattice. The use of this model, in this region of potential, is supported by existing literature [30], where hydrogen adsorption is considered to be the key process during porous silicon formation [30]. In the second region of the reflected intensity ($E > E_1$) the surface undergoes a smoothing transition. We demonstrated that in this region the kinetics of the changes in the surface morphology follow the speed of diffusion of fluorine ions in the solution. We used again the existing literature to support the value of the valance found for the overall reaction [7].

At this stage of our investigation of the surface conditioning of n-type silicon electrode we should compare the value of the exponents $1/\beta$ and α. We showed that the value of the exponent $1/\beta$ (in the case of photo-induced anodic etching $1/\beta = 0.41512 \pm 0.06034$) corresponds to the anomalous diffusion of hydrogen into the silicon lattice. This anomalous diffusion is due to the existence of a distribution of jump length and time of flight [31] between two adjacent sites for hydrogen atoms. Therefore the movement of hydrogen is not uniform in the silicon lattice and follows

the distribution of the rest time and jump length. Therefore for potentials smaller than E_1, where the kinetics of the surface variation is due to hydrogen adsorption [30] one expects to find nonuniform and anisotropic changes in the roughness of the surface. This fact is confirmed by several authors [8, 9, 30]. They found that the roughening of the surface is anisotropic during the porous silicon formation. The value of the exponent α (α = 0.46571 ±0.06252) corresponds to the case of a normal diffusion regime [31], where the fluorine ions diffuse uniformly in the electrolyte toward the surface of the electrode. Therefore, their action over the structure of surface should be isotropic. This observation is supported by the fact that during the electropolishing regime the changes on the surface structure are isotropic [8].

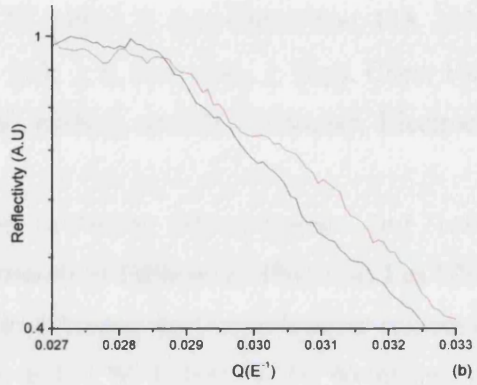

Figure 7.13 The superposition of the reflectivity profile after 129 s of etching (black line) and 2976 s of etching (red line) both curves have been smoothed by use of an adjacent averaging algorithm over 30 points. As we can see the shape of the critical edge is slightly rounded.

Figure 7.13 represents the time-resolved *in-situ* X-ray reflectivity profile data in the region of total reflection during the chemical etching of n-type silicon [111] in 1% HF: 50% NH_4F (in volume). *Itaya et al* [17] showed that the chemical etching of silicon in this solution leads to an atomically smooth and H terminated surface. However, after 24 min of etching in this solution we can notice as light rounding of the shape of the total reflection edge (figure 7.13). Therefore, the surface of the silicon substrate should present macroscopic features (wavy surface). However, the rounding of the shape of the total reflection edge is not as dramatic as that happening during electrochemical etching. Therefore, this result confirms the fact that electrochemical etching roughens the surface of the electrode on an atomic scale and

smoothes it on a macroscopic scale, whereas chemical etching roughens the surface of the electrode on a macroscopic scale but smoothes it on a microscopic scale [7].

References:

1 M. Aggour, M. Giersig, and H. J. Lewerenz, Journal of Electroanalytical Chemistry **383**, 67 (1995).

2 H. J. Lewerenz, J. Phys. Chem. B **101**, 2421 (1997).

3 M. Matsumura and R. Morrison, J. Electroanal. Chem. **144**, 113 (1983).

4 L. M. Peter, D. J. Blackwood, and S. Pons, Physical Review Letters **62**, 308 (1989).

5 Y. Kim and C. M. Lieber, J. Am. Chem. Soc. **113**, 2333 (1991).

6 J. H. Ye, T. H. Bok, J. S. Pan, et al., J. Phys. Chem **103**, 5820 (1999).

7 P. Allongue, V. Kieling, and H. Gerischer, Electrochemica Acta **40**, 1353 (1995).

8 J.-N. Chazalviel, in *Porous Silicon Science And Technology*, edited by J.-C. Vial and J. Derrien (Les Editions de Physique, Les Ulis, 1995), p. 17.

9 P. C. Searson, in *Advances in electrochemical science and engineering*, edited by H. Gerischer and C. W. Tobias (VCH, Weinheim, 1995), Vol. 4.

10 M. Rauscher and H. Spohn, Physical REVIEW E **64**, 1 (2001).

11 A. Valance, Physical Review B **52**, 8323 (1995).

12 P. Allongue, C. H. d. Villeneuve, S. Morin, et al., Electrochemica Acta **45**, 4591 (2000).

13 J. Rappich and H. J. Lewerenz, Thin Solid Films **276**, 25 (1996).

14 K.-i. Hara and I. Ohdomari, Jpn. J. Appl. Phys **37**, L 1333 (1998).

15 J. Rappich, M. Aggour, S. Rauscher, et al., Surface Science **335**, 160 (1995).

16 G. S. Higashi, R.S.Becker, Y. J. Chabal, et al., Applied physic letter **58**, 1656 (1991).

17 K. Itaya, R. Sugawara, Y. Morita, et al., Applied Physics letter **60**, 2534 (1992).

18 M. Bailes, S. Bohm, L. M. Peter, et al., Electrochemica Acta **43**, 1757 (1998).

19 H. Fukidom and M. Matsumura, Applied surface Science **130 - 132**, 146 (1998).

20 R. Houbertz, U. Mermmert, and R. J. Behm, Surface Science **396**, 198 (1998).

21 K.-i. Hara and I. Ohdomari, Applied surface Science **144-145**, 476 (1999).

22 A. Halimaoui, in *Porous silicon science and technology*, edited by J. C. Vial and J. Derrien (Springer - Verlag, New York, 1994), Vol. 1, p. 33 .

23 M. Matsumura and R. Morrison, J. Electroanal. Chem. **147**, 157 (1983).

24 L. Bailey, M. J. Henderson, A. R. Hillman, et al., Physica B **276-278**, 373 (2000).

25 J. S. Higgins and H. C. Benoit, *Polymers and Neutron Scattering*, New York, 1996).

26 J. Daillant and A. Gibaud, *X-Ray and Neutron Reflectivity: Principles and Applications*, 1999).

27 L. Landau and E. Lifchitz, *Physique statistique* (Edition Mir, 1994).

28 H. Fukidome, in *Department of Chemistry* (Osaka University, Osaka, 2000).

29 M. Doi and S. F. Edwards, *The theory of polymer dynamics*, 1986).

30 P. Allongue, C. H. d. Villeneuve, L. Pinsard, et al., Appl. Phys. Lett **67**, 941 (1995).

31 R. METZLER and J. KLAFTER, Physics reports **339**, 1 (2000).

Chapter VIII

Conclusion and Further work

"I used to be uncertain, but now I'm not so sure."
T-shirt slogan

8.1) Conclusion

In these chapters, we have demonstrated the possibility of using silicon as a working electrode for *in-situ* reflectivity studies of an electrochemical system. The low scattering length density of silicon compared to other metallic electrode and its relative transparency to neutrons make this material as an ideal electrode for *in-situ* neutron and x-ray reflectivity studies on electrochemical system. The structure of this electrode is simple and it is relatively straightforward to chemically clean the surface of this electrode. However, the major problem with this is the natural oxidation of its surface. This problem can be overcome by using n-type silicon [111] where an chemical etching of the surface of the electrode by 40%NH_4F leaves the surface stable and oxide free and therefore electrochemically active. In order to demonstrate the feasibility of an *in-situ* reflectivity experiment with this electrode, we studied the electrodeposition of poly (aniline) film.

Poly (aniline) is a conducting polymer, formed by anodic oxidation of aniline in acidic solution under illumination. The polymer film was formed by cyclic voltammetry and by potential step method. During the X-ray *in-situ* reflectivity experiment the high energy X-ray source allowed us to study the structure of the polymer film under the solution and the energy dispersive detector of the spectrometer gave time resolved characterisation of the polymer film. By this study we demonstrated that the polymer film is composed of two parts: the first part, in the vicinity of the electrode surface, is formed of a dense layer of poly (aniline). The time resolved *in-situ* reflectivity and the electrochemical measurements suggest that the formation of the compact layer is completed after the second applied cycle. Then the second part is formed by a more open polymer structure on top of the first dense layer. The comparison between the reflectivity profile from the film in at water interface and at the air interface shows clearly the penetration of solvent into the polymer film. This observation with x-rays was possible because of the low scattering length density of the silicon electrode and the high degree of penetration of the used X-ray radiation. However, It was difficult to extract any quantitative information from the reflectivity profiles because of the high degree of roughness of the deposited polymer film. In order to study the specular reflectivity from very rough surfaces we developed a new theory based on the optical geometry.

We propose a simple technique to analyze X-ray and neutron reflection data from a macroscopically rough surface. It was shown that in the limit that the correlation length and the height of the surface roughness are larger than the wavelength (at least 100 times bigger) of the incoming beam, the total reflection edge in the reflection profile becomes rounded. The particular case where the height variation of the surface texture is smooth and small compared to the surface correlation length was developed. However, it must be kept in mind that this technique can only be applied to surfaces that have a correlation length and a local height bigger than the wavelength of the incoming beam. Using neutrons or X-rays to study the structure of an interface the wavelength of the incoming beam is typically in the range of 1 Å to 12 Å, it is possible to use the formalism described in the chapter V to analysis if the correlation length of the surface structure is in the range of 100 to 800Å or even bigger. One of the must interesting characteristics of this technique is the possibility to apply it near the region of the total reflection. In this region the flux of the reflected beam is high, and it allows one to measure directly the kinetics of the surface roughening transition as chosen parameters of the system varies. The scale invariance of the developed theory in the case of surfaces where the correlation length is bigger than the in-plane coherence length of the incoming beam demonstrates the possibility to link the changes in the shape of the total reflection edge (a macroscopic effect) to the microscopic changes on the surface profile. This technique has been applied to the neutron reflection study of hydrogen evolution reaction under cathodic bias at silicon / fluoride containing solution interface and to the photo induced electrochemical and chemical etching of n-type silicon [111] in fluorine containing solution. For each of them we were able to determine the kinetics and the origins of the roughening transition.

In chapter VI we have shown that it is possible to correlate the changes of the specularly reflected intensity from silicon/electrolyte solution during the hydrogen adsorption reaction to the diffusion of hydrogen into the silicon electrode. We used the formalism developed in the chapter V and the following picture: at the beginning of the process only a few H_2 bubbles are desorbed from the electrode and therefore the surface lateral correlation length is big. However as the desorption process is carried out this correlation length becomes smaller. This picture suggests that the rate determining step for the roughening process of the silicon surface during the hydrogen evolution reaction is the desorption of hydrogen from the silicon electrode, which is

why we have linked the changes of reflectivity intensity to the kinetics of the hydrogen diffusion into the silicon lattice. We have shown that the changes of the silicon surface roughness under cathodic polarization is due to the adsorption and desorption of the hydrogen, and the kinetics of these changes are dominated by the diffusion of the hydrogen atoms in the silicon lattice following a sub diffusive regime. The same approach is used in the chapter VII to study the kinetics of the photoinduced electrochemical and chemical etching of n-type silicon [111] electrode in fluorinated solution. We demonstrated that electrochemical etching of n-type silicon under front illumination in fluorine containing solution depends on the applied potential. The variation of the reflected intensity at fixed angle as a function of potential demonstrates four distinct regions: the first region corresponds to cathodic bias (just after the porous silicon formation peak) where the morphology of the surface is determined by the hydrogen diffusion. The second region corresponds to the direct dissolution of the silicon electrode and the formation of a "wet oxide" layer. The third region corresponds to the formation of a "wet oxide" oxide layer and finally the fourth region corresponds to the formation of a "dry oxide" layer. We demonstrated that the kinetics of the variation of the reflected intensity follows the diffusion of fluorine ions in the solution when the electrode is under the anodic bias. The comparison between the shape of the critical edge between the chemical etching and the electrochemical etching shows that the chemical etching produce an atomically smooth surface but a macroscopically rough surface, whereas the chemical etching produce an microscopically rough surface and macroscopically rough surface.

8.2) Further work

An obvious extension of this work is the use of the silicon electrode to study the structure of the electrodeposited material by neutron reflectivity. As silicon is transparent to neutrons, the solid / liquid interface can be easily illuminated through the silicon electrode. The advantage of neutrons over the X-rays is the possibility to change the contrast of the solution, and therefore to have a better resolution of the structure of the deposited material. In our work we demonstrated the possibilities to use X-rays to determine the structure of an electrodeposited polymer film on the top of the silicon electrode and even we were able to observe the solvent penetration into the polymer film. This observation suggests that the use of silicon as an electrode offers the possibility of studying the structure of an electrodeposited material by X-

ray and neutron reflectivity without changing the conditions and the experimental arrangements. Therefore, the structure of the film can be highly resolved by the combination of the neutron reflectivity data and the X-ray reflectivity data.

Another possible extension of this work would be the application of the developed theory to other systems. Table 8.1 shows the domains of application covered by different theory of scattering from rough surfaces.

	$\sigma << \xi$	$\sigma < \xi$	$\sigma \sim \xi$	$\sigma > \xi$	$\sigma >> \xi$
$\xi << l_{coh}$	First order DBWA	First order DBWA	First order DBWA	First order DBWA	?
$\xi < l_{coh}$	Second order DBWA	Second Order DBWA	Second Order DBWA	Second Order DBWA	?
$\xi \sim l_{coh}$	Developed theory	Developed theory	Developed theory	Developed theory	?
$\xi > l_{coh}$	Developed theory	Developed theory	Developed theory	Developed theory	?
$\xi >> l_{coh}$	Kirchof	Kirchof	Kirchof	Kirchof	Kirchof

Table 8.1. Domain of application of different existing theory of scattering from rough surfaces.

As we can see the developed theory can describe system with an in-plane correlation length, ξ, roughly equal or much bigger than the in-plan coherence length of the incoming beam, l_{coh}. Figure 8.1 represents the variation of the angular divergence of the reflected beam as a function of the ratio of the coherence length of the incoming beam and the correlation length ($x = l_{coh} / \xi$) for a given correlation length (ξ) and a given surface dimension h.

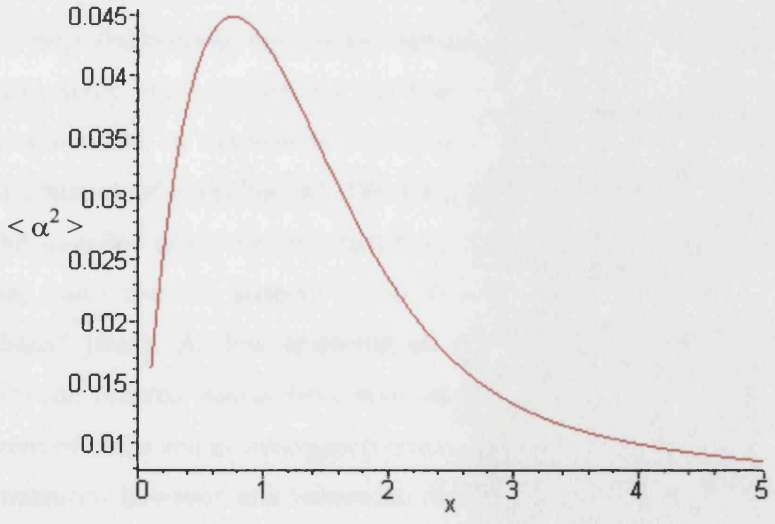

Figure 8.1 Variation of the angular divergence of the reflected beam as a function of the ratio between the coherence length and the correlation length for a surface where the correlation length is fixed to be equal to 100 Å the rms height value to 10 Å and the dimensionality of the surface (h) to 0.7

As we can see in the limit of large coherence length ($x >> 1$) the value of the angular divergence of the reflected beam reaches a plateau. However, in the intermediate region ($x \sim 1$), where the value of the in-plane coherence length matches roughly the value of the in-plane correlation length, the value of the angular divergence of the reflected beam passes through a maximum. By following the discussions and arguments presented in Chapter V, an increase in the value of the angular divergence increases the deformation of the shape of the total reflection edge.

All these consideration suggests the possibility of using the specular reflectivity to measure the in-plane correlation length of a sample having a macroscopic roughness. The advantage of this technique over the standard technique (AFM and STM) is that it can be applied easily to the buried interfaces and the experimental set-up does not need any modifications of a standard reflectometer. The proposed experiment consists of illuminating the surface of the sample in the region of total reflection edge and measuring the rounding of the latter by varying the dimension of the in-plane coherence length. The perfect candidates to be studied by this technique would be systems with low frequency surface profile variation, in other words samples whose surface presents some ripples: as the surface of the layers formed by using ion sputtering [1,2].

One of the most interesting aspects of the developed theory is its domain of application which corresponds to interfaces which have a large correlation length. The presence of a large correlation length corresponds to a long-range interaction between the constituents of the system. It is well known that the range of the interaction becomes very large (infinity) during a phase transition. Therefore the presented theory can be used to study and to determine the kinetics of phase transition of a two-dimensional system. As an example one can use the developed theory to study the behaviour of a bilayer of phospholipid. The main transition of phopshocholine (PC) bilayers is the so-called chain melting transition, which is primarily a breakdown of chain ordering, such that the material moves from ordered solid - like phase to a disordered liquid phase. At low temperatures (i.e. far below the chain melting transition), several ordered phases have been identified which are characterised by varying degrees of chain and or head group order. In between the ordered phases and the melting transition however, and interesting rippled phase exists where the surface of the bilayer becomes strongly undulating in character.

References:

1 S. Rusponi, G. Costantini, C. Borgano, *et al.*, Physical Review Letters **81**, 4184 (1998).

2 R. M. Bradley and J. M. E. Harper, J. Vac. Sci. Technol. A **6**, 2390 (1988).